

ΤΜΗΜΑ ΙΑΤΡΙΚΗΣ ΣΧΟΛΗ ΕΠΙΣΤΗΜΩΝ ΥΓΕΙΑΣ ΠΑΝΕΠΙΣΤΗΜΙΟ ΙΩΑΝΝΙΝΩΝ

ΧΕΙΡΟΥΡΓΙΚΟΣ ΤΟΜΕΑΣ ΚΛΙΝΙΚΗ ΜΑΙΕΥΤΙΚΗΣ ΚΑΙ ΓΥΝΑΙΚΟΛΟΓΙΑΣ

ΠΡΟΣΟΜΟΙΩΣΕΙΣ ΥΠΟΛΟΓΙΣΤΙΚΗΣ ΡΕΥΣΤΟΔΥΝΑΜΙΚΗΣ (CFD) ΣΤΗ ΜΑΘΗΜΑΤΙΚΗ ΜΟΝΤΕΛΟΠΟΙΗΣΗ ΤΗΣ ΑΙΜΑΤΙΚΗΣ ΡΟΗΣ ΜΗΤΡΙΑΙΩΝ ΚΑΙ ΟΜΦΑΛΙΚΩΝ ΑΡΤΗΡΙΩΝ ΜΕΣΩ ΑΠΛΟΥΣΤΕΥΜΕΝΩΝ ΚΑΙ ΑΝΩΤΕΡΗΣ ΤΑΞΗΣ ΜΑΘΗΜΑΤΙΚΩΝ ΜΟΝΤΕΛΩΝ

ΑΝΑΣΤΑΣΙΟΣ Χ. ΦΕΛΙΑΣ

ΜΑΘΗΜΑΤΙΚΟΣ

ΔΙΔΑΚΤΟΡΙΚΗ ΔΙΑΤΡΙΒΗ



FACULTY OF MEDICINE SCHOOL OF HEALTH SCIENCES UNIVERSITY OF IOANNINA

SURGERY SECTOR
DEPARTMENT OF OBSTETRICS AND GYNECOLOGY

COMPUTATIONAL FLUID DYNAMICS (CFD) SIMULATIONS IN THE MATHEMATICAL MODELING OF BLOOD FLOW IN THE UTERINE AND UMBILICAL ARTERIES USING SIMPLIFIED AND HIGHER-ORDER MATHEMATICAL MODELS

ANASTASIOS C. FELIAS

MATHEMATICIAN

DOCTOR OF PHILOSOPHY THESIS



Ημερομηνία αίτησης του κ. Φελιά Αναστάσιου: 10-06-2022

Ημερομηνία ορισμού Τριμελούς Συμβουλευτικής Επιτροπής: Γ.Σ. αριθμ. 1019α/12-07-2022

Μέλη Τριμελούς Συμβουλευτικής Επιτροπής:

Επιβλέπων:

Πασχόπουλος Μηνάς, Καθηγητής Μαιευτικής-Γυναικολογίας του Τμήματος Ιατρικής του Πανεπιστημίου Ιωαννίνων

Μέλη:

Ξένος Μιχαήλ, Αναπληρωτής Καθηγητής Εφαρμοσμένων και Υπολογιστικών Μαθηματικών του Τμήματος Ιατρικής του Πανεπιστημίου Ιωαννίνων

Τζίμας Πέτρος, Αναπληρωτής Καθηγητή Αναισθησιολογίας του Τμήματος Ιατρικής του Πανεπιστημίου Ιωαννίνων

Ημερομηνία ορισμού θέματος: Γ.Σ. αριθμ. 1019α/12-07-2022

«Μαθηματική μοντελοποίηση της ροής φαρμάκου στο εγκεφαλονωτιαίο υγρό του νωτιαίου μυελού, μέσω τεχνικών τρισδιάστατης αλληλεπίδρασης ρευστού-δομής (3D FSI), κατά τη χορήγηση επισκληρίδιου αναισθησίας στον τοκετό»

Τροποποίηση τίτλου θέματος: Γ.Σ. αριθμ. 1080α/14-12-2023

«Προσομοιώσεις υπολογιστικής Ρευστοδυναμικής (CFD) στη μαθηματική μοντελοποίηση της αιματικής ροής μητριαίων και ομφαλικών αρτηριών, μέσω απλουστευμένων και ανώτερης τάξης μαθηματικών μοντέλων»

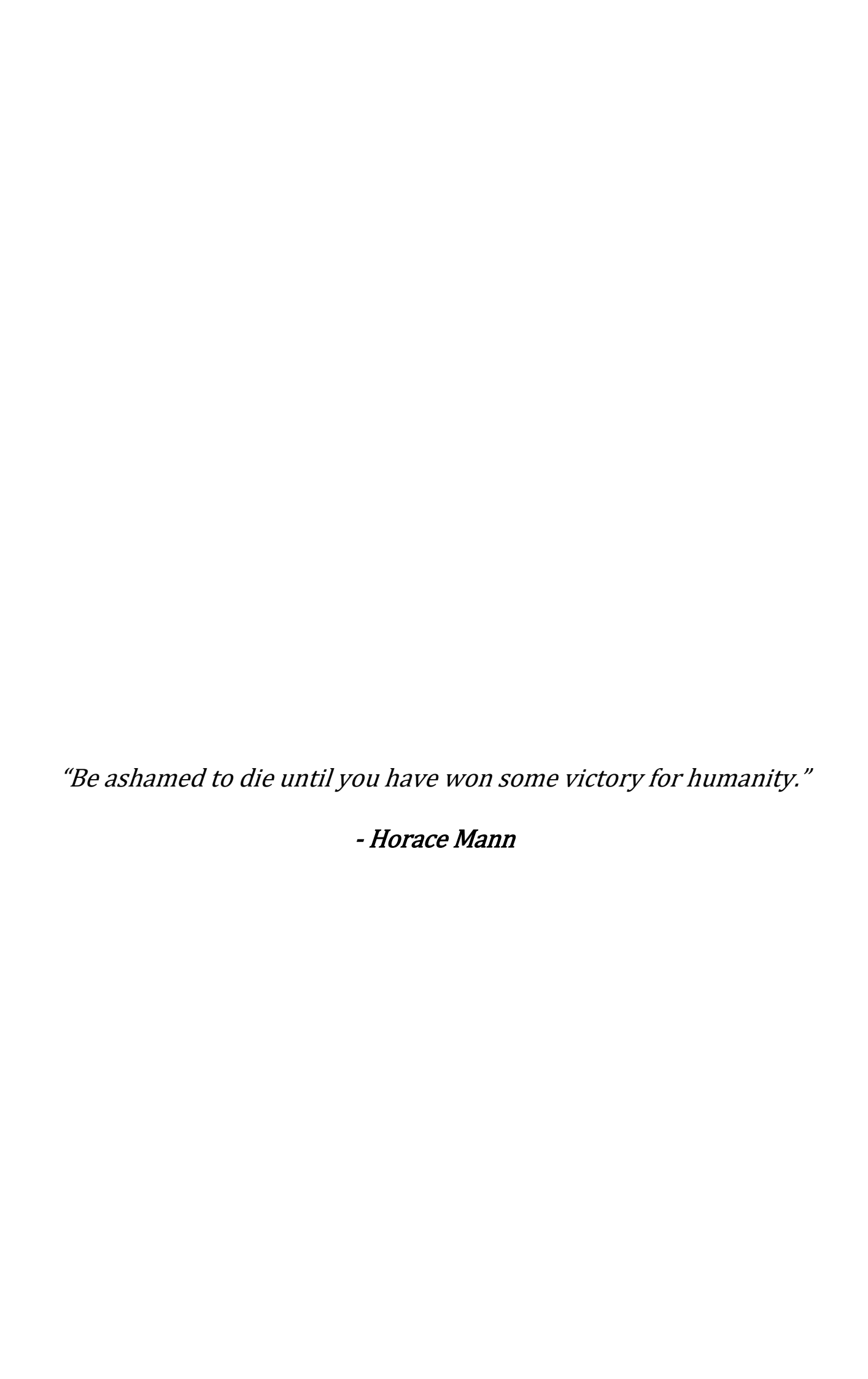
ΟΡΙΣΜΟΣ ΕΠΤΑΜΕΛΟΥΣ ΕΞΕΤΑΣΤΙΚΗΣ ΕΠΙΤΡΟΠΗΣ: 1161α/09-09-2025

- 1. Πασχόπουλος Μηνάς, Καθηγητής Μαιευτικής-Γυναικολογίας του Τμήματος Ιατρικής του Πανεπιστημίου Ιωαννίνων
- 2. Ξένος Μιχαήλ, Καθηγητής Εφαρμοσμένων και Υπολογιστικών Μαθηματικών του Τμήματος Μαθηματικών του Πανεπιστημίου Ιωαννίνων
- 3. Τζίμας Πέτρος, Καθηγητής Αναισθησιολογίας του Τμήματος Ιατρικής του Πανεπιστημίου Ιωαννίνων
- 4. Σκέντου Χαρίκλεια, Επίκουρη Καθηγήτρια Μαιευτικής-Γυναικολογίας με έμφαση στην Εμβρυομητρική Ιατρική του Τμήματος Ιατρικής του Πανεπιστημίου Ιωαννίνων
- 5. Γκρόζου Φανή, Επίκουρη Καθηγήτρια Μαιευτικής-Γυναικολογίας με έμφαση στη Γυναικολογική Ενδοσκόπηση του Τμήματος Ιατρικής του Πανεπιστημίου Ιωαννίνων
- 6. Βατοπούλου-Βουγιούκα Αναστασία, Επίκουρη Καθηγήτρια Μαιευτικής-Γυναικολογίας με έμφαση στην Παιδική και Εφηβική Γυναικολογία του Τμήματος Ιατρικής του Πανεπιστημίου Ιωαννίνων
- 7. Ρασσιάς Μιχαήλ, Καθηγητής Μαθηματικής Ανάλυσης, Θεωρίας Αριθμών και Κρυπτογραφίας του Τομέα Μαθηματικών και Επιστημών Μηχανικού της Στρατιωτικής Σχολής Ευελπίδων

Έγκριση Διδακτορικής Διατριβής με βαθμό «ΑΡΙΣΤΑ» στις 30-09-2025

Ιωάννινα 24-11-2025 ΠΡΟΕΔΡΟΣ ΤΟΥ ΤΜΗΜΑΤΟΣ ΙΑΤΡΙΚΗΣ Σπυρίδων Κονιτσιώτης Καθηγητής Νευρολογίας Η Αναπλήρωτρια Γραμματέας του Τμήματος Ιωάννα Ντούβλη

	Dedicated to	my family an	d to Irene
Αφιερώνεται σ	στην οικογένε	ιά μου και στ	ην Ειρήνη



Preface

Blood flow dynamics within the uterus and umbilical cord play a crucial role in maternal-fetal health, influencing fetal development and well-being throughout gestation. The intricate interplay of physiological factors and geometrical complexities presents challenges for the accurate modeling and prediction of these flows. This thesis addresses these challenges through the application of Computational Fluid Dynamics (CFD) simulations and advanced mathematical modeling techniques, informed by a comprehensive statistical analysis of Doppler ultrasound data from a large cohort of pregnant women.

The use of CFD traces back to the mid-20th century, with the advent of digital computers and the pioneering work of researchers such as John von Neumann and Stanislaw Ulam. Initially focused on aerodynamics and heat transfer, CFD has since evolved into a multidisciplinary approach applied to biomedical engineering and fluid-structure interaction. In this work, CFD serves as a powerful tool to enhance visualization and quantitative assessment of uterine and umbilical blood flow characteristics beyond those accessible through Doppler ultrasound alone.

Motivated by the need to deepen understanding of uterine and umbilical arterial hemodynamics, especially in the context of pregnancy complications such as pre-eclampsia and intrauterine growth restriction, this study examines three-dimensional transient flow scenarios using inlet velocity profiles derived from Doppler ultrasound data of more than 200 pregnant women during their second and third trimesters. Statistical analyses reveal significant increases in umbilical arterial peak systolic velocity (PSV) between the 22nd and 30th gestational weeks, contrasted with relatively stable uterine artery velocity profiles, indicating vascular adaptations.

The Navier–Stokes (NS) equations form the foundation of the mathematical modeling, which incorporates non-Newtonian blood properties to accurately capture pulsatile flow dynamics and shear stress distributions. Key hemodynamic parameters, including time-averaged wall shear stress (TAWSS), oscillatory shear index (OSI), relative residence time (RRT), Reynolds number (Re), and Dean number (De)—are quantified to assess laminar flow stability in the uterine artery and secondary flow phenomena in the umbilical artery. The identification of secondary flow patterns within the umbilical artery provides novel insights into the complex interactions between primary and secondary flows, a phenomenon that is difficult to discern via ultrasound imaging alone.

The uterine and umbilical arteries are conceptualized as simplified geometries, such as straight and coiled cylindrical pipes, enabling detailed numerical simulations using advanced CFD software. The simulation results are compared against mathematical and theoretical models to validate the approach and provide population-specific hemodynamic reference values.

Through these combined methodologies, this thesis contributes to a refined understanding of maternal-fetal blood flow dynamics, with important implications for clinical assessments and the monitoring of pregnancy progression. It is my hope that these findings will advance knowledge in maternal-fetal medicine and biofluid mechanics, ultimately improving early diagnosis and management strategies for pregnancy-related complications.

I express my sincere gratitude to my supervisor, Minas Paschopoulos, Professor in the Department of Obstetrics and Gynecology at the Medical School of the University of Ioannina, whose guidance and expertise have been invaluable throughout this journey. His unwavering support and insightful feedback have significantly shaped the direction of this research.

I also express my appreciation to my committee members for their constructive criticism and scholarly input. Their diverse perspectives have enriched the depth and breadth of this work. More specifically, I would like to thank:

- Michail Xenos, Professor of Applied and Computational Mathematics at the Department of Mathematics of the University of Ioannina
- Petros Tzimas, Professor in the Department of Anaesthesiology and Postoperative Intensive Care of the Medical School of the University of Ioannina
- Charikleia Skentou, Assistant Professor in the Department of Obstetrics and Gynecology at the Medical School of the University of Ioannina
- Fani Gkrozou, Assistant Professor in the Department of Obstetrics and Gynecology at the Medical School of the University of Ioannina
- Anastasia Vatopoulou-Vougiouka, Assistant Professor in the Department of Obstetrics and Gynecology at the Medical School of the University of Ioannina
- Michail Rassias, Professor of Mathematical Analysis, Number Theory and Cryptography at the Department of Mathematics and Engineering Sciences of the Hellenic Military Academy (HMA)

Furthermore, I am indebted to my colleagues and collaborators for their camaraderie and intellectual exchange, which have fostered a stimulating research environment. A special thanks goes to my friend and fellow mathematician, Dimitrios Delidis, for sharing his expertise in the statistical analysis of this thesis. Last but not least, I would like to thank my dear friends, Ph.D. candidates in Classical Studies, Vasiliki Tziora and Evangelos Tsoumpos, for their valuable contribution to the syntactic and expressive aspects of the text. Finally, I dedicate this thesis to my family and to my girlfriend Irene, whose love and encouragement have been my source of motivation.

This research was partially carried out within the framework of the Action "Flagship actions in interdisciplinary scientific fields with a special focus on the productive fabric", which is implemented through the National Recovery and Resilience Plan Greece 2.0, funded by the European Union—NextGenerationEU (Project ID: TAEDR-0535983). Additionally, I would like to acknowledge that my work was also supported through the program "DIONI: Computational Infrastructure for Processing and Analysis of Big Data – Subproject 1: Research Activity and Cloud Services" (Code 82870), under the scientific direction of Mr. Stavros Nikolopoulos. My contributions focused on the development, management, and maintenance of scientific computing software in the field of Biomedical Applications, within Work Package P1.1 of the "DIONI" project.

Informed consent was obtained from all subjects involved in the study. The study was also approved by the Scientific Research Committee of the University of Ioannina and the Commanding Board of the University Hospital of Ioannina (approval number: 4558/24-2-25). The approval can be found in Approval PDF.

The sample consisted of 200 Greek pregnant women, examined during the second and third trimesters of pregnancy using Doppler ultrasound. Data are unavailable due to privacy and ethical restrictions.

Anastasios Felias 30/09/2025

Contents

1	Intr	roduction	25
	1.1	Literature review	25
	1.2	Scope of the study	27
2	Mai	in Body	29
	2.1	Materials and Methods	29
		2.1.1 Doppler ultrasonography	29
		2.1.2 Statistical analysis of ultrasound data	32
		2.1.3 Mathematical modeling and computational approach	36
		2.1.4 Exact flow models	48
		2.1.5 Simulations properties	58
	2.2	Results	62
		2.2.1 Uterine arterial flow	62
		2.2.2 Umbilical arterial flow	65
	2.3	Discussion	70
	2.4	Conclusions	72
		2.4.1 Future directions	73
Sī	innle	emental Material	75
~ .			
3	\mathbf{Abs}	tracts	77
	3.1	Abstract in English	77
	3.2	Abstract in Greek	78
		3.2.1 Review of the thesis (in Greek)	78
4	Not	able Work	83
		Published work	84
	4.2	Work in progress	88
	4.3	Conference activity	90
		Peer reviewing	92

List of Figures

1.1	[A] Uterine and [B] umbilical arterial geometries.	25
1.2	Cross-sectional anatomy of the umbilical cord, displaying the ar-	
	rangement of the umbilical vein, umbilical arteries, Wharton's	
	Jelly, and surrounding structures. The umbilical vein (blue) car-	
	ries oxygenated blood from the placenta to the fetus, while the	
	umbilical arteries (red) transport deoxygenated blood back to	
	the placenta. Wharton's Jelly, a gelatinous substance, provides	
	structural support and protects these vessels	26
1.3	Schematic overview of the study methodology	27
2.1	Schematic explanation of the Doppler ultrasound mechanism	30
2.2	Waveform representation of blood flow velocity across a cardiac cy-	
	cle, illustrating key Doppler ultrasound parameters: Peak Systolic	
	Velocity (PSV), Mid-Diastolic Velocity (MDV) and End-Diastolic	
	Velocity (EDV). The shaded area under the curve reflects the	
	total flow during one cycle, corresponding to the product of cycle	
	duration and the Time-Averaged Velocity (T \times TAV)	31
2.3	Visual representation of equation (2.4) (purple line), revealing a	
	positive correlation between PI and RI. The orange line corre-	
	sponds to $y = x$	32
2.4	(A) PSV (left) and PI (right) histograms of the 22nd week group.	
	(B) PSV (left) and PI (right) histograms of the 30th week group.	
	The presented graphs reflect on statistically significant variations.	33
2.5	(A) PSV (left) and PI (right) normal Q-Q plots of the 22nd	
	week group. (B) PSV (left) and PI (right) normal Q-Q plots of	
	the 30th week group.	34
2.6	Uterine (left) and umbilical (right) PSV percentiles of the 22nd	
	and 30th week groups	35
2.7	Graphic representation of the Euler and Lagrange descriptions	38
2.8	Graphical representation of the local transformation from a phys-	
	ical (GCC) to a transformed (orthogonal) domain.	45
2.9	The centroid cube for discretization using FVM. The schematic	
	appears identical to the two-dimensional case when viewed from	
	-l	40

2.10 A straight cylindrical pipe filled with a fluid of density ρ and	
viscosity μ . The flow is laminar, axisymmetric and parallel to the	
<i>x</i> -axis	49
2.11 $\Delta p(r)$ for different Q, for $L=1$ and $\mu=0.01$	50
2.12 Velocity profiles for different values of Wo. The parabolic profile	
originates from the HP flow	53
2.13 The dicrotic notch, between the phases of systolic and diastolic	
flow, in the formation of the uterine arterial pulse	54
2.14 Velocity distribution and secondary flow patterns in the umbilical	
artery, obtained through our CFD analysis (more in the Results	
section). The top part illustrates the helical velocity profile, while	
the bottom one highlights vortex formation along the curvature.	
The inset on the left shows a cross-sectional view of the velocity	
distribution, revealing a characteristic secondary Dean flow pattern	. 55
2.15 The geometries representing the uterine and umbilical arteries	
(A) were modeled based on real anatomical structures observed	
in Doppler ultrasound images (B) (GE Healthcare). A cylindrical	
pipe geometry was selected for the uterine artery, while a helical	
pipe geometry was chosen for the umbilical artery	58
2.16 Inlet velocity waveforms: From the obtained medical ultrasound	
data to periodic Fourier waveforms	60
2.17 Schematic outline of the uterine arterial flow setup, with the flow	
parameters determined through literature 1, 2, 3	60
2.18 Schematic outline of the umbilical arterial flow setup, with the	
flow parameters determined through literature [4, 5, 6]	61
2.19 Blood flow in the uterine artery, during the $21-22$ week groups.	63
2.20 Comparison of the FSI method with the KdVB mathematical	
model, throughout the entire cardiac cycle (T) . The values for	
the KdVB equation, that provide similar results with the FSI	
equations, are $\alpha = 10^{-3}$, $\beta = 10^{-4}$, and $\gamma = 1$	65
2.21 Visualization of secondary flow in the helical umbilical artery model	. 67
2.22 (A) Simulation of blood flow in the umbilical artery, during the	
21-22 week groups (second trimester). The helical flow pattern is	
evident, reflecting the artery's coiled structure. (B) Simulation of	
blood flow in the umbilical artery, during the 30-31 week groups	
(third trimester).	68
2.23 Time-averaged wall shear stress (TAWSS) distribution in the um-	
bilical artery during the 2nd (\mathbf{A}) and 3rd trimester (\mathbf{B}) of pregnancy	69
3.1 Περιληπτική παρουσίαση της μεθοδολογίας που υιοθετήθηκε για	=-
την εκπόνηση της μελέτης.	79

List of Tables

1	List of Abbreviations used in the study	23
2	List of Notations used in the study	24
2.1	The main Doppler ultrasound parameters considered in our analysis.	30
2.2	PSV percentiles in the umbilical artery and uterine arteries	35
2.3	CFD-obtained measurements for the uterine artery (21–22 weeks).	62
2.4	CFD-obtained measurements for the umbilical artery, correspond-	
	ing to the second trimester of pregnancy (21–22 weeks) and the	
	third trimester of pregnancy $(30-31 \text{ weeks})$	65

Abbreviations & Notations

The following abbreviations are used in this study:

Table 1: List of Abbreviations used in the study.

Abbreviation	Meaning
Acc	Acceleration (Rate of increase in velocity during acceleration phase)
AccT	Acceleration Time (Time to reach peak systolic velocity from start of systole)
CFD	Computational Fluid Dynamics
Dec	Deceleration (Rate of decrease in velocity after peak systole)
DecT	Deceleration Time (Time for velocity to decline after peak systole)
EDV	End-Diastolic Velocity (Blood flow velocity at end of diastole)
FGR	Fetal Growth Restriction
FSI	Fluid-Structure Interaction
FVM	Finite Volume Method
GCC	Generalized Curvilinear Coordinates
HP	Hagen-Poiseuille
IUGR	Intrauterine Growth Restriction
KdVB	Korteweg de Vries-Burgers
MDV	Mid-Diastolic Velocity (Blood flow velocity during the mid-diastolic phase)
MRI	Magnetic Resonance Imaging
NS	Navier-Stokes
OSI	Oscillatory Shear Index
PDE	Partial Differential Equation
PGmax	Maximum Pressure Gradient (calculated from velocity)
PGmean	Mean Pressure Gradient (Average pressure difference across the cardiac cycle)
PI	Pulsatility Index
PSV	Peak Systolic Velocity (Maximum blood flow velocity during systole)
RI	Resistance Index
RRT	Relative Residence Time
$\mathrm{S/D}$	Systolic/Diastolic Ratio
TAmax	Time-Averaged Maximum Velocity (Average of the maximum velocities through-
	out the cardiac cycle)
TAV (or TAmean)	Time-Averaged Velocity (Average velocity over the entire cardiac cycle)

Continued on next page

Table 1 – continued from previous page

Abbreviation	Meaning
TAWSS	Time-Averaged Wall Shear Stress
UCI	Umbilical Coiling Index
UmbA	Umbilical Artery
$\mathrm{Ut}\mathrm{A}$	Uterine Artery
WSS	Wall Shear Stress

The following notations are used in this study:

Table 2: List of Notations used in the study.

Notation Meaning c Ultrasound propagation velocity De Dean number L Length n Power-law index p Pressure Q Volumetric flow rate R Radius R_c Radius of curvature Re Reynolds number T Period (cardiac cycle) v_b Propagation velocity of blood cells Wo Womersley number F Force field q Velocity field ω Vorticity $\nabla_{\mathbf{x}}$ Spatial gradient $\Delta_{\mathbf{x}}$ Spatial Laplacian $\vec{\tau}_w(t)$ Instantaneous wall shear stress vector at time t $\dot{\gamma}$ Shear rate ϑ Angle of insonation λ Relaxation time constant μ Dynamic viscosity $\mu(\dot{\gamma})$ Viscosity at $\dot{\gamma}$ μ_0 Zero-shear viscosity		Table 2: List of Notations used in the study.
De Dean number L Length n Power-law index p Pressure Q Volumetric flow rate R Radius R_c Radius of curvature Re Reynolds number Re_c Critical Reynolds number T Period (cardiac cycle) v_b Propagation velocity of blood cells Wo Womersley number F Force field q Velocity field ω Vorticity $\nabla_{\mathbf{x}}$ Spatial gradient $\Delta_{\mathbf{x}}$ Spatial Laplacian $\vec{\tau}_w(t)$ Instantaneous wall shear stress vector at time t $\dot{\gamma}$ Shear rate ϑ Angle of insonation λ Relaxation time constant μ Dynamic viscosity $\mu(\dot{\gamma})$ Viscosity at $\dot{\gamma}$ μ_0 Zero-shear viscosity	Notation	Meaning
L Length n Power-law index p Pressure Q Volumetric flow rate R Radius R_c Radius of curvature Re Reynolds number Re $_c$ Critical Reynolds number T Period (cardiac cycle) v_b Propagation velocity of blood cells Wo Womersley number F Force field Q Velocity field ω Vorticity $\nabla_{\mathbf{x}}$ Spatial gradient $\Delta_{\mathbf{x}}$ Spatial Laplacian $\vec{\tau}_w(t)$ Instantaneous wall shear stress vector at time t $\dot{\gamma}$ Shear rate ϑ Angle of insonation λ Relaxation time constant μ Dynamic viscosity $\mu(\dot{\gamma})$ Viscosity at $\dot{\gamma}$ μ_0 Zero-shear viscosity	c	Ultrasound propagation velocity
n Power-law index p Pressure Q Volumetric flow rate R Radius R_c Radius of curvature Re Reynolds number Re_c Critical Reynolds number T Period (cardiac cycle) v_b Propagation velocity of blood cells Wo Womersley number F Force field q Velocity field ω Vorticity $\nabla_{\mathbf{x}}$ Spatial gradient $\Delta_{\mathbf{x}}$ Spatial Laplacian $\vec{\tau}_w(t)$ Instantaneous wall shear stress vector at time t $\dot{\gamma}$ Shear rate ϑ Angle of insonation λ Relaxation time constant μ Dynamic viscosity $\mu(\dot{\gamma})$ Viscosity at $\dot{\gamma}$ μ_0 Zero-shear viscosity	De	Dean number
p Pressure Q Volumetric flow rate R Radius R_c Radius of curvature Re Reynolds number Re_c Critical Reynolds number T Period (cardiac cycle) v_b Propagation velocity of blood cells Wo Womersley number F Force field q Velocity field ω Vorticity $\nabla_{\mathbf{x}}$ Spatial gradient $\Delta_{\mathbf{x}}$ Spatial Laplacian $\vec{\tau}_w(t)$ Instantaneous wall shear stress vector at time t $\dot{\gamma}$ Shear rate ϑ Angle of insonation λ Relaxation time constant μ Dynamic viscosity $\mu(\dot{\gamma})$ Viscosity at $\dot{\gamma}$ μ_0 Zero-shear viscosity	\mathbf{L}	Length
Q Volumetric flow rate R Radius R_c Radius of curvature Re Reynolds number Re _c Critical Reynolds number T Period (cardiac cycle) v_b Propagation velocity of blood cells Wo Womersley number F Force field q Velocity field ω Vorticity $\nabla_{\mathbf{x}}$ Spatial gradient $\Delta_{\mathbf{x}}$ Spatial Laplacian $\vec{\tau}_w(t)$ Instantaneous wall shear stress vector at time t $\dot{\gamma}$ Shear rate ϑ Angle of insonation λ Relaxation time constant μ Dynamic viscosity $\mu(\dot{\gamma})$ Viscosity at $\dot{\gamma}$ μ_0 Zero-shear viscosity	n	Power-law index
R Radius R_c Radius of curvature Re Reynolds number Re _c Critical Reynolds number T Period (cardiac cycle) v_b Propagation velocity of blood cells Wo Womersley number F Force field q Velocity field ω Vorticity $\nabla_{\mathbf{x}}$ Spatial gradient $\Delta_{\mathbf{x}}$ Spatial Laplacian $\vec{\tau}_w(t)$ Instantaneous wall shear stress vector at time t $\dot{\gamma}$ Shear rate ϑ Angle of insonation λ Relaxation time constant μ Dynamic viscosity $\mu(\dot{\gamma})$ Viscosity at $\dot{\gamma}$ μ_0 Zero-shear viscosity	p	Pressure
$\begin{array}{lll} R_c & \text{Radius of curvature} \\ \text{Re} & \text{Reynolds number} \\ \text{Re}_c & \text{Critical Reynolds number} \\ \text{T} & \text{Period (cardiac cycle)} \\ v_b & \text{Propagation velocity of blood cells} \\ \text{Wo} & \text{Womersley number} \\ \text{F} & \text{Force field} \\ \text{q} & \text{Velocity field} \\ \omega & \text{Vorticity} \\ \nabla_{\textbf{x}} & \text{Spatial gradient} \\ \Delta_{\textbf{x}} & \text{Spatial Laplacian} \\ \vec{\tau}_w(t) & \text{Instantaneous wall shear stress vector at time } t \\ \dot{\gamma} & \text{Shear rate} \\ \vartheta & \text{Angle of insonation} \\ \lambda & \text{Relaxation time constant} \\ \mu & \text{Dynamic viscosity} \\ \mu(\dot{\gamma}) & \text{Viscosity at } \dot{\gamma} \\ \mu_0 & \text{Zero-shear viscosity} \\ \end{array}$	Q	Volumetric flow rate
Re Reynolds number Re _c Critical Reynolds number T Period (cardiac cycle) v_b Propagation velocity of blood cells Wo Womersley number F Force field q Velocity field ω Vorticity $\nabla_{\mathbf{x}}$ Spatial gradient $\Delta_{\mathbf{x}}$ Spatial Laplacian $\vec{\tau}_w(t)$ Instantaneous wall shear stress vector at time t $\dot{\gamma}$ Shear rate ϑ Angle of insonation λ Relaxation time constant μ Dynamic viscosity $\mu(\dot{\gamma})$ Viscosity at $\dot{\gamma}$ μ_0 Zero-shear viscosity	R	Radius
$\begin{array}{lll} \operatorname{Re}_c & \operatorname{Critical\ Reynolds\ number} \\ \operatorname{T} & \operatorname{Period\ (cardiac\ cycle)} \\ v_b & \operatorname{Propagation\ velocity\ of\ blood\ cells} \\ \operatorname{Wo} & \operatorname{Womersley\ number} \\ \operatorname{F} & \operatorname{Force\ field} \\ \operatorname{\mathbf{q}} & \operatorname{Velocity\ field} \\ \omega & \operatorname{Vorticity} \\ \nabla_{\mathbf{x}} & \operatorname{Spatial\ gradient} \\ \Delta_{\mathbf{x}} & \operatorname{Spatial\ Laplacian} \\ \bar{\tau}_w(t) & \operatorname{Instantaneous\ wall\ shear\ stress\ vector\ at\ time\ t} \\ \dot{\gamma} & \operatorname{Shear\ rate} \\ \vartheta & \operatorname{Angle\ of\ insonation} \\ \lambda & \operatorname{Relaxation\ time\ constant} \\ \mu & \operatorname{Dynamic\ viscosity} \\ \mu(\dot{\gamma}) & \operatorname{Viscosity\ at\ } \dot{\gamma} \\ \mu_0 & \operatorname{Zero-shear\ viscosity} \\ \end{array}$	R_c	Radius of curvature
T Period (cardiac cycle) v_b Propagation velocity of blood cells Wo Womersley number F Force field q Velocity field ω Vorticity $\nabla_{\mathbf{x}}$ Spatial gradient $\Delta_{\mathbf{x}}$ Spatial Laplacian $\vec{\tau}_w(t)$ Instantaneous wall shear stress vector at time t $\dot{\gamma}$ Shear rate ϑ Angle of insonation λ Relaxation time constant μ Dynamic viscosity $\mu(\dot{\gamma})$ Viscosity at $\dot{\gamma}$ μ_0 Zero-shear viscosity	Re	Reynolds number
$\begin{array}{lll} v_b & \operatorname{Propagation velocity} \text{ of blood cells} \\ Wo & \operatorname{Womersley number} \\ \mathbf{F} & \operatorname{Force} \text{ field} \\ \mathbf{q} & \operatorname{Velocity} \text{ field} \\ \omega & \operatorname{Vorticity} \\ \nabla_{\mathbf{x}} & \operatorname{Spatial gradient} \\ \Delta_{\mathbf{x}} & \operatorname{Spatial Laplacian} \\ \vec{\tau}_w(t) & \operatorname{Instantaneous wall shear stress vector at time } t \\ \dot{\gamma} & \operatorname{Shear rate} \\ \vartheta & \operatorname{Angle of insonation} \\ \lambda & \operatorname{Relaxation time constant} \\ \mu & \operatorname{Dynamic viscosity} \\ \mu(\dot{\gamma}) & \operatorname{Viscosity at } \dot{\gamma} \\ \mu_0 & \operatorname{Zero-shear viscosity} \\ \end{array}$	Re_c	Critical Reynolds number
Wo Womersley number \mathbf{F} Force field \mathbf{q} Velocity field ω Vorticity $\nabla_{\mathbf{x}}$ Spatial gradient $\Delta_{\mathbf{x}}$ Spatial Laplacian $\vec{\tau}_w(t)$ Instantaneous wall shear stress vector at time t $\dot{\gamma}$ Shear rate ϑ Angle of insonation λ Relaxation time constant μ Dynamic viscosity $\mu(\dot{\gamma})$ Viscosity at $\dot{\gamma}$ μ_0 Zero-shear viscosity	${ m T}$	Period (cardiac cycle)
$ \begin{array}{lll} \mathbf{F} & \text{Force field} \\ \mathbf{q} & \text{Velocity field} \\ \omega & \text{Vorticity} \\ \nabla_{\mathbf{x}} & \text{Spatial gradient} \\ \Delta_{\mathbf{x}} & \text{Spatial Laplacian} \\ \vec{\tau}_w(t) & \text{Instantaneous wall shear stress vector at time } t \\ \dot{\gamma} & \text{Shear rate} \\ \vartheta & \text{Angle of insonation} \\ \lambda & \text{Relaxation time constant} \\ \mu & \text{Dynamic viscosity} \\ \mu(\dot{\gamma}) & \text{Viscosity at } \dot{\gamma} \\ \mu_0 & \text{Zero-shear viscosity} \\ \end{array} $	v_b	Propagation velocity of blood cells
$\begin{array}{lll} \mathbf{q} & \text{Velocity field} \\ \omega & \text{Vorticity} \\ \nabla_{\mathbf{x}} & \text{Spatial gradient} \\ \Delta_{\mathbf{x}} & \text{Spatial Laplacian} \\ \vec{\tau}_w(t) & \text{Instantaneous wall shear stress vector at time } t \\ \dot{\gamma} & \text{Shear rate} \\ \vartheta & \text{Angle of insonation} \\ \lambda & \text{Relaxation time constant} \\ \mu & \text{Dynamic viscosity} \\ \mu(\dot{\gamma}) & \text{Viscosity at } \dot{\gamma} \\ \mu_0 & \text{Zero-shear viscosity} \end{array}$	Wo	Womersley number
$\begin{array}{lll} \omega & \text{Vorticity} \\ \nabla_{\mathbf{x}} & \text{Spatial gradient} \\ \Delta_{\mathbf{x}} & \text{Spatial Laplacian} \\ \vec{\tau}_w(t) & \text{Instantaneous wall shear stress vector at time } t \\ \dot{\gamma} & \text{Shear rate} \\ \vartheta & \text{Angle of insonation} \\ \lambda & \text{Relaxation time constant} \\ \mu & \text{Dynamic viscosity} \\ \mu(\dot{\gamma}) & \text{Viscosity at } \dot{\gamma} \\ \mu_0 & \text{Zero-shear viscosity} \\ \end{array}$	${f F}$	Force field
$\begin{array}{lll} \nabla_{\mathbf{x}} & \text{Spatial gradient} \\ \Delta_{\mathbf{x}} & \text{Spatial Laplacian} \\ \vec{\tau}_w(t) & \text{Instantaneous wall shear stress vector at time } t \\ \dot{\gamma} & \text{Shear rate} \\ \vartheta & \text{Angle of insonation} \\ \lambda & \text{Relaxation time constant} \\ \mu & \text{Dynamic viscosity} \\ \mu(\dot{\gamma}) & \text{Viscosity at } \dot{\gamma} \\ \mu_0 & \text{Zero-shear viscosity} \end{array}$	${f q}$	Velocity field
$\begin{array}{lll} \Delta_{\mathbf{x}} & \text{Spatial Laplacian} \\ \vec{\tau}_w(t) & \text{Instantaneous wall shear stress vector at time } t \\ \dot{\gamma} & \text{Shear rate} \\ \vartheta & \text{Angle of insonation} \\ \lambda & \text{Relaxation time constant} \\ \mu & \text{Dynamic viscosity} \\ \mu(\dot{\gamma}) & \text{Viscosity at } \dot{\gamma} \\ \mu_0 & \text{Zero-shear viscosity} \end{array}$	ω	Vorticity
$\vec{\tau}_w(t)$ Instantaneous wall shear stress vector at time t $\dot{\gamma}$ Shear rate ϑ Angle of insonation λ Relaxation time constant μ Dynamic viscosity $\mu(\dot{\gamma})$ Viscosity at $\dot{\gamma}$ μ_0 Zero-shear viscosity	$ abla_{\mathbf{x}}$	Spatial gradient
$\dot{\gamma}$ Shear rate ϑ Angle of insonation λ Relaxation time constant μ Dynamic viscosity $\mu(\dot{\gamma})$ Viscosity at $\dot{\gamma}$ μ_0 Zero-shear viscosity		Spatial Laplacian
ϑ Angle of insonation λ Relaxation time constant μ Dynamic viscosity $\mu(\dot{\gamma})$ Viscosity at $\dot{\gamma}$ μ_0 Zero-shear viscosity	$\vec{ au}_w(t)$	Instantaneous wall shear stress vector at time t
λ Relaxation time constant μ Dynamic viscosity $\mu(\dot{\gamma})$ Viscosity at $\dot{\gamma}$ μ_0 Zero-shear viscosity	$\dot{\gamma}$	Shear rate
μ Dynamic viscosity $\mu(\dot{\gamma})$ Viscosity at $\dot{\gamma}$ μ_0 Zero-shear viscosity	ϑ	Angle of insonation
$\mu(\dot{\gamma})$ Viscosity at $\dot{\gamma}$ μ_0 Zero-shear viscosity	λ	Relaxation time constant
μ_0 Zero-shear viscosity	μ	Dynamic viscosity
• •	$\mu(\dot{\gamma})$	Viscosity at $\dot{\gamma}$
T 0 4: 1	μ_0	Zero-shear viscosity
μ_{∞} Infinite-shear viscosity	μ_{∞}	Infinite-shear viscosity
ν Kinematic viscosity	ν	Kinematic viscosity
ρ Density	ρ	v
Ψ Stream function	Ψ	Stream function

Chapter 1

Introduction

1.1 Literature review

Uterine arterial blood flow plays a critical role in maintaining the health of both mother and fetus throughout pregnancy. Impairments in uteroplacental circulation have been strongly associated with serious complications such as pre-eclampsia and intrauterine growth restriction (IUGR). Pre-eclampsia affects approximately 2-8% of pregnancies worldwide, with higher prevalence observed in low- and middle-income countries 7. Likewise, IUGR impacts about 20–25% of pregnancies globally 8. Understanding the hemodynamics of uterine and umbilical arteries is, therefore, vital for the early diagnosis and management of these conditions.

The uterine arteries supply oxygenated blood to the placenta, while the umbilical cord, composed of one vein and two arteries surrounded by Wharton's jelly, facilitates nutrient and waste exchange between mother and fetus. Specifically, the umbilical vein delivers oxygen and nutrients to the fetus, while the umbilical arteries transport deoxygenated blood back to the placenta. The unique anatomical and physiological features of these vessels, including the helical geometry of the umbilical arteries, influence blood flow patterns and fetal development [4].

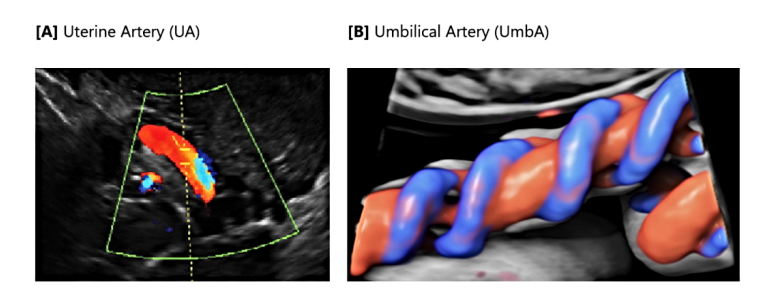


Figure 1.1: [A] Uterine and [B] umbilical arterial geometries.

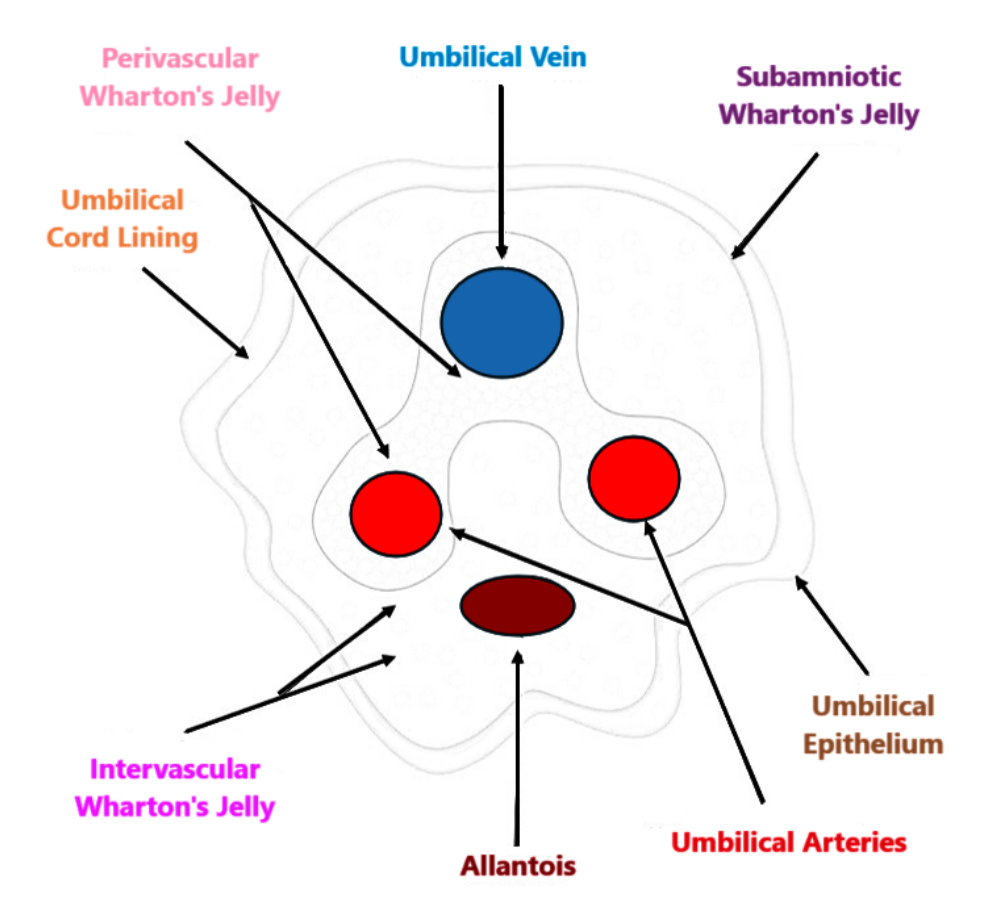


Figure 1.2: Cross-sectional anatomy of the umbilical cord, displaying the arrangement of the umbilical vein, umbilical arteries, Wharton's Jelly, and surrounding structures. The umbilical vein (blue) carries oxygenated blood from the placenta to the fetus, while the umbilical arteries (red) transport deoxygenated blood back to the placenta. Wharton's Jelly, a gelatinous substance, provides structural support and protects these vessels.

Computational fluid dynamics (CFD) has emerged as a powerful tool to investigate the complex blood flow characteristics within these arteries. Rooted in the mathematical framework of the Navier–Stokes equations, CFD models can capture the influence of vessel geometry, blood rheology, and flow conditions on hemodynamic parameters [9]. In this study, we specifically use Doppler ultrasound data acquired from Greek pregnant women to construct image-based geometries for CFD analysis, thereby linking physiological measurements with engineering simulations. Doppler ultrasound, the imaging modality employed here, is widely used clinically to monitor blood flow velocities non-invasively, providing critical input data for modeling.

Previous research using CFD has demonstrated important insights into

maternal-fetal circulation. For example, uterine artery dilation and increased blood velocity correlate with better fetal nourishment [10]. Investigations into umbilical cord morphology have shown that hypercoiling reduces blood flow velocity, potentially impairing oxygen supply [11]. Additionally, the spiral configuration of the umbilical arteries contributes to fetal-maternal heat exchange and thermal regulation [4]. Despite these advances, gaps remain in integrating real-time clinical data within CFD frameworks and in studying distinct populations such as Greek pregnant women.

1.2 Scope of the study

This study combines Doppler ultrasound imaging with three-dimensional CFD simulations to assess critical hemodynamic indices, including Wall Shear Stress (WSS), Oscillatory Shear Index (OSI), and Relative Residence Time (RRT) [12] [13], [14], [15]. Briefly, WSS quantifies tangential forces exerted by blood flow on the vessel wall; OSI measures directional changes in shear stress, related to disturbed flow and RRT estimates the residence time of blood near the wall, linked to vascular risks. These parameters serve as markers for vascular health and potential predictors of pregnancy complications.

Importantly, this work analyzes a previously understudied population by using real-time Doppler ultrasound data from Greek pregnant women, offering novel insights with potential clinical implications. We frame our objectives as follows: (1) to develop CFD models using Doppler data from Greek pregnant women; (2) to characterize uterine and umbilical arterial hemodynamics with detailed flow and shear stress metrics; (3) to identify flow abnormalities associated with adverse pregnancy outcomes in this cohort. To clarify the overall workflow of the present study, a schematic diagram illustrating the main steps of the methodology is presented in Figure [1.3]

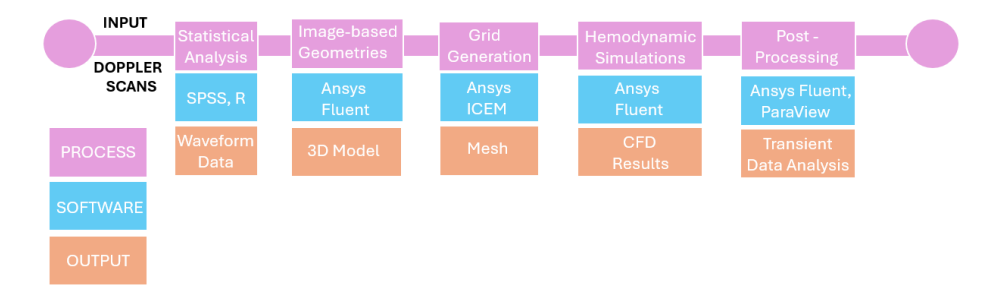


Figure 1.3: Schematic overview of the study methodology.

Chapter 2

Main Body

2.1 Materials and Methods

This section discusses the use of Doppler ultrasound to assess blood flow to the uterine arteries and umbilical arteries during pregnancy, as well as the mathematical modeling of transient blood flow by CFD. Since this work will ultimately provide guidance in designing vessels with flow conditions relevant to real life, the model used will represent laminar, incompressible and non-Newtonian flow governed by the Navier–Stokes equations, so it will be necessary to use a coordinate system appropriate for the complex geometry of the vessels. Equations are discretized using the finite-volume method (FVM). Exact flow models are also presented. The results obtained are discussed, and comparisons are made with those in the current literature.

2.1.1 Doppler ultrasonography

Doppler ultrasonography provides important information on the dynamics of blood flow in the uterine and umbilical arteries in pregnant women. Its use enables one to measure the changes in frequency of ultrasound waves reflected from moving blood cells, allowing one to determine the velocity and direction of blood flow. This shift of frequency is given by:

$$\Delta f = \frac{2v_b \cos \theta}{c} f_0 \tag{2.1}$$

where:

- v_b : propagation velocity of blood cells
- c: ultrasound propagation velocity
- θ : angle of the ultrasound beam relative to blood cells

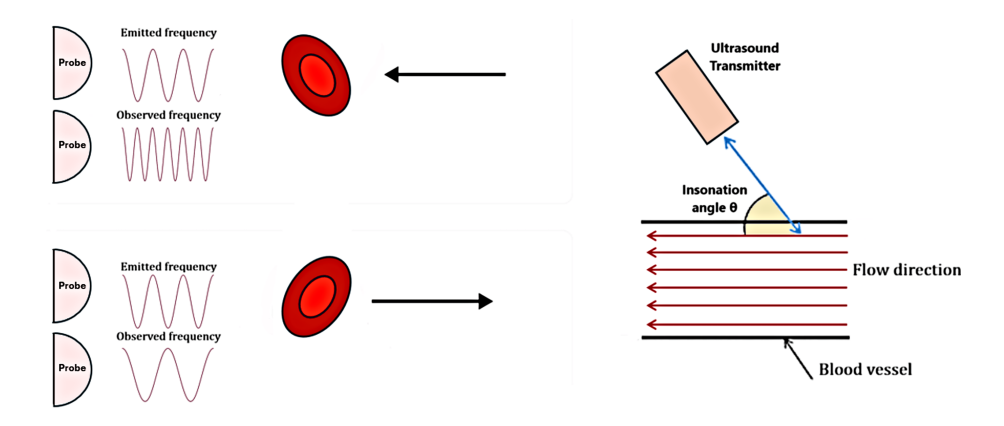


Figure 2.1: Schematic explanation of the Doppler ultrasound mechanism.

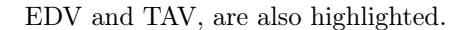
Typically, an insonation angle of less than 60° is used to provide accurate velocity estimates.

In the uterine artery, medical experts utilize the Doppler effect to evaluate maternal blood supply to the placenta, which is essential for fetal development and general health during pregnancy. In the umbilical artery, Doppler measurements assess fetal blood circulation and can indicate potential issues such as placental insufficiency or fetal distress. This noninvasive technique allows for real-time monitoring of blood flow, contributing to the early detection of potential complications and guiding clinical management. When combined with CFD, Doppler ultrasound data can be used to create detailed simulations of blood flow, offering a deeper understanding of the hemodynamic environment and enhancing diagnostic accuracy [16]. Key Doppler ultrasound parameters that influenced our analysis are summarized in Table [2.1]

Doppler Ultrasound Parameters & Significance						
Parameter	Significance					
PSV	Indicates the force and efficiency of blood flow during heartbeat.					
EDV	Assesses resistance in downstream vessels; low or absent EDV suggests higher resistance or pathology.					
MDV	Provides additional insight into diastolic flow dynamics; can show mid-diastolic forward flow and may relate to ventricular relaxation patterns.					
TAmax	Reflects the average peak flow velocities over time.					
TAmean (or TAV)	Used to estimate overall volumetric blood flow in the vessel.					
PGmax	Indicates peak pressure gradient driving flow.					
PGmean	Reflects average pressure load against vessel resistance.					
AccT	Shorter AccT may indicate stiffer vessels or abnormal flow.					
Acc	Helps evaluate vessel compliance and cardiac function.					
DecT	Longer DecT may indicate impaired downstream resistance.					
Dec	Assesses vascular compliance during flow reduction.					
PI	Reflects vascular resistance; higher PI indicates increased resistance.					
RI	Indicates downstream resistance; higher RI means higher resistance.					
S/D	Another index of vascular resistance and compliance.					

Table 2.1: The main Doppler ultrasound parameters considered in our analysis.

Figure 2.2 illustrates the typical waveform of arterial blood flow velocity during a cardiac cycle, as measured by Doppler ultrasound. The vertical axis represents blood flow velocity (in cm/s), while the horizontal axis corresponds to time over one complete cardiac cycle (T). Key parameters, like PSV, MDV,



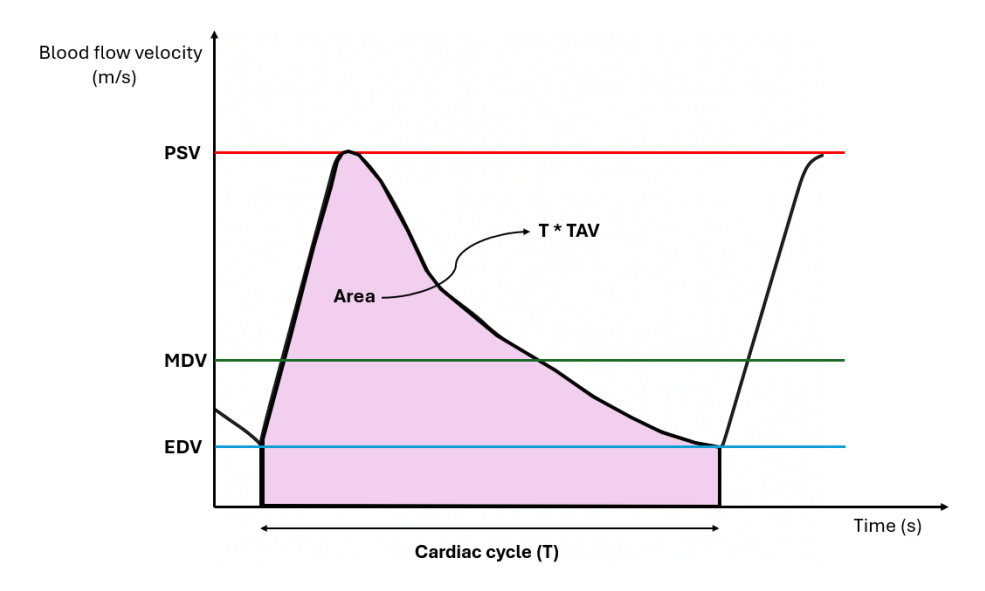


Figure 2.2: Waveform representation of blood flow velocity across a cardiac cycle, illustrating key Doppler ultrasound parameters: Peak Systolic Velocity (PSV), Mid-Diastolic Velocity (MDV) and End-Diastolic Velocity (EDV). The shaded area under the curve reflects the total flow during one cycle, corresponding to the product of cycle duration and the Time-Averaged Velocity (T \times TAV).

Both uterine and umbilical arterial blood flows are inherently pulsatile. This pulsatility is a fundamental property of the cardiovascular system, arising from the varying resistance within the arteriolar network. Such resistance differences allow the potential energy stored in the elastic proximal arteries to be transmitted through the microcirculation at a mean pressure sufficient to maintain adequate tissue perfusion. The pulsatility index PI, also known as the Gosling index, is a calculated flow parameter in ultrasound, derived from the maximum, minimum, and mean Doppler frequency changes during a specific cardiac cycle. It is commonly used, along with the resistance index RI, to evaluate resistance in a pulsatile vascular system . When assessed as a derived flow parameter using pulsed wave Doppler, PI is calculated as,

$$PI = \frac{\text{Peak Systolic Velocity (PSV)} - \text{End Diastolic Velocity (EDV)}}{\text{Time Averaged Velocity (TAV)}}$$
 (2.2)

The resistance index RI, also known as the Pourcelot index, is one of the most commonly used vascular ultrasound indices due to its simplicity. It is influenced by both vascular resistance and vascular compliance. As the vessel narrows and the resistance to flow increases, RI also increases. It is a flow parameter calculated by ultrasound, derived from the maximum and minimum Doppler

frequency shifts during a cardiac cycle. The formula to express RI is,

$$RI = \frac{PSV - EDV}{PSV}$$
 (2.3)

One can combine (2.2) and (2.3) to obtain:

$$PI = \frac{PSV}{TAV} \times RI \tag{2.4}$$

The latter shows that since PSV is always greater than TAV, PI is always greater than RI. It also reveals a linear relationship between the two.

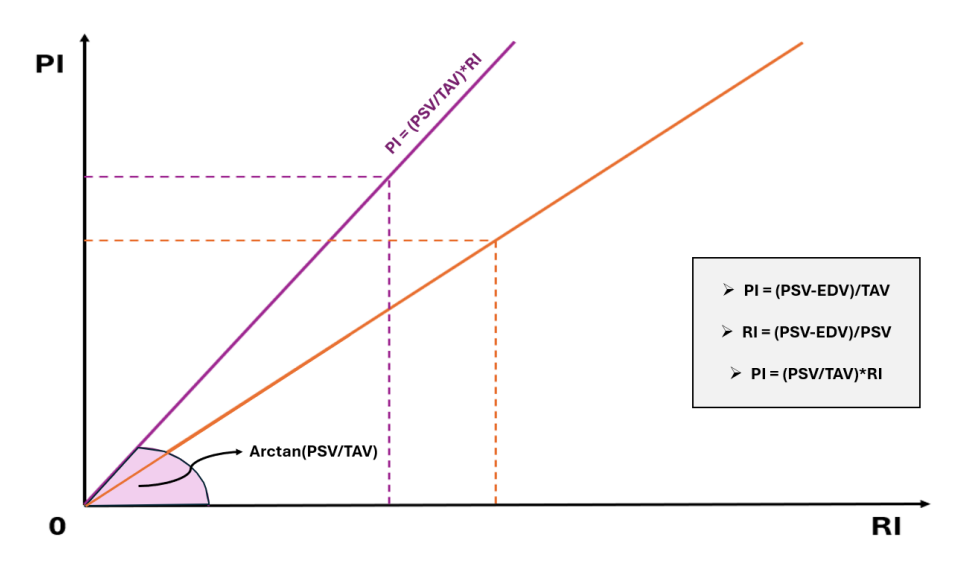


Figure 2.3: Visual representation of equation (2.4) (purple line), revealing a positive correlation between PI and RI. The orange line corresponds to y = x.

2.1.2 Statistical analysis of ultrasound data

A large cohort of more than 200 pregnant women, during the second and third trimesters of pregnancy, was examined using Doppler ultrasound. Key parameters of umbilical and uterine arterial flows were statistically analyzed. More specifically, four independent groups were studied, corresponding to the 21st, 22nd, 30th and 31st weeks of gestation, respectively.

The goal was to assess any statistically significant differences among these weeks, primarily with respect to four markers: Doppler input velocities (PSV, EDV), PI and RI. A significance level 5% was used and outliers, whose number did not exceed 10% of the category size, were removed. In each group, the four markers were adequately represented by a normal distribution. Furthermore, t-tests were performed to evaluate statistically significant differences between

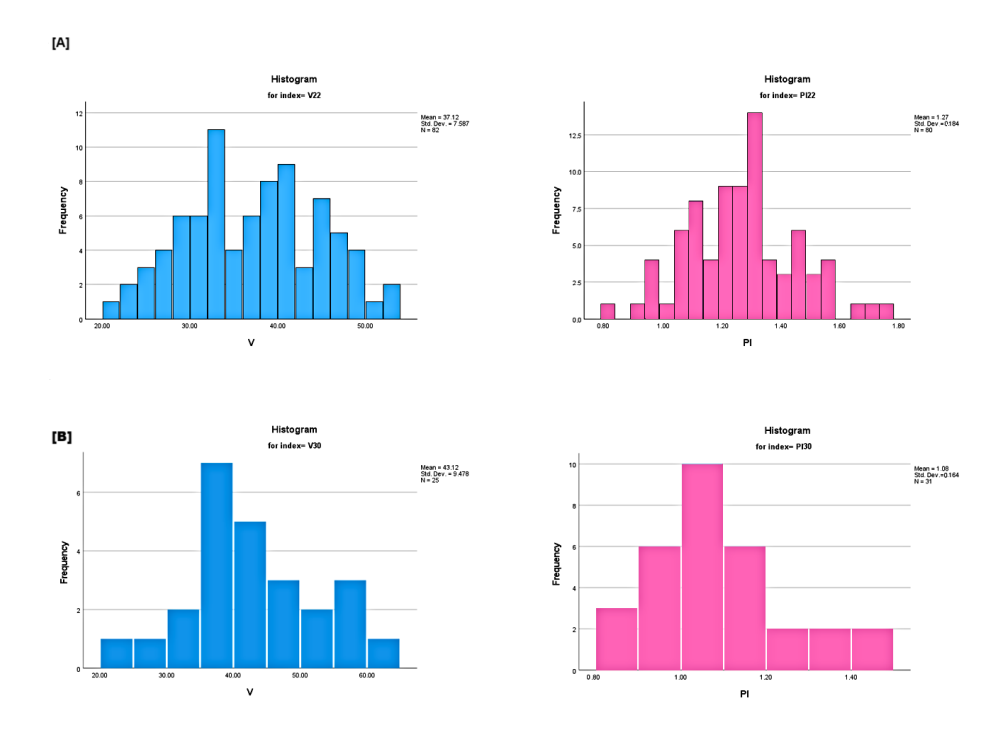


Figure 2.4: (A) PSV (left) and PI (right) histograms of the 22nd week group. (B) PSV (left) and PI (right) histograms of the 30th week group. The presented graphs reflect on statistically significant variations.

the groups. Figures 2.4 and 2.5 present histograms and Q-Q plots related to the statistical analysis.

To the best of our knowledge, this study presents the first analysis conducted using data from Greek pregnant women. It significantly contributes to region-specific knowledge, particularly in understanding how health outcomes vary between populations due to genetic, environmental, and health factors. Valuable insights are provided on how these variables influence maternal and fetal health in Greece. The results may serve as a baseline for Greek healthcare providers by setting local reference values for umbilical and uterine arterial flow parameters. Any slight difference between these standards and the international norms could make the findings particularly useful for practitioners in Greece. In addition, it could pave the way for more research on how lifestyle, diet and regional healthcare practice influence pregnancy outcomes, potentially inspiring larger studies in various regions of the country. The conducted analysis led to the following results:

• No statistically significant differences were observed in velocities between the 21st and 22nd week groups for both uterine and umbilical arteries. The same held for the velocities between the 30th and 31st week groups.

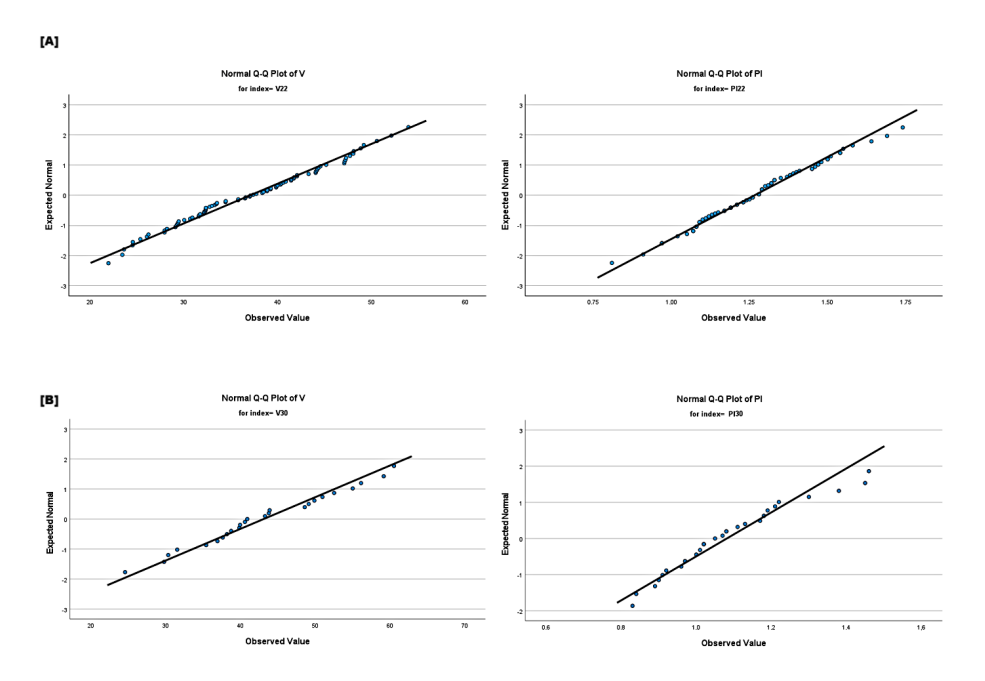


Figure 2.5: (A) PSV (left) and PI (right) normal Q-Q plots of the 22nd week group. (B) PSV (left) and PI (right) normal Q-Q plots of the 30th week group.

Statistically significant differences were observed in umbilical artery velocities between the 22nd and 30th week groups. No such differences were observed in the velocities of the uterine arteries.

• Statistically significant reductions in biomarkers PI and RI were observed between the second-trimester groups for the uterine and umbilical arteries. No statistically significant differences were found in the two biomarkers of the uterine and umbilical arteries between the third trimester groups, indicating that the reductions observed during the second trimester tend to stabilize in the third trimester.

The formulae for PI and RI, which relate the four markers, can be used to derive correlations among these categories (see equations (2.2), (2.3) and (2.4)). Table 2.2 presents the PSV percentiles in the two arteries, umbilical and uterine, at two different gestational weeks, the 22nd (Umb22, Ut22) and the 30th (Umb30, Ut30) weeks of pregnancy. The inlet velocities are presented as percentiles. The 0th percentile represents the minimum value of PSV, while the 100th percentile represents the maximum value in the population. The 50th percentile (median) represents the middle value, where half the population has a PSV below this value and the other half has values above. The 25th and 75th percentiles (lower and upper quartiles) provide an indication of the variability within the middle 50% of the population. For instance, 50% of women will have a PSV

between the 25th and 75th percentile.

Percentile Velocity	0%	25%	50%	75%	100%
$\mathrm{Umb}22$	21.980	31.700	37.410	42.705	60.780
Umb30	24.60	37.66	40.94	49.91	60.56
Ut22	44.890	70.470	87.090	114.245	164.540
Ut30	47.55	74.31	95.89	118.72	153.86

Table 2.2: PSV percentiles in the umbilical artery and uterine arteries.

Analyzing the percentiles table provides the following crucial insights:

- The PSV at 30 weeks is consistently higher than at 22 weeks across all percentiles. This indicates an increase in blood flow velocity in the umbilical artery as pregnancy progresses, which is biologically plausible given the growing demand for nutrients and oxygen as the fetus develops. The observed, statistically significant difference suggests that the increase in PSV in the umbilical artery with advancing gestation represents a meaningful physiological change.
- Similarly, there is an increase in PSV in the uterine artery from 22 weeks to 30 weeks across all percentiles, though the change is less pronounced compared to the umbilical artery. However, the lack of statistical significance suggests that while an increase in PSV is observed in the uterine artery, this difference is not large or consistent enough across the population to be considered physiologically meaningful at a statistical level.

These percentile values help to assess whether the patient's PSV is within the normal range of their gestational age. Significant deviations, such as PSV below the 25th percentile, could signal potential problems, such as fetal growth restriction (FGR) or placental insufficiency, particularly if the umbilical PSV is too low.

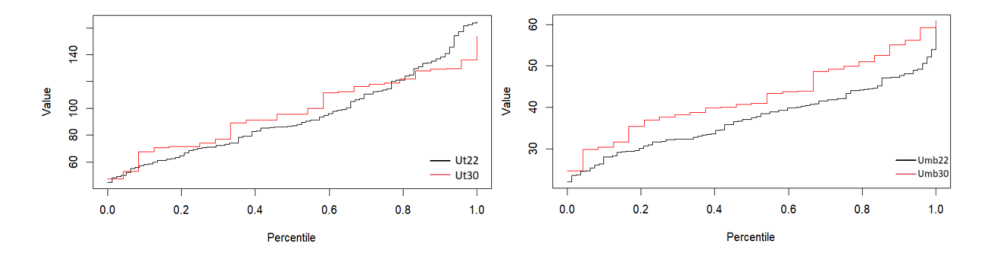


Figure 2.6: Uterine (**left**) and umbilical (**right**) PSV percentiles of the 22nd and 30th week groups.

2.1.3 Mathematical modeling and computational approach Fourier analysis in medicine

Fourier series is one of the important mathematical contributions to medicine. It is used to evaluate periodic phenomena such as the blood flow of the uterine and umbilical arteries during pregnancy. These flows have certain cyclic characteristics that can be analyzed by decomposing them into a series of starts and sine waves using Fourier series. The amplitude of these components can be used to analyze the frequencies contained within the analyzed signal. This identification is important for diagnosing different conditions, for example fetal distress, placental insufficiency, or vascular abnormalities. Quantitative diagnostic methods such as Doppler ultrasound applying the Fourier series of periodic signals have made it possible to monitor maternal and fetal well-being with greater reliability.

Let f = f(t) be a 2T-periodic and L^2 function corresponding to some medical signal. The periodicity requirement is equivalent to,

$$f(t+2T) = f(t), \ \forall \ t \in D_f, \ T > 0$$
 (2.5)

while the L^2 condition requires that,

$$\int_{D_f} |f(t)|^2 dt < \infty \tag{2.6}$$

If (2.5) and (2.6) are met, the corresponding Fourier, N-order, expansion is given as,

$$S_{N,f}(t) := \frac{a_0}{2} + \sum_{n=1}^{N} \left[a_n \cos\left(\frac{n\pi t}{T}\right) + b_n \sin\left(\frac{n\pi t}{T}\right) \right]$$
 (2.7)

while its Fourier series, as,

$$\frac{a_0}{2} + \sum_{n=1}^{\infty} \left[a_n \cos\left(\frac{n\pi t}{T}\right) + b_n \sin\left(\frac{n\pi t}{T}\right) \right] = \lim_{N \to \infty} S_{N,f}(t)$$
 (2.8)

The Fourier coefficients, a_n and b_n , are expressed as,

$$\begin{cases} a_n = \frac{1}{T} \int_{-T}^T f(t) \cos\left(\frac{n\pi t}{T}\right) dt, & n \in \mathbb{N} \cup \{0\} \\ b_n = \frac{1}{T} \int_{-T}^T f(t) \sin\left(\frac{n\pi t}{T}\right) dt, & n \in \mathbb{N} \end{cases}$$
(2.9)

Description of flow

In classical field theories, one finds the Lagrange and Euler descriptions. In the Lagrange description of the flow field, the motion of the fluid is considered, with the observer following a single fluid particle as it moves through space and time 17. Plotting the position of a single fluid particle in time gives the trajectory of the particle. In simpler words, we can visualize the Lagrange description by sitting in a boat and drifting down a river.

The Euler description of the flow field considers the motion of the fluid, focusing on specific positions in the space through which the fluid flows at a time t, without examining which fluid particle is passing through that position [17]. This description can be visualized by sitting on the bank of a river and watching the water pass through a given position.

The Lagrange and Euler descriptions are also found as Lagrange and Euler reference frames, respectively. However, in general, both of these flow field descriptions can be applied to any observer reference frame and any coordinate system used within the chosen reference frame.

The Lagrange and Euler descriptions are commonly used in CFD, where Euler simulations use a fixed grid, while Lagrange simulations have simulation nodes that can move following the flow field.

In the Euler description, the field is represented as a function of position \mathbf{x} and time t. For example, the flow velocity is represented by a function,

$$\mathbf{q}(\mathbf{x},t), \ \mathbf{q}, \mathbf{x} \in \mathbb{R}^n, \ t \ge 0$$
 (2.10)

On the other hand, in the Lagrange description, individual fluid particles are tracked through time. The particles are characterized by some (time-independent) vector field \mathbf{x}_0 . Often, \mathbf{x}_0 is chosen as the position of the center of mass of the fluid particle at some initial time t_0 . It is chosen in this particular way so that possible changes in the shape of the particle over time can be taken into account $\boxed{17}$. In the Lagrange description, the flow is described by a function,

$$\mathbf{X}(\mathbf{x}_0, t), \ \mathbf{X}, \mathbf{x}_0 \in \mathbb{R}^n, \ t \ge 0$$
 (2.11)

giving the position of the particle as a function of \mathbf{x}_0 and time t. The two descriptions are connected by the relation [17],

$$\mathbf{u}\left(\mathbf{X}(\mathbf{x}_{0},t),t\right) = \frac{\partial \mathbf{X}}{\partial t}\left(\mathbf{x}_{0},t\right) \tag{2.12}$$

because both terms describe the velocity of the particle, denoted \mathbf{x}_0 , at time t.

The Lagrange and Euler descriptions of the flow field are associated with the Stokes derivative (also called the material derivative) [17]. Suppose that one studies a flow field \mathbf{q} , and is also given a general field $\mathbf{F}(\mathbf{x},t)$. The interest lies in the total rate of change of \mathbf{F} undergone by a particular fluid particle. This can be calculated as,

$$\frac{\mathrm{D}\mathbf{F}}{\mathrm{D}t} = \frac{\partial \mathbf{F}}{\partial t} + \underbrace{(\mathbf{u} \cdot \nabla) \mathbf{F}}_{\text{translational rate of change}} \tag{2.13}$$
total rate of change | Lagrange derivative | Euler derivative |

where ∇ stands for the gradient operator with respect to \mathbf{x} , and the operator $\mathbf{u} \cdot \nabla$ must be applied to each component of \mathbf{F} . Then (2.13) tells us that the

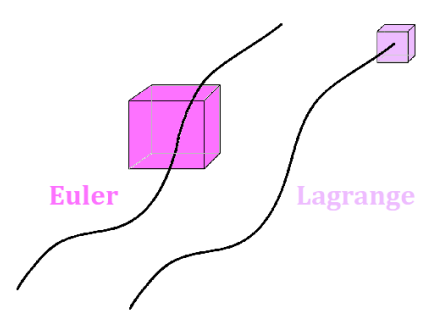


Figure 2.7: Graphic representation of the Euler and Lagrange descriptions.

total rate of change of \mathbf{F} as the fluid particles move through a flow field under the Euler description of \mathbf{u} is equal to the sum of the local rate of change and the translational rate of change of \mathbf{F} . Mathematically, this is an implication of chain differentiating $\mathbf{F}(\mathbf{X}(\mathbf{x}_0,t),t)$ with respect to t.

As an example, imagine a relatively light particle floating and drifting along a flowing river that undergoes changes in its temperature. The temperature of the water locally can increase because one part of the river is sunny and another is in the shade, or the water as a whole may warm up as the day progresses. Changes resulting from the motion of the particle (which is caused by the motion of the fluid) are called advective changes.

To summarize, the main difference between the two descriptions is that in the Lagrange description the coordinates of the fluid particle depend on time, being dependent variables, whereas in the Euler description they are time-independent variables, since the velocity is a function of time and position. The Lagrangian view is particularly useful when the laws of fluid motion are derived from Newton's laws. However, once derived, these laws are more conveniently interpreted from the Euler point of view. The conservation laws, expressed per unit mass, have a Lagrangian form, which together with the conservation of mass produces Euler conservation. In contrast, when fluid particles can exchange a quantity (such as energy or momentum), only conservation laws in Euler form exist [18].

Geometrical representation of flow

Streamlines (or flow lines), streaklines, and pathlines are predicted for field lines in a fluid flow. They differ only when the flow varies with time, that is, when the flow is not constant [17]. Considering a vector velocity field in a three-dimensional space in the context of continuum mechanics, the following hold.

• The flow lines (streamlines) are a family of curves whose tangent vectors constitute the velocity field of the flow. They indicate the direction in which a massless fluid element will move at any given time.

- The streaklines are the geometric locations of the points of all fluid particles that have continuously passed through a given spatial point in the past. A dye stably injected into the fluid at a fixed point extends along a bar line.
- The path lines are the trajectories followed by individual fluid particles. They can be thought of as a «record» of the path of a flowing fluid element during a certain period of time. The direction of the path will be determined by the flow lines of the fluid at any given time.
- Timelines are the lines formed by a set of fluid particles, marked at a previous time instant, creating a line or curve that shifts in time as the particles move.

By definition, different flow lines, at the same instant in a flow, do not intersect, since a fluid particle cannot have two different velocities at the same point. However, path lines are allowed to intersect themselves or other path lines (except for the starting and end points of path lines, which must be distinct). Bar lines may also intersect themselves, as well as other bar lines.

Flow lines and timelines provide a snapshot of certain characteristics of the flow field, whereas bar lines and path lines depend on the full time history of the flow. However, often, sequences of timelines and streaklines, at different times, presented either in a single image or with a video stream, can be used to provide information about the flow and its evolution.

In the case where a line, curve or closed curve is used as a starting point for a continuous set of flow lines, the result is a stream surface. In the case of a closed curve in a steady flow, the fluid within a flow surface must remain there forever because the flow lines are tangent to the flow velocity. A gradient function whose isostatic curves define the flow lines is called a flow function or stream function.

Let's now look at the mathematical interpretation of the above basic concepts of a flow. Flow lines are defined by the relation [19],

$$\frac{d\vec{x}_S}{ds} \times \vec{q}(\vec{x}_S) = 0 \tag{2.14}$$

where \times denotes the cross product and $\vec{x}_S(s)$ is the parametric representation of a flow line at a time. If the velocity components are written as, $\vec{q} = (u, v, w)$, and those of the flow line as $\vec{x}_S = (x_S, y_S, z_S)$, we conclude that,

$$\frac{dx_S}{u} = \frac{dy_S}{v} = \frac{dz_S}{w} \tag{2.15}$$

which shows that the curves are parallel to the velocity vector. Here s is a variable that parametrizes the curve $s \mapsto \vec{x}_S(s)$.

The pathlines are defined via the relation [19],

$$\begin{cases} \frac{d\vec{x}_P}{dt}(t) = \vec{u}_P(\vec{x}_P(t), t) \\ \vec{x}_P(t_0) = \vec{x}_{P0} \end{cases}$$
 (2.16)

The subscript P indicates that we are following the motion of a fluid particle. Note that at the point \vec{x}_P the curve is parallel to the flow velocity vector \vec{u} , where the velocity vector is estimated at the position of the particle \vec{x}_P at the given time t.

Additionally, the streaklines can be expressed via the relation [19],

$$\begin{cases}
\frac{d\vec{x}_{str}}{dt} = \vec{u}_P(\vec{x}_{str}, t) \\
\vec{x}_{str}(t = \tau_P) = \vec{x}_{P0}
\end{cases}$$
(2.17)

where $\vec{u}_P(\vec{x},t)$ is the velocity of a particle P at the position \vec{x} , at time t. The parameter τ_P , parametrizes the streakline $\vec{x}_{str}(t,\tau_P)$ with $t_0 \leq \tau_P \leq t$, where t is a time of interest.

The stream function of a two-dimensional flow $\mathbf{q} := (u, v)$ is defined as the twice continuously differentiable function $\Psi : \mathbb{R}^2 \to \mathbb{R}$, with Π ,

$$\left\{ u = \Psi_y, \ v = -\Psi_x \right. \tag{2.18}$$

such that the so-called flow continuity equation is satisfied, which corresponds to the conservation of fluid mass during flow,

$$\nabla \cdot \mathbf{q} = u_x + v_y = \Psi_{yx} - \Psi_{xy}$$
$$= 0$$

The stream function is also defined in special cases of three-dimensional flows, e.g. axisymmetric flows.

In a steady flow (where the vector velocity field does not vary with time), the flow lines, path lines, and bar lines coincide. This is not surprising, and is due to the fact that when a particle on a streamline reaches a point, a_0 , further along that line the equations governing the flow will send it in a particular direction \vec{x} . As the equations governing the flow remain the same, when another particle reaches a_0 it will also go in the direction \vec{x} . If the flow is not constant then when the next particle reaches a_0 the flow will have changed and the particle will go in a different direction. This observation is particularly useful, since it is usually very difficult to examine the flow lines in an experiment. However, if the flow is constant, one can, through the bar lines, describe the pattern of the flow lines.

In fluid dynamics, knowledge of the streamlines is of paramount importance. The curvature of a flow line is related to the vertical pressure gradient in the flow line. The centre of curvature of a streamline occurs in the direction of decreasing radial pressure. The magnitude of the radial pressure gradient can be calculated directly from fluid density, streamline curvature and local velocity.

Finally, it is worth mentioning that the streamlines depend on the reference framework. This means that the flow lines observed in one inertial reference frame are different from those observed in another inertial reference frame. For example, the flow lines in the air around an aircraft wing are defined differently for passengers in the aircraft than for an observer on the ground. In the aircraft example, the observer on the ground will observe non-permanent flow, while the observers on the aircraft will observe permanent flow, with constant flow lines. In general, in fluid dynamics we seek a reference frame in which the flow is steady, so that experimental methods of generating bar lines can be used to determine the flow lines.

The Navier-Stokes equations

Blood flow in a pulsating artery is governed by the principles of fluid dynamics, specifically described by the Navier-Stokes (NS) equations. For a transient, three-dimensional, laminar, and incompressible flow, these equations, in cartesian coordinates, are expressed as follows \mathfrak{Q} :

Continuity equation

$$\nabla_{\mathbf{x}} \cdot \mathbf{q} = 0 \tag{2.19}$$

Momentum equation

$$\underbrace{\mathbf{q}_t + (\mathbf{q} \cdot \nabla_{\mathbf{x}})\mathbf{q}}_{\text{inertia terms}} = \underbrace{-\frac{\nabla_{\mathbf{x}}p}{\rho} + \nu\Delta_{\mathbf{x}}\mathbf{q} + \mathbf{F}}_{\text{viscous terms}}$$
(2.20)

with $\mathbf{q} = (u, v, w)$ being the velocity field and $\mathbf{x} = (x, y, z)$ the position vector. Additionally, p denotes the pressure driving the flow, ρ the fluid density, and ν the kinematic viscosity of the fluid. Finally $\nabla_{\mathbf{x}}$ stands for the cartesian gradient vector $\left(\frac{\partial}{\partial x}, \frac{\partial}{\partial y}, \frac{\partial}{\partial z}\right)$. Regarding the physical meaning of the terms encountered above, one has:

- \mathbf{q}_t : local acceleration
- $(\mathbf{q} \cdot \nabla_{\mathbf{x}})\mathbf{q}$: nonlinear translational acceleration
- $-\frac{\nabla_{\mathbf{x}}p}{\rho}$: internal forcing (internal source)
- $\nu \Delta_{\mathbf{x}} \mathbf{q}$: diffusion
- **F** : external forcing term

The first equation of the NS system is the continuity equation (mass conservation) with the second being the momentum equation, in apparent analogy with Newton's 2nd law. The NS system is of order 2 in space and of order 1 in time, nonlinear and generally inhomogeneous. It is furthermore coupled, since none of the equations can be solved independently of the others.

The goal now is to derive a closed, conservative form of the NS equations, which is convenient enough for their numerical treatment [9]. One starts with

the left-hand side of the x- momentum equation, getting:

$$u_t + uu_x + vu_y + wu_z = u_t + uu_x + vu_y + wu_z + u \underbrace{(u_x + v_y + w_z)}_{=0 \text{ (continuity equation)}}$$
$$= u_t + (u^2)_x + (uv)_y + (uw)_z$$
(2.21)

Regarding the right-hand side:

$$-\frac{p_x}{\rho} + \nu(u_{xx} + u_{yy} + u_{zz}) = \left(-\frac{p}{\rho}\right)_x + \left[(\nu u)_{xx} + (\nu u)_{yy} + (\nu u)_{zz}\right]$$
(2.22)

Therefore, by combining (2.21) and (2.22), the x- momentum equation is written as:

$$u_t + (u^2)_x + (uv)_y + (uw)_z = \left(-\frac{p}{\rho}\right)_x + \left[(\nu u)_{xx} + (\nu u)_{yy} + (\nu u)_{zz}\right]$$
 (2.23)

The y- and z- momentum equations are expressed in a similar manner.

For convenience, consider a negligible external force along with a characteristic length L and velocity U, so that the new, dimensionless, variables are expressed via the transformation:

$$\begin{cases} \mathbf{x}^* := \frac{\mathbf{x}}{L}, \ \nabla^* := L \nabla_{\mathbf{x}}, \\ \mathbf{q}^* := \frac{\mathbf{q}}{U}, \\ t^* := \frac{t}{\frac{L}{U}} \end{cases}$$
 (2.24)

Regarding the pressure p there is no natural choice and one may choose among:

$$\begin{cases} p^* = \frac{p}{\rho U^2} \text{ (high speed flows),} \\ \\ p^* = \frac{pL}{\mu U} \text{ (creeping flows)} \end{cases}$$
 (2.25)

Thus, substituting (2.24) and (2.25) into the NS system, for high-speed flows, yields:

$$\begin{cases}
\nabla^* \cdot \mathbf{q}^* = 0, \\
\frac{\partial \mathbf{q}^*}{\partial t^*} + (\mathbf{q}^* \cdot \nabla^*) \mathbf{q}^* = -\nabla^* p^* + \frac{\nu}{LU} \nabla^{*2} \mathbf{q}^*
\end{cases}$$
(2.26)

while for slow, viscous-dominated flows,

$$\begin{cases}
\nabla^* \cdot \mathbf{q}^* = 0, \\
\frac{LU}{\nu} \left(\frac{\partial \mathbf{q}^*}{\partial t^*} + (\mathbf{q}^* \cdot \nabla^*) \mathbf{q}^* \right) = -\nabla^* p^* + \nabla^{*2} \mathbf{q}^*
\end{cases}$$
(2.27)

The dimensionless number,

$$Re := \frac{LU}{\nu} \tag{2.28}$$

is known as the Reynolds number and makes an important contribution to the prediction of the flow in different states, expressing the ratio between the inertia and viscous forces. At low Re, the flow tends to be laminar, while at high Re it tends to be turbulent.

- In the case of high Re, Re $\to \infty$, the momentum equations (2.26) are reduced to the Euler equations, with the inertia forces dominating, the term $\frac{1}{Re}\nabla^{*2}\mathbf{q}^*$ being negligible, and the fluid behaves as an ideal fluid.
- In contrast, in the case of low Re, Re → 0⁺, the momentum equations (2.27) describe creeping (or slow) Stokes flows, where viscous forces predominate on the right-hand side of (2.27). It is worth pointing out that these equations are linear.

The flows under study are governed by the following dimensionless numbers:

• Re :
$$\frac{2\rho uR}{\mu} \sim \frac{\text{inertial forces}}{\text{viscous forces}}$$

where R denotes the arterial radius.

with R_c corresponding to the radius of curvature of the artery. The Dean number De is indicative of secondary flow in curved pipes. When a fluid moves from a straight pipe to a curved section, centrifugal forces develop as a result of the curvature, creating an asymmetric flow. This shifts the maximum velocity from the center towards the concave outer wall, altering the velocity profile. The curvature induces a pressure gradient that increases pressure and decreases velocity near the convex wall, while the opposite occurs near the concave wall. This results in secondary motion: the fluid at the center moves outwards, while the fluid near the walls moves inward.

• Wo:
$$R\sqrt{\frac{2\pi\rho}{\mu T}}$$

with T being the period of the cardiac cycle. The Womersley number Wo is used to predict deviations from the parabolic flow profile, as well as flow reversals. More details on Wo will be discussed later.

The vorticity equation

As seen above, the Navier-Stokes equations form a coupled system in terms of the velocity field and flow pressure. However, the pressure terms can be eliminated from the equations. For this purpose, the vorticity of both members of the momentum equation of (2.20), is considered to derive an equation for the vorticity $\omega = \nabla_{\mathbf{x}} \times \mathbf{q}$. The driving idea here is that the vorticity of a gradient, such as pressure, vanishes, and therefore pressure, or any other conservative quantity, is eliminated from the equation. Under this framework, one gets,

$$\nabla_{\mathbf{x}} \times [\mathbf{q}_{t} + (\mathbf{q} \cdot \nabla_{\mathbf{x}})\mathbf{q}] = \nabla_{\mathbf{x}} \times \left[-\frac{\nabla_{\mathbf{x}}p}{\rho} + \nu \Delta_{\mathbf{x}}\mathbf{q} + \mathbf{F} \right]$$

$$\Leftrightarrow (\nabla_{\mathbf{x}} \times \mathbf{q})_{t} + \nabla_{\mathbf{x}} \times [(\mathbf{q} \cdot \nabla_{\mathbf{x}})\mathbf{q}] = -\underbrace{\frac{\nabla_{\mathbf{x}} \times \nabla_{\mathbf{x}}p}{\rho}}_{=0} + \nu \nabla_{\mathbf{x}} \times \Delta_{\mathbf{x}}\mathbf{q} + \nabla_{\mathbf{x}} \times \mathbf{F}$$

$$\Leftrightarrow \omega_{t} + \nabla_{\mathbf{x}} \times [(\mathbf{q} \cdot \nabla_{\mathbf{x}})\mathbf{q}] = \nu \Delta_{\mathbf{x}}\omega + \nabla_{\mathbf{x}} \times \mathbf{F}$$

$$(2.29)$$

One may easily verify that $\nabla_{\mathbf{x}} \times [(\mathbf{q} \cdot \nabla_{\mathbf{x}})\mathbf{q}]$ satisfies,

$$\nabla_{\mathbf{x}} \times [(\mathbf{q} \cdot \nabla_{\mathbf{x}})\mathbf{q}] = \nabla_{\mathbf{x}} \times (\omega \times \mathbf{q}) \tag{2.30}$$

Therefore, from (2.29) and (2.30), it follows that,

$$\omega_t + \nabla_{\mathbf{x}} \times (\omega \times \mathbf{q}) = \nu \Delta_{\mathbf{x}} \omega + \nabla_{\mathbf{x}} \times \mathbf{F}$$
 (2.31)

Moreover, in the case where the external force field is conservative, e.g. it is the Earth's gravitational field \mathbf{g} , then (2.31) becomes,

$$\omega_t + \nabla_{\mathbf{x}} \times (\omega \times \mathbf{q}) = \nu \Delta_{\mathbf{x}} \omega \tag{2.32}$$

In the case of two-dimensional flow, introducing the stream function,

$$\begin{cases} u = \Psi_y, \ v = -\Psi_x \end{cases} \tag{2.33}$$

the continuity equation is automatically satisfied and (2.32) is reduced to,

$$(\Delta_{\mathbf{x}}\Psi)_t + \Psi_y(\Delta_{\mathbf{x}}\Psi)_x - \Psi_x(\Delta_{\mathbf{x}}\Psi)_y = \nu\Delta_{\mathbf{x}}(\Delta_{\mathbf{x}}\Psi)$$
(2.34)

The last equation, together with appropriate boundary conditions, describes the two-dimensional fluid flow, taking only the kinematic viscosity as a parameter. Note that the equation for the Stokes flow is obtained when the left-hand side of the above equation is assumed to be zero. In the case of three-dimensional and axisymmetric flow, the corresponding result can be derived using the Stokes stream function 17.

The GCC transform

One key point of the study is the ability to express the NS equations in any generalized curvilinear coordinate (GCC) system by substituting the particular form of the gradient vector, obtained by chain differentiation.

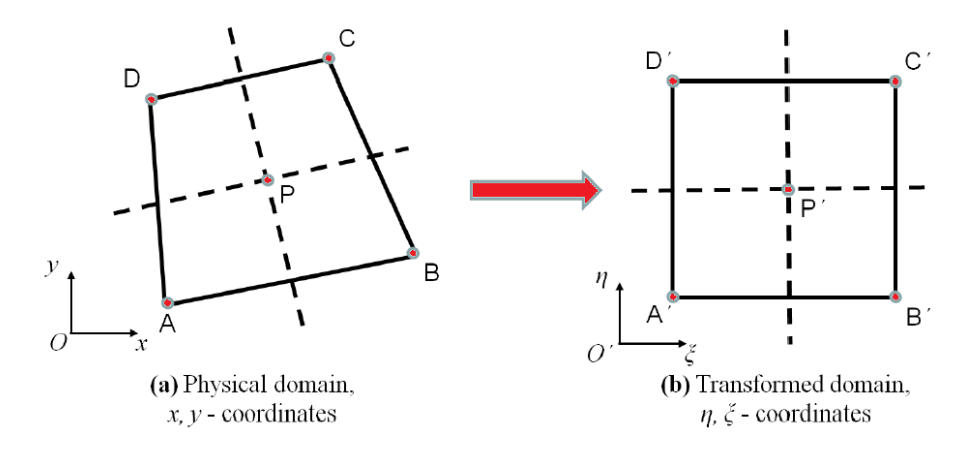


Figure 2.8: Graphical representation of the local transformation from a physical (GCC) to a transformed (orthogonal) domain.

In order to derive the governing fluid flow equations in generalized curvilinear coordinates, facilitating the study of fluid flow in complex domains, the chain rule is applied to the unknown variables:

$$u_x = \xi_x u_\xi + \eta_x u_\eta + \zeta_x u_\zeta,$$

$$v_y = \xi_y v_\xi + \eta_y v_\eta + \zeta_y v_\zeta,$$

$$w_z = \xi_z w_\xi + \eta_z w_\eta + \zeta_z w_\zeta$$
(2.35)

Equivalently one may write:

$$\begin{pmatrix} u_x & u_y & u_z \\ v_x & v_y & v_z \\ w_x & w_y & w_z \end{pmatrix} = \begin{pmatrix} u_{\xi} & u_{\eta} & u_{\zeta} \\ v_{\xi} & v_{\eta} & v_{\zeta} \\ w_{\xi} & w_{\eta} & w_{\zeta} \end{pmatrix} \underbrace{\begin{pmatrix} \xi_x & \xi_y & \xi_z \\ \eta_x & \eta_y & \eta_z \\ \zeta_x & \zeta_y & \zeta_z \end{pmatrix}}_{(2.36)}$$

Also note that:

$$J^{-1} = \begin{pmatrix} x_{\xi} & y_{\xi} & z_{\xi} \\ x_{\eta} & y_{\eta} & z_{\eta} \\ x_{\zeta} & y_{\zeta} & z_{\zeta} \end{pmatrix}$$
 (2.37)

One may further verify that:

$$\xi_{x} = \frac{y_{\eta}z_{\zeta} - y_{\zeta}z_{\eta}}{|J^{-1}|}, \quad \xi_{y} = \frac{z_{\zeta}x_{\eta} - z_{\eta}x_{\zeta}}{|J^{-1}|}, \quad \xi_{z} = \frac{x_{\eta}y_{\zeta} - x_{\zeta}y_{\eta}}{|J^{-1}|},
\eta_{x} = \frac{y_{\zeta}z_{\xi} - y_{\xi}z_{\zeta}}{|J^{-1}|}, \quad \eta_{y} = \frac{z_{\xi}x_{\zeta} - z_{\zeta}x_{\xi}}{|J^{-1}|}, \quad \eta_{z} = \frac{x_{\zeta}y_{\xi} - x_{\xi}y_{\zeta}}{|J^{-1}|},
\zeta_{x} = \frac{y_{\xi}z_{\eta} - y_{\eta}z_{\xi}}{|J^{-1}|}, \quad \zeta_{y} = \frac{z_{\eta}x_{\xi} - z_{\xi}x_{\eta}}{|J^{-1}|}, \quad \zeta_{z} = \frac{x_{\xi}y_{\eta} - x_{\eta}y_{\xi}}{|J^{-1}|}$$
(2.38)

Setting:

$$c_{1} := y_{\eta} z_{\zeta} - y_{\zeta} z_{\eta}, \quad c_{2} := z_{\zeta} x_{\eta} - z_{\eta} x_{\zeta}, \quad c_{3} := x_{\eta} y_{\zeta} - x_{\zeta} y_{\eta},$$

$$c_{4} := y_{\zeta} z_{\xi} - y_{\xi} z_{\zeta}, \quad c_{5} := z_{\xi} x_{\zeta} - z_{\zeta} x_{\xi}, \quad c_{6} := x_{\zeta} y_{\xi} - x_{\xi} y_{\zeta},$$

$$c_{7} := y_{\xi} z_{\eta} - y_{\eta} z_{\xi}, \quad c_{8} := z_{\eta} x_{\xi} - z_{\xi} x_{\eta}, \quad c_{9} := x_{\xi} y_{\eta} - x_{\eta} y_{\xi},$$

$$(2.39)$$

allows for a more compact form of the dimensionless NS equations in curvilinear coordinates:

Continuity equation (GCC)

$$\frac{\partial J^{-1}}{\partial t} + \frac{\partial U}{\partial \xi} + \frac{\partial V}{\partial \eta} + \frac{\partial W}{\partial \zeta} = 0 \tag{2.40}$$

x-momentum equation (GCC)

$$\begin{split} \frac{\partial (J^{-1}u)}{\partial t} &+ \frac{\partial (uU)}{\partial \xi} + \frac{\partial (uV)}{\partial \eta} + \frac{\partial (uW)}{\partial \zeta} \\ &= -\left(c_1 \frac{\partial p}{\partial \xi} + c_4 \frac{\partial p}{\partial \eta} + c_7 \frac{\partial p}{\partial \zeta}\right) \\ &+ \frac{1}{\mathrm{Re}} \frac{\partial}{\partial \xi} \left(\frac{1}{J^{-1}} \left(q_1 \frac{\partial u}{\partial \xi} + q_2 \frac{\partial u}{\partial \eta} + q_3 \frac{\partial u}{\partial \zeta}\right)\right) \\ &+ \frac{1}{\mathrm{Re}} \frac{\partial}{\partial \eta} \left(\frac{1}{J^{-1}} \left(q_2 \frac{\partial u}{\partial \xi} + q_4 \frac{\partial u}{\partial \eta} + q_5 \frac{\partial u}{\partial \zeta}\right)\right) \\ &+ \frac{1}{\mathrm{Re}} \frac{\partial}{\partial \zeta} \left(\frac{1}{J^{-1}} \left(q_3 \frac{\partial u}{\partial \xi} + q_5 \frac{\partial u}{\partial \eta} + q_6 \frac{\partial u}{\partial \zeta}\right)\right), \end{split}$$
(2.41)

y-momentum equation (GCC)

$$\frac{\partial(J^{-1}v)}{\partial t} + \frac{\partial(vU)}{\partial \xi} + \frac{\partial(vV)}{\partial \eta} + \frac{\partial(vW)}{\partial \zeta}$$

$$= -\left(c_2 \frac{\partial p}{\partial \xi} + c_5 \frac{\partial p}{\partial \eta} + c_8 \frac{\partial p}{\partial \zeta}\right)$$

$$+ \frac{1}{\text{Re}} \frac{\partial}{\partial \xi} \left(\frac{1}{J^{-1}} \left(q_1 \frac{\partial v}{\partial \xi} + q_2 \frac{\partial v}{\partial \eta} + q_3 \frac{\partial v}{\partial \zeta}\right)\right)$$

$$+ \frac{1}{\text{Re}} \frac{\partial}{\partial \eta} \left(\frac{1}{J^{-1}} \left(q_2 \frac{\partial v}{\partial \xi} + q_4 \frac{\partial v}{\partial \eta} + q_5 \frac{\partial v}{\partial \zeta}\right)\right)$$

$$+ \frac{1}{\text{Re}} \frac{\partial}{\partial \zeta} \left(\frac{1}{J^{-1}} \left(q_3 \frac{\partial v}{\partial \xi} + q_5 \frac{\partial v}{\partial \eta} + q_6 \frac{\partial v}{\partial \zeta}\right)\right),$$
(2.42)

z-momentum equation (GCC)

$$\frac{\partial(J^{-1}w)}{\partial t} + \frac{\partial(wU)}{\partial \xi} + \frac{\partial(wV)}{\partial \eta} + \frac{\partial(wW)}{\partial \zeta}$$

$$= -\left(c_3 \frac{\partial p}{\partial \xi} + c_6 \frac{\partial p}{\partial \eta} + c_9 \frac{\partial p}{\partial \zeta}\right)$$

$$+ \frac{1}{\text{Re}} \frac{\partial}{\partial \xi} \left(\frac{1}{J^{-1}} \left(q_1 \frac{\partial w}{\partial \xi} + q_2 \frac{\partial w}{\partial \eta} + q_3 \frac{\partial w}{\partial \zeta}\right)\right)$$

$$+ \frac{1}{\text{Re}} \frac{\partial}{\partial \eta} \left(\frac{1}{J^{-1}} \left(q_2 \frac{\partial w}{\partial \xi} + q_4 \frac{\partial w}{\partial \eta} + q_5 \frac{\partial w}{\partial \zeta}\right)\right)$$

$$+ \frac{1}{\text{Re}} \frac{\partial}{\partial \zeta} \left(\frac{1}{J^{-1}} \left(q_3 \frac{\partial w}{\partial \xi} + q_5 \frac{\partial w}{\partial \eta} + q_6 \frac{\partial w}{\partial \zeta}\right)\right),$$
(2.43)

where:

$$U := c_1 u + c_2 v + c_3 w,$$

$$V := c_4 u + c_5 v + c_6 w,$$

$$W := c_7 u + c_8 v + c_9 w,$$

$$J^{-1} := |J^{-1}|$$
(2.44)

Regarding q_i one has:

$$q_{1} := c_{1}^{2} + c_{2}^{2} + c_{3}^{2},$$

$$q_{2} := c_{1}c_{4} + c_{2}c_{5} + c_{3}c_{6},$$

$$q_{3} := c_{1}c_{7} + c_{2}c_{8} + c_{3}c_{9},$$

$$q_{4} := c_{4}^{2} + c_{5}^{2} + c_{6}^{2},$$

$$q_{5} := c_{4}c_{7} + c_{5}c_{8} + c_{6}c_{9},$$

$$q_{6} := c_{7}^{2} + c_{8}^{2} + c_{9}^{2}$$

$$(2.45)$$

The theory of generalized curvilinear coordinates provides a framework for transforming complex geometries into simpler ones and vice versa, facilitating analysis and computation.

The Finite Volume approach

The Finite Volume Method (FVM) solves PDEs by averaging conserved variable values across a volume, using a collocated approach with all state variables on grid points. The method achieves second-order accuracy for spatial derivatives and first-order accuracy for the time derivative, resulting in an unconditionally stable implicit scheme [20]. This approach minimizes the influence of convection for first-order accuracy, while diffusion terms retain second-order accuracy as flow velocity increases.

Due to the non-linearity of the NS equations, solving them analytically in three dimensions is challenging, yet various numerical methods have been developed for this purpose [21], [22], [23], [24]. The domain of interest is divided into finite volumes, with unknown variables evaluated at the faces of each

volume by integrating over the control volume. In three dimensions, the controls volume faces are denoted as w, e, s, n, b, and t, representing the faces in the two-dimensional area and the top and bottom in the z-axis [25]. An extended formalism on the FVM continuity and momentum equations can be found in [9, [24, [26], [27]]].

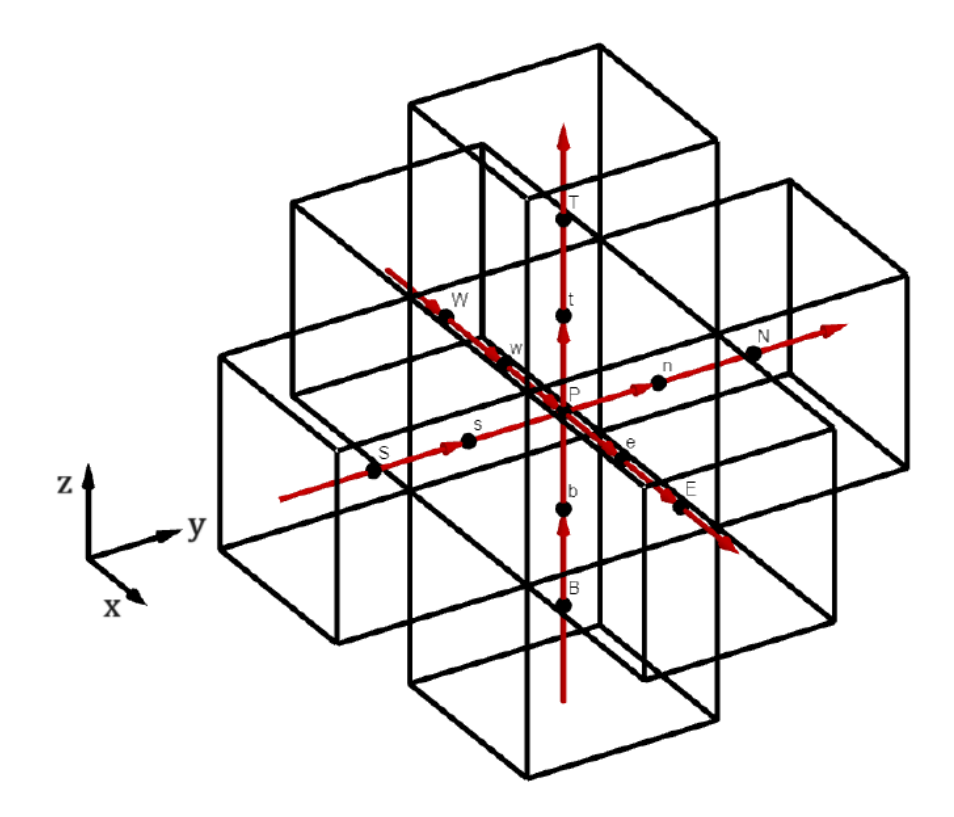


Figure 2.9: The centroid cube for discretization using FVM. The schematic appears identical to the two-dimensional case when viewed from above.

2.1.4 Exact flow models

No in-vivo experimental data are available for direct validation in this study. Therefore, to verify the accuracy of our computational approach, we performed benchmark simulations of fully developed laminar flows in canonical geometries. Specifically, velocity profiles and pressure drops obtained from simulations were compared against well-established theoretical solutions of the Navier–Stokes equations, including the Hagen–Poiseuille flow for steady pressure-driven flow in straight circular tubes, the Womersley flow describing pulsatile velocity profiles in oscillatory arterial flow, and the Dean flow characterizing secondary flow patterns

in curved tubes. These classical flow solutions provide essential reference cases that underpin the validation of CFD models in physiological flow simulations.

The Hagen-Poiseuille flow

In fluid dynamics, the Hagen-Poiseuille (HP) equation describes laminar flow through a pipe of length L and uniform (circular) cross-section of diameter D [28]. The equations governing HP flow are derived from the NS equations in three-dimensional cylindrical coordinates, (r, θ, x) , under the following assumptions:

- The flow is steady, i.e., $\frac{\partial ...}{\partial t} = 0$
- The radial and azimuthal velocity components are zero $(u_r = u_\theta = 0)$
- The flow is axisymmetric, that is, $\frac{\partial \dots}{\partial \theta} = 0$
- ullet Any external force field is negligible, i.e., ${f F}={f 0}$

The HP equation, under the above assumptions, reads:

$$\frac{1}{r}\frac{d}{dr}\left(r\frac{du}{dr}\right) = \frac{1}{\mu}\frac{dp}{dx}, \quad u := u_x \tag{2.46}$$

with boundary conditions $u(R) = \frac{du}{dr}(0) = 0$.

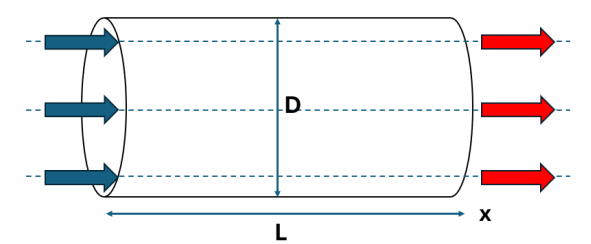


Figure 2.10: A straight cylindrical pipe filled with a fluid of density ρ and viscosity μ . The flow is laminar, axisymmetric and parallel to the x-axis.

In the above equation, the left term is a function of r, while the right term is a function of x, which means that both terms should equal the same constant. The valuation of this constant is straightforward. Given the length L of the pipe, denoting as Δp the pressure difference between the two ends of the pipe (high pressure minus low pressure), then the constant will be given as:

$$-\frac{dp}{dx} = \frac{\Delta p}{L} = G \tag{2.47}$$

defined such that G is positive. The general solution of (2.46) will be given as:

$$u(r) = -\frac{Gr^2}{4\mu} + C_1 \ln r + C_2 \tag{2.48}$$

which, due to the imposed boundary conditions, becomes:

$$u(r) = \frac{G}{4\mu} \left(R^2 - r^2 \right) \tag{2.49}$$

Considering the dimensionless distance, $y := \frac{r}{R} \in [0, 1]$, (2.49) is transformed to:

$$u(y) = \frac{GR^2}{4\mu} \left(1 - y^2 \right) \tag{2.50}$$

One can easily notice that u(r) exhibits a maximum at r=0, with the maximum velocity, U_{max} , given as $U_{max} = \frac{GR^2}{4\mu}$. The average velocity can be obtained by integration on the cross-section of the pipe:

$$\overline{u} = \frac{1}{\pi R^2} \int_0^R 2\pi r u dr = \frac{1}{2} U_{max}$$
 (2.51)

The easily measurable quantity in the experiments is the volumetric flow rate $Q = \pi R^2 \overline{u}$. The rearrangement of this equation gives the Hagen-Poiseuille relation for the pressure drop in the pipe:

$$\Delta p = \frac{8\mu LQ}{\pi R^4} \tag{2.52}$$

Furthermore, (2.52) was obtained under the assumption of laminar flow of the fluid in the pipe. This means that the Reynolds number of the flow, $\mathrm{Re_D} = \frac{\overline{u}D\rho}{\mu}$, is kept low and less than the critical Reynolds number, $\mathrm{Re_c}$. Experimentally, in the case where the fluid is water, the critical number Reynolds is approximately equal to 2300 [29]. For $\mathrm{Re} > \mathrm{Re_c}$ the flow ceases to be laminar and becomes turbulent [29].

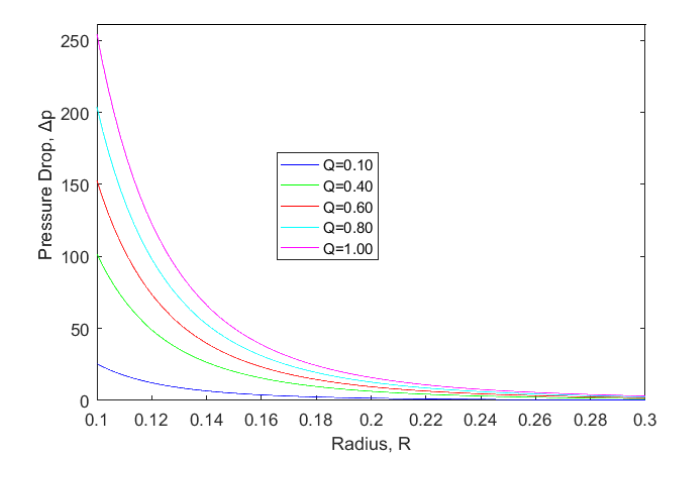


Figure 2.11: $\Delta p(r)$ for different Q, for L=1 and $\mu=0.01$.

The Womersley pulsatile flow

In fluid dynamics, the Womersley pulsatile flow is a flow governed by periodic variations. Womersley firstly derived such flow profiles in his study of blood flow in the cardiovascular system. Pulse flow profiles are given by the Womersley equation, which describes laminar and unsteady flow in a rectilinear cylindrical pipe of length L and radius R, containing a fluid of density ρ , dynamic viscosity μ and kinematic viscosity $\nu = \frac{\mu}{\rho}$. The derivation of the exact solution of the velocity profile requires the following assumptions [28] 30.

- The fluid is homogeneous, incompressible and Newtonian
- The pipe wall is rigid and cylindrical
- The flow is axisymmetric and parallel to the axis of the pipe
- Axisymmetry and the no-slip condition apply at the centre of the pipe and at its wall, respectively
- The pressure gradient is periodic in time
- Gravity does not significantly affect the flow

Based on the above assumptions, the NS equations simplify as:

$$\frac{\partial u}{\partial t} = -\frac{1}{\rho} \frac{\partial p}{\partial x} + \nu \left(\frac{\partial^2 u}{\partial r^2} + \frac{1}{r} \frac{\partial u}{\partial r} \right)$$
 (2.53)

Considering the dimensionless, normalized variables:

$$y = \frac{r}{R}, \ z = \frac{x}{R}, \ \tau = \omega t, \ u = \frac{v}{W}$$
 (2.54)

(2.53) transforms into:

$$\frac{R^2 \omega}{\nu} \frac{\partial v}{\partial \tau} = -\frac{R}{\rho \nu W} \frac{\partial p}{\partial z} + \frac{\partial^2 v}{\partial y^2} + \frac{1}{y} \frac{\partial v}{\partial y}$$
(2.55)

From (2.55) one obtains a natural normalization of pressure:

$$p^* = \frac{Rp}{\rho\nu W} = \frac{Rp}{\mu W} \tag{2.56}$$

from which, combined with (2.55), follows:

$$Wo^{2} \frac{\partial v}{\partial \tau} = -\frac{\partial p^{*}}{\partial z} + \frac{\partial^{2} v}{\partial u^{2}} + \frac{1}{u} \frac{\partial v}{\partial y}$$
 (2.57)

which is the dimensionless, normalized Womersley equation. The dimensionless quantity,

$$Wo := R\sqrt{\frac{\omega}{\nu}}, \tag{2.58}$$

expresses the frequency of the pulse flow in relation to its viscous effects, and is defined as the Womersley number, symbolically Wo.

The flows where Wo $\gg 1$ are usually characterized as dominated by inertia terms, since the viscous forces are negligible compared to the other terms in the equation (2.57) and the pressure gradient is used exclusively for the acceleration of the fluid particle. Such a situation usually occurs in large-diameter vessels (aorta), in high-frequency flows.

In the case where the flow has Wo $\ll 1$ (small-diameter and/or low-frequency vessels), (2.57) is reduced to the normalized HP equation, with the flow dominated by friction terms. Such a situation occurs in capillaries.

As (2.57) is linear, superposition of solutions for various harmonics is allowed. To proceed further, one may assume that the pressure gradient is oscillatory and represent it by:

$$\frac{\partial p^*}{\partial z}(\tau) = \frac{\partial}{\partial z}e^i \tag{2.59}$$

This consideration is justified by the fact that the heartbeat varies periodically in time, and can therefore be expressed as a series of terms of the above form. Because of the harmonic form of the pressure gradient, it is further assumed that velocity can be represented as:

$$v(y,\tau) = w(y)e^{i\tau} \tag{2.60}$$

The transformation (2.60) converts (2.57) to:

$$y^{2}\frac{d^{2}w}{dy^{2}} + y\frac{dw}{dy} + \left(i^{3/2}\operatorname{Woy}\right)^{2}w = \frac{\partial\hat{p}}{\partial z}y^{2}$$
(2.61)

The boundary conditions of the problem are $w(1) = \frac{dw}{dy}(0) = 0$. By means of the transformation:

$$s = i^{3/2} \text{Wo} y \tag{2.62}$$

(2.61) is reduced to the inhomogeneous Bessel equation of order zero:

$$s^2 \frac{d^2 w}{ds^2} + s \frac{dw}{ds} + s^2 w = \frac{i}{\text{Wo}^2} \frac{\partial \hat{p}}{\partial z} s^2$$
 (2.63)

with boundary conditions $w(i^{3/2}\text{Wo}) = \frac{dw}{ds}(0) = 0$. Note that:

$$w_p(s) = \frac{i}{\text{Wo}^2} \frac{\partial \hat{p}}{\partial z} \tag{2.64}$$

is a partial solution of (2.63). Equation (2.63) is linear, so its general solution is obtained by summing the general solution of the homogeneous (2.63) with \hat{w}_p . The homogeneous (2.63) is solved analytically, around $s_0 = 0$, via the Frobenius method, with its solution expressed through Bessel functions of first kind and zero order (31), as:

$$w_H(s) = C_1 J_0(s) + C_2 Y_0(s) \tag{2.65}$$

Thus, the general solution of (2.63), is obtained:

$$w(s) = w_p(s) + w_H(s) (2.66)$$

Respecting the boundary conditions, one arrives at the solution:

$$w(s) = \frac{i}{Wo^{2}} \frac{\partial \hat{p}}{\partial z} \left(1 - \frac{J_{0}(s)}{J_{0}(i^{3/2}Wo)} \right)$$
 (2.67)

Reversing the aforementioned transformations to return to the original variables, it finally follows:

$$u(r,t) = \frac{i}{\rho\omega} \frac{\partial p}{\partial x} \left(1 - \frac{J_0(i^{3/2} \text{Wor}/R)}{J_0(i^{3/2} \text{Wo})} \right)$$
 (2.68)

Ultimately, since (2.63) is linear, the real solution for the velocity profile is obtained by taking the real part of the complex function of (2.68),

$$\Re\left\{\frac{i}{\rho\omega}\frac{\partial p}{\partial x}\left(1 - \frac{J_0(i^{3/2}\text{Wor}/R)}{J_0(i^{3/2}\text{Wo})}\right)\right\}$$
 (2.69)

To be convinced of the validity of this claim, it suffices to see that if L is a linear (differential) operator and $u = \Re u + i\Im u$ such that L[u] = 0, then,

$$0=L[u]=L[\Re u+i\Im u]=L[\Re u]+iL[\Im u]$$

so $L[\Re u] = L[\Im u] = 0$, i.e. the real and imaginary parts of the solution are also solutions.

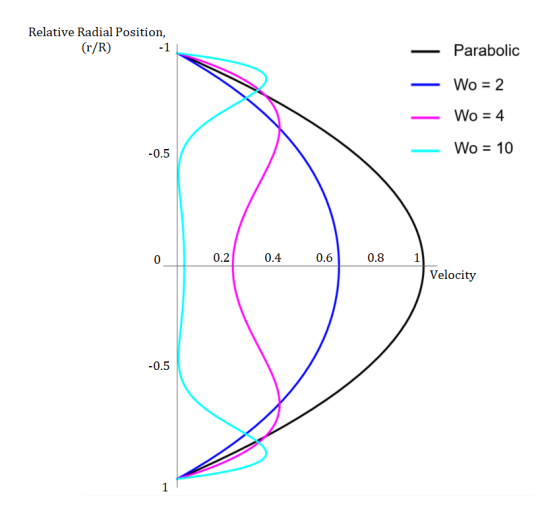


Figure 2.12: Velocity profiles for different values of Wo. The parabolic profile originates from the HP flow.

The Korteweg de Vries-Burgers model

This section discusses the Korteweg-de Vries-Burgers (KdVB) equation [32],

$$u_t + \gamma u u_x - \alpha u_{xx} + \beta u_{xxx} = 0, \quad u = u(x, t), \quad (x, t) \in \mathbb{R} \times (0, \infty), \quad (2.70)$$

serving as the simplest nonlinear and non-integrable wave model balancing nonlinearity, dissipation, and dispersion. Its derivation comes through considering the Womersley flow assumptions, along with a thin and viscoelastic tube [32, 33]. Focus shall be set on its applications to uterine hemodynamics, where the dicrotic notch stage is observed. The obtained analytical solutions are in qualitative agreement with the dicrotic notch stage.

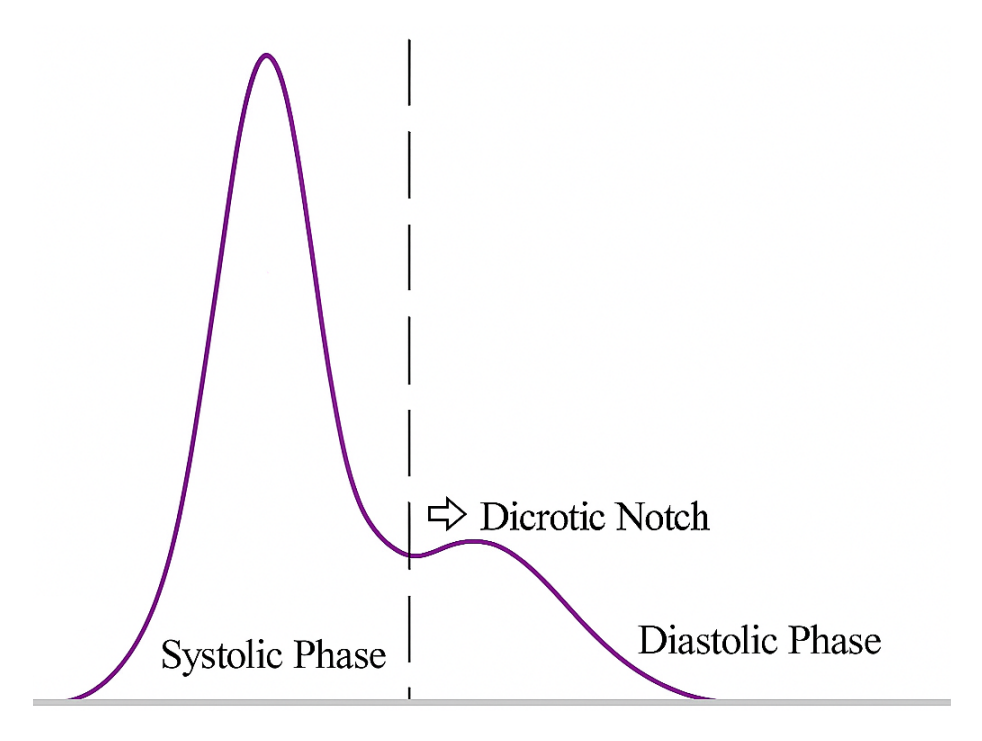


Figure 2.13: The dicrotic notch, between the phases of systolic and diastolic flow, in the formation of the uterine arterial pulse.

Exact, traveling wave, solutions of the n-dimensional KdVB and compound KdVB equations ($n \in \mathbb{N}$), derived through the hyperbolic tangent method, are derived and discussed in [32, 35, 36]. These solutions consist of both solitary and wavefront parts, a behavior also highlighted in the formational stages of the arterial pulse [32].

Secondary flow

When fluid flows through a straight pipe and encounters a curved section, centrifugal forces develop due to the change in direction. This results in an asymmetric flow profile, shifting the maximum velocity from the center to the outer, concave wall of the curve. The pressure increases near the convex wall, reducing velocity there, while the opposite occurs near the concave wall. This causes secondary flow, where fluid in the pipe's center moves outward, and fluid near the wall circulates back toward the inside of the bend [37].

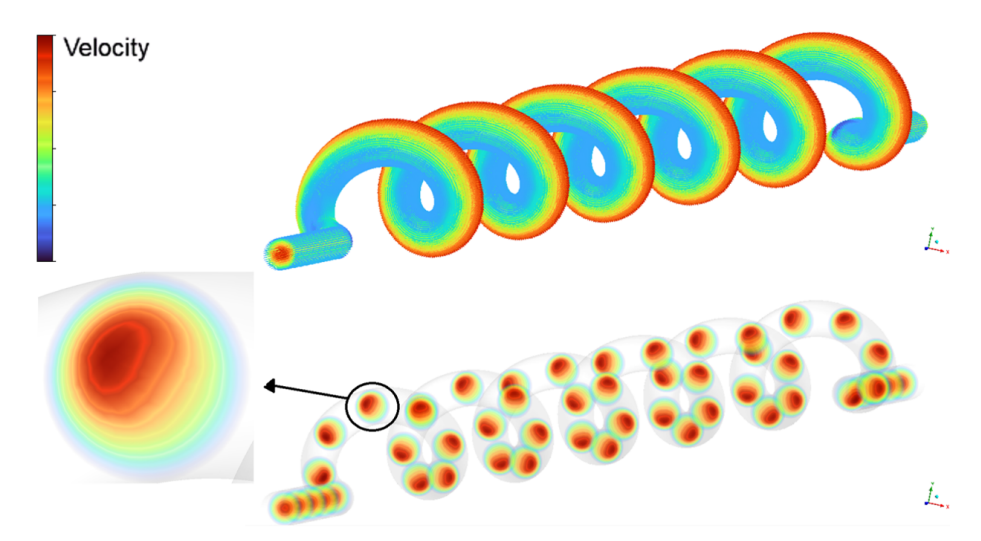


Figure 2.14: Velocity distribution and secondary flow patterns in the umbilical artery, obtained through our CFD analysis (more in the Results section). The top part illustrates the helical velocity profile, while the bottom one highlights vortex formation along the curvature. The inset on the left shows a cross-sectional view of the velocity distribution, revealing a characteristic secondary Dean flow pattern.

William Dean, after whom the Dean number De is named, was the first to develop a theoretical explanation for how fluids move through curved pipes under laminar flow conditions. He achieved this by applying a mathematical technique called perturbation analysis. This approach starts with the well-understood Poiseuille flow (the flow of a fluid through a straight pipe) and gradually adapts it to account for the effects of slight curvature in the pipe. Dean's work laid the foundation for understanding fluid dynamics in curved geometries.

Dean studied the so-called Dean equations, serving as an approximation to the NS equations [38], where flow in a slowly curved pipe is considered. Using cylindrical coordinates, (r, θ, z) , the pipe is modeled as,

$$D = \{(r, \theta, z) | (r - b)^2 + z^2 = a^2\}$$
(2.71)

with $b \gg a$. Notice that (2.71) refers to a portion of a torus. Solutions independent of θ are sought, driven by $\frac{\partial p}{\partial \theta}$. The velocity field (u_r, u_θ, u_z) satisfies the NS equations, in cylindrical coordinates, namely:

$$\begin{cases} \frac{1}{r} \frac{\partial}{\partial r} \left(r u_r \right) + \frac{\partial u_z}{\partial z} = 0, \\ \rho \left(\frac{D u_r}{D t} - \frac{u_\theta^2}{r} \right) = -\frac{\partial p}{\partial r} + \mu \left(\nabla^2 u_r - \frac{u_r}{r^2} \right), \\ \rho \left(\frac{D u_\theta}{D t} + \frac{u_\theta u_r}{r} \right) = \underbrace{-\frac{1}{r} \frac{\partial p}{\partial \theta}}_{=G} + \mu \left(\nabla^2 u_\theta - \frac{u_\theta}{r^2} \right), \end{cases}$$

$$\left(\frac{D u_z}{D t} = -\frac{\partial p}{\partial z} + \mu \nabla^2 u_z \right)$$

$$(2.72)$$

where:

$$\frac{D}{Dt} = \frac{\partial}{\partial t} + u_r \frac{\partial}{\partial r} + u_z \frac{\partial}{\partial z}.$$
 (2.73)

Dean sought for steady solutions of (2.72). Could a unidirectional solution work, as in the straight pipe case? Setting $u_r = u_z = 0$, (2.72) provides with:

$$\frac{\partial p}{\partial z} = 0, \quad \frac{\partial p}{\partial r} = \frac{u_{\theta}^2}{r} \Rightarrow \frac{\partial u_{\theta}}{\partial z} = 0$$
 (2.74)

Thus, such a solution is feasible only if u_{θ} remains constant on cylinders. This type of flow aligns with the no-slip condition exclusively for flows occurring between concentric cylinders. Consequently, any flow within a curved pipe cannot be unidirectional. For an almost straight pipe, it is reasonable to anticipate that the flow is nearly unidirectional. The radial and axial coordinates r and z vary over a scale a, and we assume $b \gg a$, leading to $r = b + ax^* \approx b$. Consequently:

$$\frac{\partial}{\partial r} \sim \frac{1}{a} \gg \frac{1}{r}$$

Furthermore, one may scale $z = az^*$ and let U_0 represent a typical scale of u_θ . The pressure is expected to scale as:

$$p \sim \rho U_0^2 \frac{a}{b}$$

The velocity components and their derivatives are scaled as:

$$u_r \frac{\partial u_r}{\partial r} \sim u_z \frac{\partial u_r}{\partial z} \sim \frac{u_\theta^2}{r}$$

This implies:

$$u_r \sim u_z \sim U_0 \left(\frac{a}{b}\right)^{1/2}$$

Therefore:

$$u_{\theta} = U_0 u_{\theta}^*, \quad u_{r,z} = U_0 \left(\frac{a}{b}\right)^{1/2} u_{x,z}^*, \quad p = \rho U_0^2 \left(\frac{a}{b}\right) p^*$$

Further requiring that:

$$\frac{Ga^2}{\mu U_0} = 1 \quad \text{and} \quad \text{De} = \frac{\rho U_0 a}{\mu} \left(\frac{a}{b}\right)^{1/2} \tag{2.75}$$

and neglecting terms of order $(\frac{a}{b})$, converts (2.72) into:

$$\begin{cases} \frac{\partial u_x}{\partial x} + \frac{\partial u_z}{\partial z} = 0, \\ \operatorname{De}\left(\frac{Du_x}{Dt} - u_\theta^2\right) = -\operatorname{De}\frac{\partial p}{\partial x} + \nabla^2 u_x, \\ \operatorname{De}\frac{Du_\theta}{Dt} = 1 + \nabla^2 u_\theta, \\ \operatorname{De}\frac{Du_z}{Dt} = -\operatorname{De}\frac{\partial p}{\partial z} + \nabla^2 u_z \end{cases}$$

$$(2.76)$$

These equations are, in essence, the two-dimensional Navier-Stokes equations, with a body force u_{θ}^2 directed toward the inside of the bend. In Cartesian coordinates (x, y, z), the velocity field is expressed as $\mathbf{q} = (u, v, w)$. To simplify the analysis, one may introduce a stream function $\psi(x, z)$, where:

$$u \equiv u_x = \frac{\partial \psi}{\partial z}, \quad w \equiv u_z = -\frac{\partial \psi}{\partial x}, \quad v(x,z) = u_\theta$$

Then (2.76) reduce to:

$$\begin{cases}
\operatorname{De}(\psi_z v_x - \psi_x v_z) = 1 + \nabla^2 v, \\
\operatorname{De}(\psi_z \Omega_x - \psi_x \Omega_z) = \nabla^2 \Omega - 2\operatorname{De} v v_z
\end{cases}$$
(2.77)

where $\Omega := -\nabla^2 \psi$ is the downpipe vorticity. These equations are solved for v(x,z) and $\psi(x,z)$ under the no-slip boundary conditions:

$$\nabla \psi = 0, \quad v = 0 \quad \text{on the pipe boundary}$$
 (2.78)

The problem involves a single parameter, De, known as the Dean number, which is defined in (2.75). This parameter represents a Reynolds number modified by the pipe curvature, $(a/b)^2$. For weak curvature effects (small De), the Dean equations can be solved using a series expansion in De. The first correction to the leading-order axial Poiseuille flow consists of a pair of vortices in the cross-section. These vortices transport fluid from the inside to the outside of the bend across the center and return it along the edges. This solution remains stable up to a critical Dean number, De ≈ 956 [39]. For larger De, multiple solutions exist, many of which are unstable.

2.1.5 Simulations properties

The present section discusses the flow setups of the uterine and umbilical blood flows. The geometries used are based on medical imaging of those vessels, obtained by ultrasound. As already mentioned, transient three-dimensional flows are considered, combining ultrasound data with an advanced CFD approach.

Focus is placed on the second trimester (21st and 22nd weeks) and the third trimester (30th and 31st weeks) of pregnancy. The results obtained from the statistical analysis suggest considering two simulations for the umbilical artery (one for the second trimester and one for the third trimester) and one simulation for the uterine artery (for the second trimester).

For the simulation of umbilical arterial flow corresponding to the second trimester, the maximum systolic velocity (PSV) was set to the average of the mean values PSV recorded in the 21st and 22nd weeks of gestation. The same approach was applied to the end diastolic velocity (EDV). Similarly, this method was used to determine the values in the third trimester. The modeling geometries are shown in Figure 2.15. As previously stated, we have validated our results by simulating a fully developed laminar flow in a circular tube and comparing the velocity profiles and pressure drops with theoretical solutions. The results show very good agreement, which supports the accuracy of our computational approach and numerical implementation.

[B] Real geometries

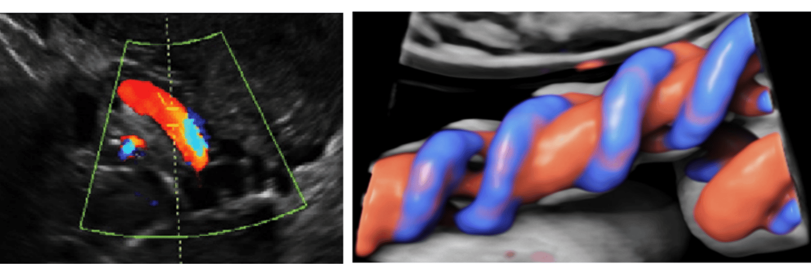


Figure 2.15: The geometries representing the uterine and umbilical arteries (**A**) were modeled based on real anatomical structures observed in Doppler ultrasound images (**B**) (GE Healthcare). A cylindrical pipe geometry was selected for the uterine artery, while a helical pipe geometry was chosen for the umbilical artery.

Uterine artery

The uterine artery is mathematically modeled as a straight cylindrical pipe, of length L=100 mm and radius R=2 mm. Flow is considered laminar, incompressible, with $\rho=1056$ kg/m³, and non-Newtonian, described by the Carreau model $\boxed{40}$, $\boxed{41}$, where

$$\mu(\dot{\gamma}) = \mu_{\infty} + (\mu_0 - \mu_{\infty}) \left[1 + (\lambda \dot{\gamma})^2 \right]^{\frac{n-1}{2}},$$
 (2.79)

with $\mu(\dot{\gamma})$ accounting for viscosity at shear rate $\dot{\gamma}$, μ_0 and μ_{∞} representing zero-shear viscosity and infinite-shear viscosity, λ standing for the relaxation time constant and n denoting the power-law index. At low shear rates ($\dot{\gamma} \to 0$), blood behaves like a Newtonian fluid with viscosity μ_0 . At high shear rates ($\dot{\gamma} \to \infty$), viscosity approaches μ_{∞} , following a power-law trend. The term

$$\left[1+(\lambda\dot{\gamma})^2\right]^{\frac{n-1}{2}},$$

captures the transition between these states, accounting for shear-thinning. The values chosen were $\mu_0 = 0.056$ kg/(ms), $\mu_\infty = 0.0035$ kg/(ms), $\lambda = 3.313$ s and n = 0.3568. A velocity periodic waveform,

$$u(r,t) = \underbrace{PSV}_{\text{peak systolic velocity}} \times \left[\underbrace{1 - \left(\frac{r}{R}\right)^{2}}_{\text{parabolic profile}}\right] \times \underbrace{g(t)}_{\text{periodic time dependence}}, \quad (2.80)$$

extracted by interpolating on the ultrasound data and applying Fourier analysis (10 terms), is used as the inlet boundary condition. The period of the pulse is set to $\frac{60}{80}$ s, corresponding to Wo \simeq 3. The no-slip boundary condition is considered on the arterial wall and a pressure outlet of 70 mmHg is set on its exit. It is worth noting that the exact value can vary based on individual physiology, yet pressures in this range support normal blood flow to the placenta and fetus. The arterial wall is modeled as rigid and stationary, focusing primarily on hemodynamics without accounting for wall motion.

To achieve numerical convergence and reduce computational resources and computing time, different mesh designs are utilized. The objective variables used to assess convergence were the mass average velocity and mass average absolute pressure within the vessels. These parameters were selected because they represent key hemodynamic quantities related to flow rate and pressure distribution, directly impacting the study's physiological interpretations. Mesh refinement was performed iteratively until these variables changed by less than 1% between successive refinements. The chosen computational mesh consists of approximately 2×10^5 hexahedral elements and 2.2×10^5 nodes. The residual RMS error values for the mass and momentum components over four cardiac cycles ranged between 10^{-4} and 10^{-5} . ANSYS Fluent (2025 R1 Academic, 16.1 Academic) was used to study the uterine and umbilical arterial flows. Figure 2.16 illustrates the process followed to obtain the inlet waveforms from the ultrasound data. In Figure 2.17 a schematic outline of the uterine arterial flow setup is depicted, with the flow parameters determined through literature 11 2 3.

[B] Umbilical artery Interpolation on clinical data Interpolation on clinical data Fourier analysis Fourier analysis

Figure 2.16: Inlet velocity waveforms: From the obtained medical ultrasound data to periodic Fourier waveforms.

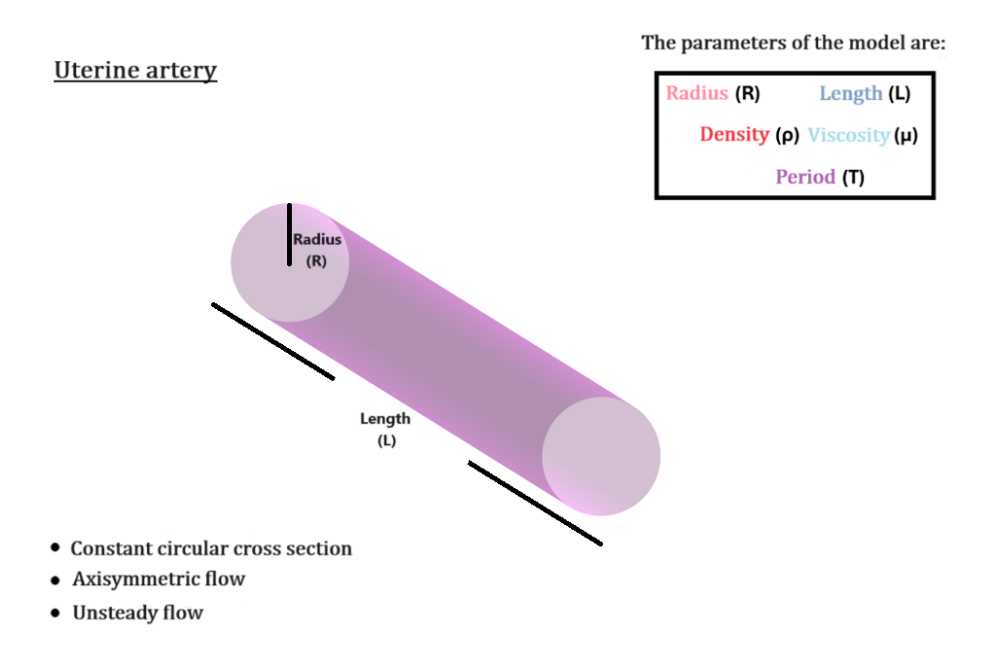


Figure 2.17: Schematic outline of the uterine arterial flow setup, with the flow parameters determined through literature 1 2 3.

Umbilical artery

Accounting for its helical structure, the umbilical artery is mathematically modeled as a helically coiled pipe of six turns of length L=330 mm and radius R=1.5 mm. The respected coil radius, R_c , is set to 5 mm, accounting for the radius of the umbilical vein. The derived umbilical coiling index, UCI, indicates a physiological coiling pattern. The helical structure is thought to offer

flexibility and resilience, enabling the umbilical cord to endure movements and avoid kinking or blockage, which is essential for maintaining consistent blood flow between the fetus and the placenta. The arterial wall is assumed to be rigid, the same as in the uterine artery.

The velocity inlet is again expressed in the form of (10), with the pulse period being $\frac{60}{140}$ s, providing with Wo $\simeq 3$. The latter is indicative of harmonized hemodynamics between the mother and fetus. The pressure outlet is now set at 20 mmHg, with the reference pressure set at 5 mmHg, simulating the intrauterine environment [11]. This is significantly lower than adult systemic pressures, but is appropriate for fetal circulation. The no-slip boundary condition is again imposed. As in the uterine artery, the flow is considered laminar, incompressible and non-Newtonian, under the same density and viscosity assumptions. The mesh independence test was conducted with a hexahedral grid, in the same manner as in the uterine artery, consisting of approximately 5×10^5 elements and 5.3×10^5 nodes. The RMS errors remained between 10^{-4} and 10^{-5} . Figure [2.18] shows a schematic outline of the umbilical arterial flow setup, with flow parameters determined through the literature [4] [5] [6].

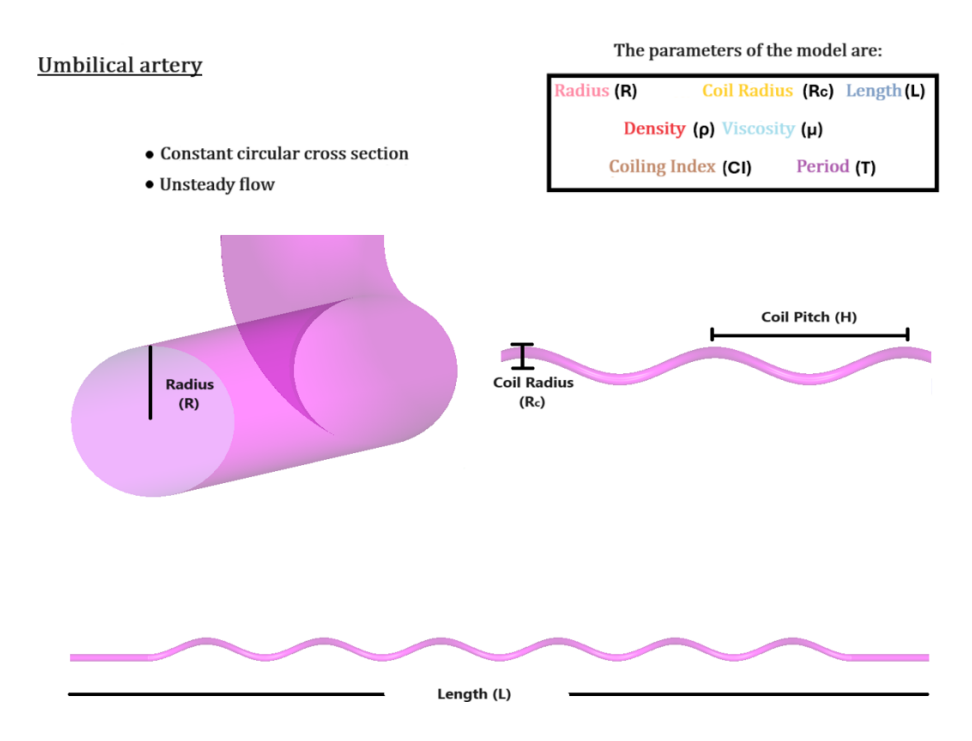


Figure 2.18: Schematic outline of the umbilical arterial flow setup, with the flow parameters determined through literature [4, 5, 6].

2.2 Results

2.2.1 Uterine arterial flow

The blood flow in the uterine artery exhibits laminar characteristics, as indicated by the Reynolds number (Re < 2300). This type of flow, devoid of turbulence, is ideal under physiological conditions, particularly during pregnancy, as it ensures an efficient and steady blood supply. In laminar flow, the maximum velocity occurs in the center of the artery, while the velocity near the vessel wall is lower. This distribution follows a typical cylindrical vessel parabolic velocity profile. Furthermore, the pressure drop across the uterine artery can be explained by the Hagen–Poiseuille law. This relationship is crucial in understanding the efficiency of blood supply through the artery. Table 2.3 provides the CFD-obtained measurements for the uterine artery, corresponding to the second trimester of pregnancy (21–22 weeks).

Uterine Artery				
2nd Trimester	Peak Systolic Velocity (PSV)	0.9378 m/s		
	End Diastolic Velocity (EDV)	0.4387 m/s		
	Time-Averaged Velocity (TAV)	0.5976 m/s		
	Resistance Index (RI)	0.5322		
	Pulsatility Index (PI)	0.8351		

Table 2.3: CFD-obtained measurements for the uterine artery (21–22 weeks).

PSV and EDV indicate that the uterine artery supplies an increased volume of blood, which is crucial during the second trimester to support the growing placenta and fetus. TAV further confirms that the uterine artery provides a stable blood supply with minimal pressure fluctuations and low velocity variation.

PI reflects the average pulsatility of blood flow, where a lower PI suggests continuous and stable perfusion—optimal for fetal growth. This stability ensures a smooth blood supply, without significant pressure variations between heart-beats. RI measures vascular resistance in the uterus, which remains within an optimal range, preventing excessive pressure on blood vessels while maintaining continuous flow. Pregnancy naturally reduces arterial resistance to accommodate the increasing blood supply needed for fetal development.

As pregnancy progresses, blood vessels adjust to maintain steady flow, preventing complications such as fetal growth restriction. The balance between vascular resistance and continuous perfusion is essential for a healthy intrauterine environment, ensuring efficient nutrient and oxygen exchange while minimizing shear stress on vessel walls. These physiological changes highlight the dynamic nature of maternal circulation and the importance of stable uteroplacental perfusion for fetal development. Figure 2.19 presents the uterine arterial flow during

the second trimester.

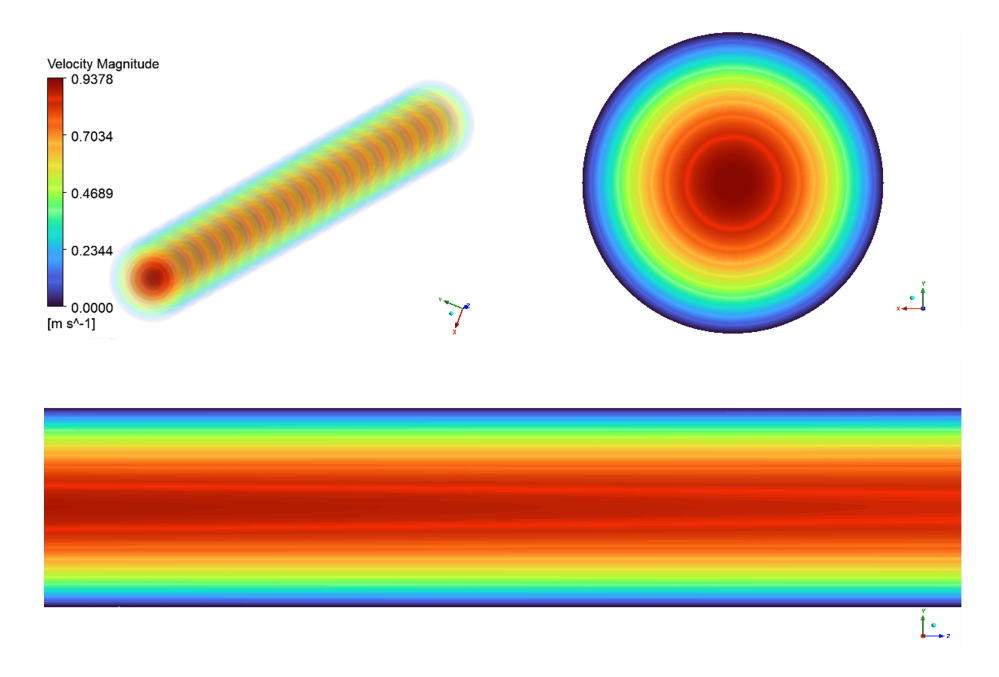


Figure 2.19: Blood flow in the uterine artery, during the 21-22 week groups.

The axial view of the uterine artery, shown in the top left of Figure 2.19 displays regular concentric ring patterns, indicating laminar rather than turbulent flow, as seen in larger arteries. The transition between colors in the flow field represents velocity variations, with the highest velocity at the center (red region) and decreasing toward the walls (green to blue regions). This characteristic velocity gradient follows a parabolic flow profile, where flow is fastest in the center and slowest near the vessel walls due to viscous effects. The upper right section of the figure presents a cross-sectional velocity vector field of the uterine artery. The central red region represents peak velocity, which gradually decreases outward into green and blue rings, reaching its lowest values near the outer walls. This profile indicates fully developed laminar flow, ensuring stable and efficient blood perfusion to the uterus.

The lower portion of the figure illustrates the longitudinal flow progression along the uterine artery. The nearly straight flow lines and smooth color gradient from red to blue indicate stable, turbulence-free flow. The gradual reduction in velocity toward the arterial wall further confirms laminar flow, ensuring efficient circulation within the artery.

Comparison with numerical data from multi-dimensional numerical methods

$$U = (u - \dot{x})y_{\eta} - (v - \dot{y})x_{\eta}, \quad V = (v - \dot{y})x_{\xi} - (u - \dot{x})y_{\xi}, \tag{2.81}$$

$$q_1 = x_\eta^2 + y_\eta^2$$
, $q_2 = x_\xi x_\eta + y_\xi y_\eta$, $q_3 = x_\xi^2 + y_\xi^2$. (2.82)

In the above, $x_{\xi}, x_{\eta}, y_{\xi}$, and y_{η} denote the transformation metrics, computed locally on each cell volume [42]. Based on the mixed formulation above, the dimensionless transport equations are transformed to follow the exact geometric characteristics of the vessel [2.83] - [2.85]. Furthermore, J is the determinant of the inverse Jacobian of the transformation, described in [9].

$$\frac{\partial J}{\partial t} + \frac{\partial U}{\partial \xi} + \frac{\partial V}{\partial \eta} = 0, \tag{2.83}$$

$$\frac{\partial(Ju)}{\partial t} + \frac{\partial(Uu)}{\partial \xi} + \frac{\partial(Vu)}{\partial \eta} = -\left(y_{\eta}\frac{\partial p}{\partial \xi} + y_{\xi}\frac{\partial p}{\partial \eta}\right) + \frac{\partial}{\partial \xi}\left[\frac{1}{J\operatorname{Re}}\left(q_{1}\frac{\partial u}{\partial \xi} - q_{2}\frac{\partial u}{\partial \eta}\right)\right] + \frac{\partial}{\partial \eta}\left[\frac{1}{J\operatorname{Re}}\left(q_{3}\frac{\partial u}{\partial \eta} - q_{2}\frac{\partial u}{\partial \xi}\right)\right],$$
(2.84)

$$\frac{\partial(Jv)}{\partial t} + \frac{\partial(Uv)}{\partial \xi} + \frac{\partial(Vv)}{\partial \eta} = -\left(x_{\xi}\frac{\partial p}{\partial \eta} - x_{\eta}\frac{\partial p}{\partial \xi}\right) + \frac{\partial}{\partial \xi}\left[\frac{1}{J\text{Re}}\left(q_{1}\frac{\partial v}{\partial \xi} - q_{2}\frac{\partial v}{\partial \eta}\right)\right] + \frac{\partial}{\partial \eta}\left[\frac{1}{J\text{Re}}\left(q_{3}\frac{\partial v}{\partial \eta} - q_{2}\frac{\partial v}{\partial \xi}\right)\right]$$
(2.85)

The FVM is used to numerically solve the aforementioned problem, under appropriate initial and boundary conditions (see 2.1.5). More information on FSI techniques can be found in [9]. Comparison of the FSI method with the KdVB mathematical model, throughout the cardiac cycle, shows good agreement.

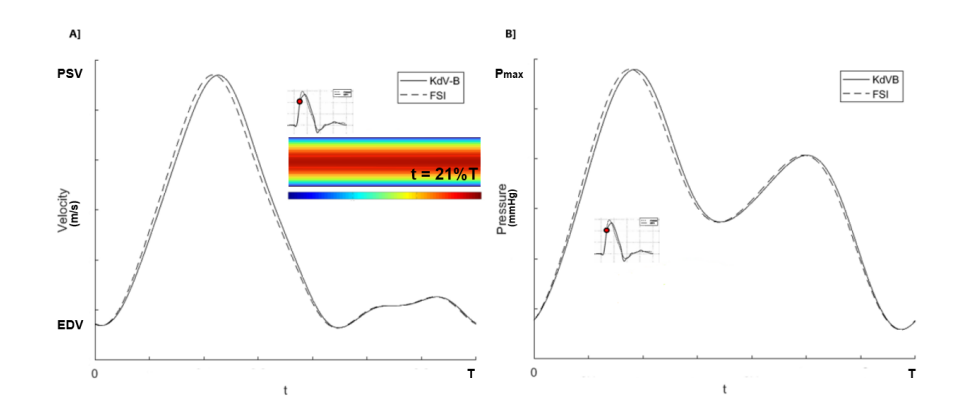


Figure 2.20: Comparison of the FSI method with the KdVB mathematical model, throughout the entire cardiac cycle (T). The values for the KdVB equation, that provide similar results with the FSI equations, are $\alpha=10^{-3}$, $\beta=10^{-4}$, and $\gamma=1$.

2.2.2 Umbilical arterial flow

The blood flow in the umbilical artery is also laminar, with a Reynolds number (Re < 2300) indicating a smooth laminar flow. However, due to the curvature of the artery, the Dean number (De > $40\sim60$) suggests the presence of secondary flow patterns, which result in vortex-like movements. These secondary flows disrupt the typical parabolic velocity profile observed in straight vessels, with the highest velocity occurring along the outer curve of the artery rather than in the center. This is a normal consequence of the geometry of the vessel.

Umbilical Artery					
2nd Trimester	Peak Systolic Velocity (PSV)	0.3977 m/s			
	End Diastolic Velocity (EDV)	0.1226 m/s			
	Time-Averaged Velocity (TAV)	0.2481 m/s			
	Resistance Index (RI)	0.6917			
	Pulsatility Index (PI) 1.1088				
	Time-Averaged Wall Shear Stress (TAWSS)	Min: 0.3921 Pa	Max: 3.4407 Pa	Avg: 1.9164 Pa	
	Oscilatory Shear Index (OSI)	Min: 0.0745	Max: 0.2674	Avg: 0.1710	
	Relative Residence Time (RRT)	Min: 0.3415 Pa ⁻¹	Max: 5.4823 Pa ⁻¹	Avg: 2.9119 Pa ⁻¹	
3rd Trimester	Peak Systolic Velocity (PSV) 0.4595 m/s				
	End Diastolic Velocity (EDV)	0.1757 m/s			
	Time-Averaged Velocity (TAV)	AV) 0.2870 m/s			
	Resistance Index (RI)	0.6176			
	Pulsatility Index (PI)	0.9888			
	Time-Averaged Wall Shear Stress (TAWSS)	Min: 0.4337 Pa	Max: 4.5490 Pa	Avg: 2.4914 Pa	
	Oscilatory Shear Index (OSI)	Min: 0.0826	Max: 0.2958	Avg: 0.1892	
	Relative Residence Time (RRT)	Min: 0.2633 Pa ⁻¹	Max: 5.6458 Pa ⁻¹	Avg: 2.9545 Pa ⁻¹	

Table 2.4: CFD-obtained measurements for the umbilical artery, corresponding to the second trimester of pregnancy (21-22 weeks) and the third trimester of pregnancy (30-31 weeks).

The CFD-obtained measurements provide valuable insights into the hemodynamic changes occurring in the umbilical artery between the second and third trimesters. In comparing the two trimesters, several trends emerge that reflect the physiological adaptations necessary to support fetal growth.

Peak systolic velocity (PSV) increases as pregnancy progresses, indicating a rise in blood flow velocity during systole. Similarly, end diastolic velocity (EDV) increases, suggesting a reduction in downstream resistance and improved continuous blood flow to the fetus. The time-averaged velocity (TAV) also increases, reinforcing the observation of an increase in overall blood flow.

The resistance index (RI) decreases, which is in line with the expected reduction in placental vascular resistance as pregnancy progresses. A similar trend is seen in the pulsatility index (PI), which also decreases, suggesting improved perfusion and better regulation of blood flow.

Wall shear stress parameters also exhibit notable changes. TAWSS is a key factor in maintaining vascular health, as adequate shear stress promotes proper endothelial function and vessel remodeling 12 13 14 15. TAWSS is defined as the average magnitude of the wall shear stress vector $\vec{\tau}_w(t)$ over one cardiac cycle of duration T:

$$TAWSS = \frac{1}{T} \int_0^T |\vec{\tau}_w(t)| dt \qquad (2.86)$$

where $\vec{\tau}_w(t)$ and T denote the instantaneous wall shear stress vector at time t and the duration of the cardiac cycle, respectively. The increase in TAWSS during the third trimester indicates that the artery is adapting to higher blood flow demands. OSI, on the other hand, provides insight into the bidirectional nature of shear stress [12, 13, 15]. More precisely OSI quantifies the directional change of wall shear stress, measuring the flow oscillation over the cycle:

OSI =
$$\frac{1}{2} \left(1 - \frac{\left| \int_0^T \vec{\tau}_w(t) dt \right|}{\int_0^T |\vec{\tau}_w(t)| dt} \right)$$
 (2.87)

OSI ranges from 0 (unidirectional flow) to 0.5 (purely oscillatory flow). While high OSI values can be associated with disturbed flow and potential vascular dysfunction, the measured values suggest that oscillations in shear stress remain within a normal range. RRT, which is an indicator of how long blood pools, is important in assessing the risk of thrombosis or impaired perfusion [12] [15]. RRT describes the residence time of blood particles near the vessel wall and is defined, using (2.86) and (2.87), as:

$$RRT = \frac{1}{(1 - 2 OSI) \cdot TAWSS}$$
 (2.88)

The slight increase in RRT in the third trimester does not appear to be of concern, as it remains within expected physiological limits. These findings align with the

normal hemodynamic changes expected in normal pregnancy, reinforcing the importance of maintaining proper vascular function for optimal fetal growth.

The secondary flow promotes the mixing of blood constituents, which is essential for two key reasons: the efficient transport of oxygen and nutrients to tissues and the removal of metabolic by-products. Continuous mixing facilitated by secondary flow promotes the efficient delivery of essential nutrients to the fetus and the removal of metabolic waste [43]. Additionally, secondary flow helps prevent stagnation zones—areas of near-zero velocity—thereby reducing the risk of thrombosis within the umbilical arteries. Moreover, disruptions in secondary flow patterns can serve as early indicators of complications such as reduced blood flow or placental insufficiency, aiding in timely diagnosis and intervention. Figure [2.21] depicts the development of secondary flow patterns within the umbilical artery.

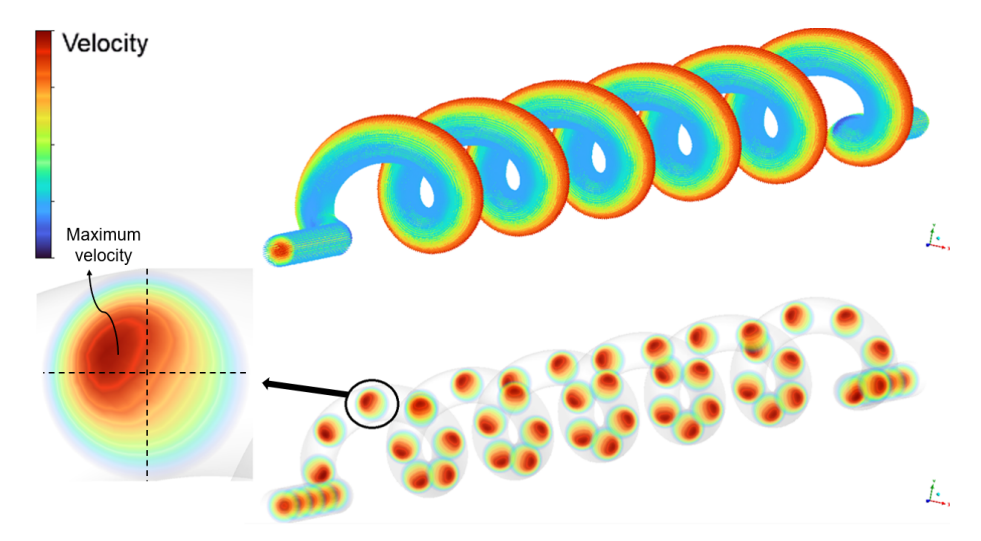


Figure 2.21: Visualization of secondary flow in the helical umbilical artery model.

The top part shows the three-dimensional geometry of the umbilical artery with color-mapped streamlines indicating the axial velocity distribution along the vessel. The bottom part presents cross-sectional velocity contours at multiple locations along the helical path, revealing the development and persistence of secondary flow vortices. The detailed inset highlights the off-center velocity maximum and characteristic vortex structure in a representative cross-section, clearly demonstrating the formation of Dean-type secondary flows due to vessel curvature.

Next, two graphical illustrations of the velocity are shown (Figure 2.22) with regard to the second and third trimesters of pregnancy. The geometry of the umbilical artery contributes to complex blood flow patterns, which are crucial for efficient oxygen and nutrient delivery to the fetus during the late stages of pregnancy.

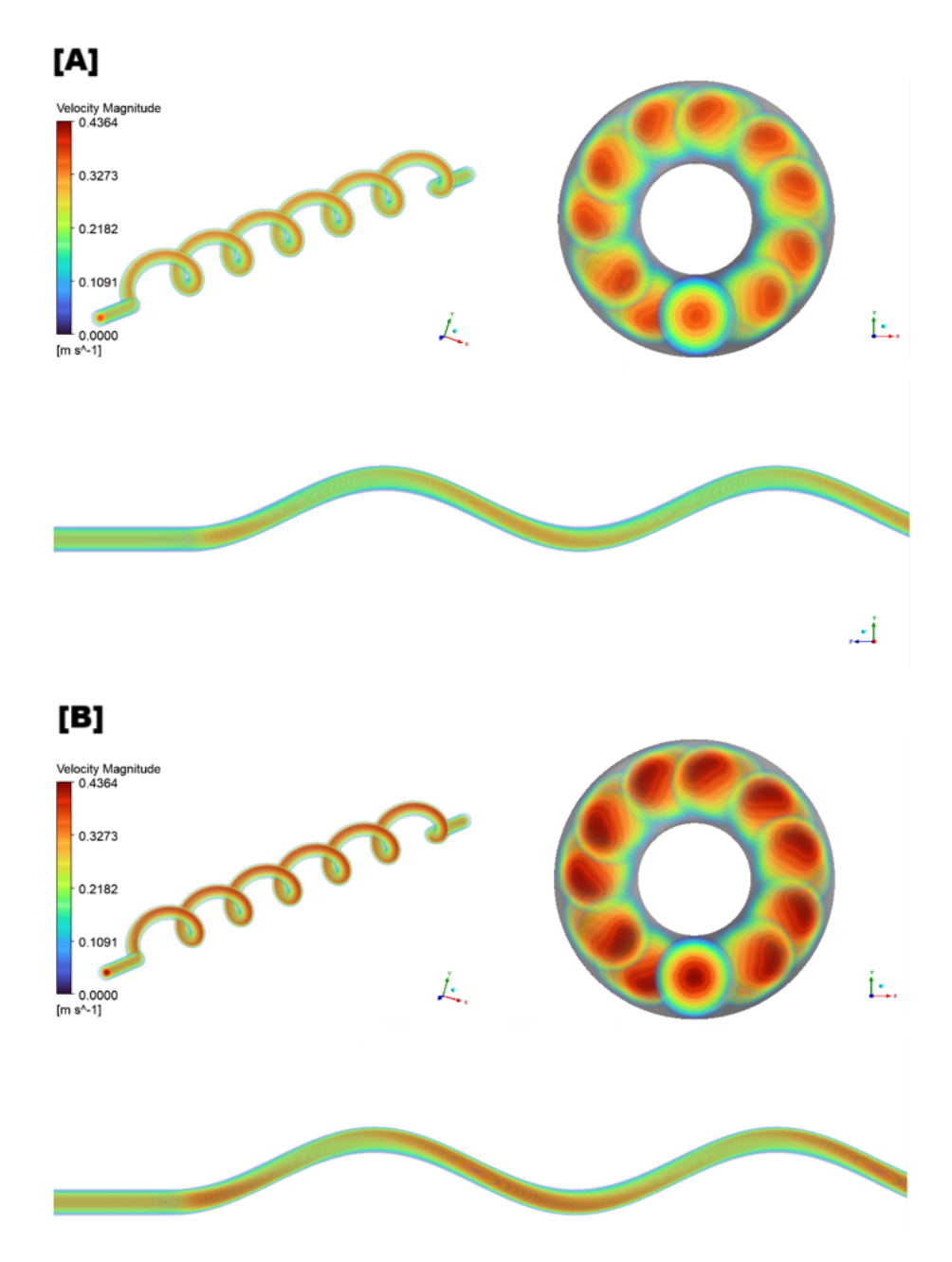


Figure 2.22: (A) Simulation of blood flow in the umbilical artery, during the 21-22 week groups (second trimester). The helical flow pattern is evident, reflecting the artery's coiled structure. (B) Simulation of blood flow in the umbilical artery, during the 30-31 week groups (third trimester).

The upper left of Figure 2.22 depicts a helical or spiral flow pattern, characteristic of blood flow through the coiled umbilical artery. The alternating high- and low-velocity regions along the helix suggest a swirling flow field, influenced by the artery's ability to stretch and twist in response to fetal movements. The more pronounced helical structure observed in the third trimester reflects a physiological adaptation to meet the increasing circulatory demands of the growing fetus. The upper right section presents cross-sectional views of the umbilical artery. High-velocity regions appear near the outer walls, while lower-velocity areas are concentrated toward the center. The third trimester exhibits a more intense velocity magnitude, indicating higher energy and momentum transfer driven by increased fetal demands.

The lower portion of the figure shows longitudinal slices of blood flow through the artery. The wavy pattern, represented by alternating colors, reflects variations in velocity caused by the helical flow. This undulating waveform becomes more defined in the third trimester, suggesting increased pulsatility and enhanced adaptability to fetal circulation. The Time-Averaged Wall Shear Stress (TAWSS) distributions for the second and third trimesters are shown in Figure [2.23]

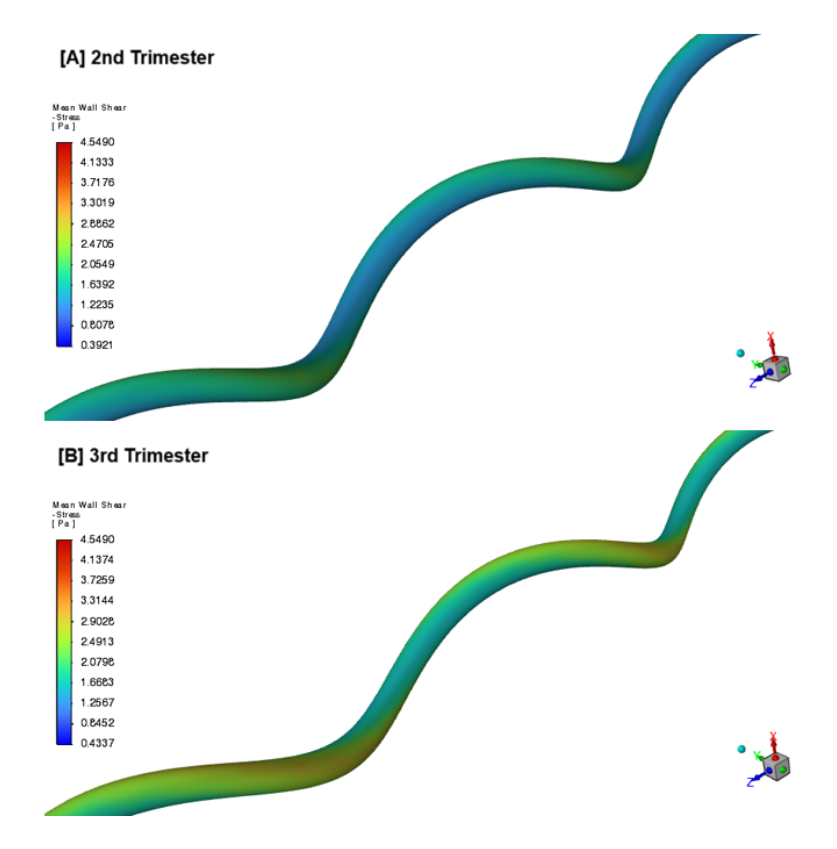


Figure 2.23: Time-averaged wall shear stress (TAWSS) distribution in the umbilical artery during the 2nd (**A**) and 3rd trimester (**B**) of pregnancy.

2.3 Discussion

This study provides a detailed analysis of blood flow dynamics in the uterine and umbilical arteries during pregnancy, contributing to a clearer understanding of maternal-fetal circulation, using CFD models [9, [21, 25, 26]. The integration of Doppler ultrasound data with mathematical models based on the Navier–Stokes equations allows the quantification of hemodynamic parameters such as Peak Systolic Velocity (PSV), Pulsatility Index (PI), and Resistance Index (RI) under physiological conditions. A key advancement in this work lies in the transient three-dimensional solution of the Navier–Stokes equations with parabolic velocity inlets, derived from spectral Fourier analysis of Doppler ultrasound data. This extends previous studies [4, 6, 10] by incorporating real-time statistical analysis to refine the flow setup.

A major finding of this study is that CFD offers explicit and quantitative visualization of blood flow patterns in the umbilical artery—an advantage not provided by traditional observation methods such as Doppler ultrasound. While Doppler ultrasound primarily estimates blood flow direction and velocity based on the angle of the ultrasonic beam, CFD enables the visualization of streamlines, velocity distributions, and instantaneous particle motion, providing a more detailed hemodynamic assessment. Furthermore, CFD reveals the presence of secondary flow patterns within the umbilical artery, which interact with the primary flow along the vessel's trajectory—phenomena that are difficult to capture using ultrasound alone. This enhanced visualization allows for a more comprehensive understanding of the relationship between umbilical arterial hemodynamics and fetal growth, improving clinical assessments.

The focus on the second and third trimesters stems from their critical role in maternal-fetal health, as evidenced by our statistical analysis. During this period, the rapid growth of the fetus and the continued development of the placenta significantly alter blood flow dynamics, increasing the risk of complications such as preeclampsia and intrauterine growth restriction (IUGR). These findings align with prior research [I, [2], [III]], emphasizing the importance of noninvasive Doppler ultrasonography for monitoring uterine and umbilical blood flow. While Doppler ultrasound remains a valuable clinical tool, the ability of CFD to visualize pressure and wall shear stress (WSS) distribution provides additional insight into vascular resistance and flow adaptations during pregnancy.

The results confirm that blood flow in the uterine artery remains predominantly laminar, with stable PSV and EDV across gestation. The observed decrease in PI and RI between the second-trimester groups suggests a reduction in vascular resistance, which stabilizes in the third trimester. These findings support the notion of progressive maternal hemodynamic adaptation, ensuring continuous placental perfusion without excessive pressure fluctuations.

The computed TAWSS values in the uterine artery indicate a relatively uniform shear stress distribution, which is essential for maintaining endothelial function and supporting efficient oxygen and nutrient exchange. The consistently low OSI values confirm that flow remains unidirectional, reinforcing the stability of the uterine blood supply. Additionally, the low RRT suggests that blood does

not pool, which is crucial in preventing thrombotic complications that could compromise placental function.

In contrast, the umbilical artery exhibits more complex flow characteristics due to its helical structure. The computed Dean number (De > 40) confirms the presence of secondary vortical flows, which enhance mixing and facilitate oxygen transport. The observed increase in PSV and EDV between the second and third trimesters is consistent with the physiological expectation of increasing fetal metabolic demand and decreasing placental vascular resistance.

The increase in TAWSS in the umbilical artery during the third trimester reflects vessel adaptation to higher volumetric flow rates, ensuring adequate perfusion of the fetus. The moderate values of OSI indicate the expected oscillatory nature of shear stress due to the coiled morphology of the artery, but do not suggest excessive flow disturbances. A slight increase in RRT is observed in the third trimester, which may improve the efficiency of nutrient exchange but could also indicate a slightly prolonged residence time of the blood, which requires careful clinical evaluation in pathological cases.

These findings emphasize the importance of monitoring uteroplacental hemodynamics to detect pregnancy complications such as fetal growth restriction (FGR) or placental insufficiency. An abnormal decrease in TAWSS or a pathological increase in OSI and RRT could serve as early markers of vascular dysfunction, warranting closer clinical surveillance. This study also reinforces the value of CFD as a complementary tool to Doppler ultrasound by providing a more detailed visualization of secondary flow structures, which are otherwise difficult to observe.

Despite its contributions, this study has some limitations. The idealized arterial geometries, as in previous work [4], [10], may not fully capture patient-specific vascular variations. The assumption of laminar flow does not account for potential turbulence in pathological cases, limiting the applicability of the model to abnormal pregnancies. Additionally, while the dataset of 200 pregnant women strengthens the statistical analysis, broader studies across different populations and gestational stages could improve generalizability.

The Carreau model more accurately represents blood's viscoelasticity than simpler models (e.g., Newtonian or power-law), as it accounts for both low- and high-shear-rate behavior. This formulation provides a balance between physiological fidelity and computational tractability, making it a cornerstone in hemodynamic modeling. Variants like the Carreau-Yasuda or Carreau-Gambaruto models could also be studied, potentially offering refinements for specific hematocrit or protein concentrations [44]. Future research could enhance these models by incorporating patient-specific vascular geometries reconstructed from ultrasound imaging and expanding CFD simulations to include cases of turbulent flow.

By bridging the gap between physiology and computational modeling, this study advances the understanding of pregnancy hemodynamics, particularly in the second and third trimesters when circulatory demands are at their highest. The application of CFD modeling alongside Doppler ultrasound offers a powerful tool for improving maternal-fetal medicine by providing deeper insight into vascular adaptations and potential complications. Integrating CFD simula-

tions into clinical assessments can enhance early diagnosis and management of pregnancy-related disorders, offering better maternal and fetal health outcomes.

2.4 Conclusions

This study utilized computational fluid dynamics (CFD) and mathematical modeling to analyze maternal-fetal blood flow, integrating Doppler ultrasound data with Navier–Stokes models. A key finding is that CFD provides a more detailed and quantitative visualization of blood flow than traditional imaging methods, capturing complex flow patterns such as secondary flows in the umbilical artery, phenomena difficult to observe with ultrasound alone. This enhanced visualization improves our understanding of umbilical arterial hemodynamics and its link to fetal growth restriction.

Simulations confirmed that uterine artery flow remains laminar, with stable PSV and EDV across trimesters, while the umbilical artery exhibits secondary flow patterns due to its helical structure. The observed increase in umbilical artery PSV and EDV between the second and third trimester reflects increased fetal metabolic demand and a reduction in placental vascular resistance. CFD analysis also revealed critical hemodynamic parameters such as time-averaged wall shear stress (TAWSS), oscillatory shear index (OSI), and relative residence time (RRT). The increase in TAWSS in the umbilical artery indicates vascular adaptation to higher blood flow demands, while the moderate OSI values confirm expected oscillatory behavior due to the vessel's coiled structure. Additionally, the slight increase in RRT suggests prolonged blood residence time, which may enhance nutrient exchange but could also indicate potential thrombotic risk in certain cases. Importantly, all simulations assumed blood's non-Newtonian behavior, reflecting its shear-dependent viscosity, which is critical for accurately modeling pulsatile flow dynamics and wall shear stresses in uterine and umbilical arteries. This assumption enhances the physiological relevance of the CFD results and supports more precise hemodynamic assessments.

While this study provides valuable insights using CFD and Doppler ultrasound integration, several limitations should be acknowledged. The modeling relied on idealized arterial geometries rather than fully patient-specific vessel reconstructions, which may limit the generalizability of flow patterns. Additionally, the limitations of Doppler ultrasound image resolution posed challenges for detailed three-dimensional segmentation. In future work, we plan to employ advanced reconstruction tools to generate patient-specific models, which could provide even more realistic representations of the vascular domains. Furthermore, assumptions inherent in the employed non-Newtonian rheological models and simplifications related to steady versus transient flow states may affect the accuracy of simulated hemodynamics. Technical factors such as mesh resolution and convergence criteria were carefully monitored.

No in-vivo experimental data are available for direct validation in this study. Therefore, to verify the accuracy of our computational approach, we performed benchmark simulations of fully developed laminar flows in the vessel geometries.

Specifically, velocity profiles and pressure drops obtained from simulations were compared against well-established theoretical solutions of the Navier–Stokes equations, including the Hagen–Poiseuille flow for steady pressure-driven flow in straight circular pipes, the Womersley flow describing pulsatile velocity profiles in oscillatory arterial flow, and the Dean flow characterizing secondary flow patterns in curved tubes. These classical flow solutions provide essential reference cases that underpin the validation of CFD models in physiological flow simulations.

Moreover, although parameters like Wall Shear Stress (TAWSS), Oscillatory Shear Index (OSI), and Relative Residence Time (RRT) show promise as markers of vascular adaptation and dysfunction, there are currently no established clinical thresholds for these indices in uteroplacental circulation. Defining such diagnostic benchmarks requires larger-scale, longitudinal clinical studies.

By establishing population-specific blood flow parameters, this study enhances clinical assessments and the detection of complications such as placental insufficiency and fetal growth restriction (FGR). The findings emphasize the importance of monitoring uteroplacental hemodynamics to detect potential complications early. An abnormal decrease in TAWSS or a pathological increase in OSI and RRT could serve as early markers of vascular dysfunction, warranting closer clinical surveillance. While CFD is not yet standard in clinical practice, its ability to reveal flow patterns beyond the reach of ultrasound highlights its potential as a complementary diagnostic tool.

2.4.1 Future directions

Building upon the findings of this study, several important avenues for future research are proposed. One key direction is the study of blood flow under the influence of striations or elastic plates on the arterial walls, which may provide deeper insights into the hemodynamic behavior and vascular mechanics of the arteries examined. Another crucial step is the incorporation of fluid-structure interaction (FSI) in future models to account for the dynamic movement of arterial walls during the cardiac cycle, thereby capturing more physiologically accurate flow dynamics and wall shear stress distributions. Furthermore, exploring advanced hemodynamic biomarkers such as helicity, vorticity, and others could enhance our understanding of complex flow features related to vascular function and pathology.

In addition, demographic studies involving clinical data from diverse geographic or population groups are necessary to identify potential differences in uteroplacental hemodynamics; such differences could inform the development of population-specific diagnostic benchmarks and treatment strategies. Considering the influence of fetal weight in the formation of velocity profiles in the arteries under study may improve the accuracy of simulations by reflecting physiological changes associated with fetal growth.

Moreover, future work should emphasize the incorporation of patient-specific vascular geometries reconstructed from ultrasound imaging, expanding real-time computational fluid dynamics (CFD) applications to include pathological conditions. The application of machine learning algorithms trained on Doppler

ultrasound data holds promise for refining diagnostic capabilities, enabling predictive modeling for pregnancy complications. The continued integration of CFD simulations into clinical assessments is expected to facilitate earlier diagnosis and more effective management of pregnancy-related disorders, ultimately improving maternal and fetal health outcomes.

Pursuing these directions will refine computational models and enhance their clinical relevance, contributing to earlier and more precise diagnosis of pregnancy-related vascular complications.

Supplemental Material

This chapter provides supplemental materials that complement the research presented in this thesis. These resources include code, data analyses, and simulation files.

Statistical analysis

The detailed statistical analysis of the Doppler ultrasound dataset—including preprocessing, descriptive statistics, hypothesis testing, and visualizations—is available at the following link:

• Statistical Analysis of Doppler Ultrasound Data

Waveform construction notebooks

Wolfram Mathematica notebooks used for the construction, using interpolation and Fourier analysis, of the uterine and umbilical artery blood flow waveforms are available here:

- Uterine Artery Waveform Modeling and Analysis
- Umbilical Artery Waveform Modeling and Analysis

CFD simulation files

Simulation files created with Ansys Fluent (2025 R1 Academic, 16.1 Academic) for uterine and umbilical arterial blood flow modeling—including input files, mesh data, and solver settings—can be accessed via the following links:

- Uterine Artery CFD Simulations
- Umbilical Artery CFD Simulations

For any issues accessing the files or further inquiries, please contact the author.

Note: Due to privacy and ethical considerations, raw patient data are not publicly shared.

Chapter 3

Abstracts

This chapter contains the abstract of the study in both English and Greek. As the thesis is written in English, a brief overview of the thesis is also provided in Greek alongside the Greek abstract.

3.1 Abstract in English

The study employs Computational Fluid Dynamics (CFD) and mathematical modeling to analyze uterine and umbilical arterial blood flow during pregnancy, offering a detailed understanding of hemodynamic changes throughout gestation. Statistical analysis of Doppler ultrasound data from a large cohort of more than 200 pregnant women (in the second and third trimesters) reveals significant increases in the umbilical arterial peak systolic velocity (PSV) between the 22nd and 30th weeks, while uterine artery velocities remain relatively stable, suggesting adaptations in vascular resistance during pregnancy. By combining the Navier-Stokes equations with Doppler ultrasound-derived inlet velocity profiles, we quantify several key fluid dynamics parameters, including time-averaged wall shear stress (TAWSS), oscillatory shear index (OSI), relative residence time (RRT), Reynolds number (Re), and Dean number (De), evaluating laminar flow stability in the uterine artery and secondary flow patterns in the umbilical artery. Since blood exhibits shear-dependent viscosity and complex rheological behavior, modeling it as a non-Newtonian fluid is essential to accurately capture pulsatile flow dynamics and wall shear stresses in these vessels. Unlike conventional imaging techniques, CFD offers enhanced visualization of blood flow characteristics such as streamlines, velocity distributions, and instantaneous particle motion, providing insights that are not easily captured by Doppler ultrasound alone. Specifically, CFD reveals secondary flow patterns in the umbilical artery, which interact with the primary flow, a phenomenon that is challenging to observe with ultrasound. These findings refine existing hemodynamic models, provide population-specific reference values for clinical assessments, and improve our understanding of the relationship between umbilical arterial flow dynamics

and Intrauterine Growth Restriction (IUGR), with important implications for maternal and fetal health monitoring.

3.2 Abstract in Greek

Η μελέτη αξιοποιεί την Υπολογιστική Ρευστοδυναμική (CFD) και τη μαθηματική μοντελοποίηση για την ανάλυση της ροής του αίματος στη μήτρα και στον ομφάλιο λώρο κατά τη διάρκεια της εγκυμοσύνης, προσφέροντας μια λεπτομερή κατανόηση των αιμοδυναμικών αλλαγών καθ' όλη τη διάρκεια της κύησης. Η στατιστική ανάλυση δεδομένων υπερηχογραφικού Doppler από ένα μεγάλο δείγμα, αποτελούμενο από περισσότερες από 200 έγχυες γυναίχες στο δεύτερο και τρίτο τρίμηνο της κύησης, αποκαλύπτει σημαντική αύξηση της μέγιστης συστολικής ταχύτητας της ομφαλικής αρτηρίας (PSV) μεταξύ της 22ης και της 30ής εβδομάδας, ενώ οι ταχύτητες στη μητριαία αρτηρία παραμένουν σχετικά σταθερές, υποδηλώνοντας προσαρμογές στην αγγειακή αντίσταση κατά τη διάρκεια της εγκυμοσύνης. Με τη συνδυαστική χρήση των εξισώσεων Navier-Stokes και των προφίλ ταχύτητας εισόδου που προχύπτουν από υπερήχους Doppler, ποσοτιχοποιούνται διάφορες βασιχές παράμετροι της δυναμικής των ρευστών, όπως η μέση διατμητική τάση τοιχώματος (TAWSS), ο δείχτης ταλαντευόμενης διάτμησης (OSI), ο σχετικός χρόνος παραμονής (RRT), ο αριθμός Reynolds (Re) και ο αριθμός Dean (De). Μέσα από αυτήν την ανάλυση αξιολογείται η σταθερότητα της στρωτής ροής στη μητριαία αρτηρία, καθώς και η δευτερογενής ροή στην ομφαλική αρτηρία. Επειδή το αίμα χαρακτηρίζεται από ιξώδες εξαρτώμενο από τη διάτμηση με σύνθετη ρεολογική συμπεριφορά, η μοντελοποίησή του ως μη-Νευτώνειο ρευστό είναι απαραίτητη για την αχριβή αποτύπωση της δυναμικής της παλμικής ροής και των διατμητικών τάσεων στα τοιχώματα των υπό μελέτη αγγείων. Σε αντίθεση με τις συμβατικές απεικονιστικές τεχνικές, η CFD παρέχει βελτιωμένη απεικόνιση χαρακτηριστικών της ροής του αίματος, όπως γραμμές ροής, κατανομές ταχύτητας και πίεσης, προσφέροντας πολύτιμες πληροφορίες που δεν αποτυπώνονται εύχολα μέσω του υπερηχογραφήματος Doppler. Συγκεκριμένα, η ανάλυση αποκαλύπτει μοτίβα δευτερογενούς ροής στην ομφαλική αρτηρία, τα οποία αλληλεπιδρούν με την κύρια ροή – ένα φαινόμενο δύσκολα παρατηρήσιμο μέσω υπερήχων. Τα ευρήματα αυτά συμβάλλουν στη βελτίωση των υπαρχόντων αιμοδυναμικών μοντέλων, παρέχουν τιμές αναφοράς για συγχεχριμένους πληθυσμούς προς χρήση σε χλινιχές αξιολογήσεις, και ενισχύουν την κατανόηση της σχέσης μεταξύ της δυναμικής της ομφαλικής αρτηριαχής ροής και της ενδομήτριας καθυστέρησης της ανάπτυξης (IUGR), με σημαντικές συνέπειες για την παρακολούθηση της υγείας τόσο της μητέρας όσο και του εμβρύου.

3.2.1 Review of the thesis (in Greek)

Η παρούσα υποενότητα παρουσιάζει μία εκτενή ανασκόπηση της Διδακτορικής Διατριβής του κ. Αναστάσιου Φελιά με τίτλο «Προσομοιώσεις Υπολογιστικής Ρευστοδυναμικής (CFD) στη Μαθηματική Μοντελοποίηση της Αιματικής Ροής Μητριαίων και Ομφαλικών Αρτηριών μέσω Απλουστευμένων και Ανώτερης Τάξης

Μαθηματικών Μοντέλων». Για την αποσαφήνιση της συνολικής ροής εργασίας της παρούσας μελέτης, στο Σ χήμα 3.1 παρουσιάζεται ένα σχηματικό διάγραμμα που απεικονίζει τα βασικά βήματα της μεθοδολογίας.

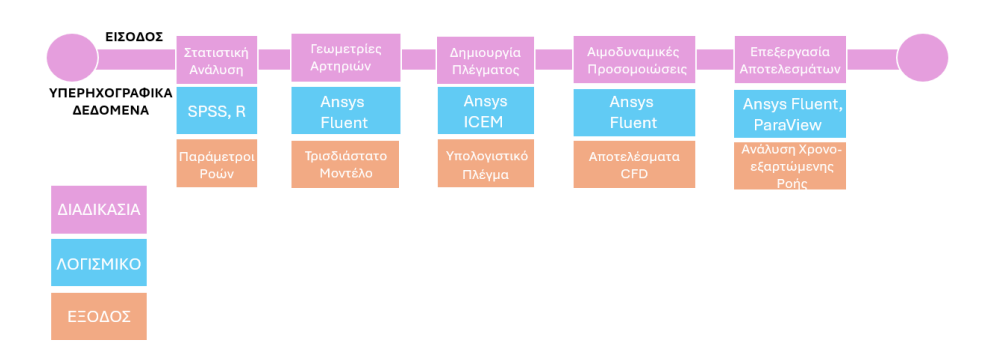


Figure 3.1: Περιληπτική παρουσίαση της μεθοδολογίας που υιοθετήθηκε για την εκπόνηση της μελέτης.

Η ροή του αίματος στη μήτρα και στον ομφάλιο λώρο παίζει καθοριστικό ρόλο για την υγεία μητέρας και εμβρύου, επηρεάζοντας την ανάπτυξη και την ευημερία του εμβρύου καθ' όλη τη διάρκεια της κύησης. Η σύνθετη αλληλεπίδραση φυσιολογικών παραγόντων και γεωμετρικών ιδιαιτεροτήτων δημιουργεί προκλήσεις για την ακριβή μοντελοποίηση και πρόβλεψη αυτής της ροής. Η διατριβή αυτή αντιμετωπίζει τις προκλήσεις με τη χρήση προσομοιώσεων υπολογιστικής ρευστοδυναμικής (CFD) και σύγχρονων μαθηματικών μοντέλων, στηριζόμενη σε εκτενή στατιστική ανάλυση δεδομένων υπερήχων Doppler από μεγάλο δείγμα Ελληνίδων εγκύων γυναικών.

Η εφαρμογή της CFD ξεκίνησε στα μέσα του 20ού αιώνα, με την ανάπτυξη των ψηφιακών υπολογιστών και το πρωτοποριακό έργο των John von Neumann και Stanislaw Ulam. Αρχικά εστιάζοντας στην αεροδυναμική και τη μεταφορά θερμότητας, η CFD εξελίχθηκε σε διεπιστημονικό εργαλείο που εφαρμόζεται πλέον και στη βιοϊατρική μηχανική και στην αλληλεπίδραση ρευστού-δομής (FSI). Στην παρούσα μελέτη, η CFD παρέχει μια ισχυρή προσέγγιση για την οπτικοποίηση και ποσοτική ανάλυση της αιματικής ροής στη μήτρα και τον ομφάλιο λώρο, προσφέροντας δεδομένα που υπερβαίνουν αυτά που προκύπτουν αποκλειστικά μέσω υπερηχογραφικών μετρήσεων.

Με στόχο την εμβάθυνση της κατανόησης της αιμοδυναμικής των μητριαίων και ομφαλικών αρτηριών, ιδιαίτερα σε επιπλοκές όπως η προεκλαμψία και ο ενδομήτριος περιορισμός ανάπτυξης, η μελέτη πραγματοποιεί τρισδιάστατες προσομοιώσεις χρονοεξαρτώμενης ροής, με προφίλ ταχύτητας εισόδου βασισμένα σε δεδομένα Doppler, από πάνω από 200 Ελληνίδες εγκύους, κυρίως στη διάρκεια του δεύτερου και τρίτου τριμήνου. Η στατιστική ανάλυση υπογραμμίζει σημαντική αύξηση στη μέγιστη συστολική ταχύτητα (PSV) της ομφαλικής αρτηρίας μεταξύ 22ης και 30ης εβδομάδας κύησης, ενώ τα προφίλ ροής στη μητριαία αρτηρία παραμένουν σχετικά σταθερά, υποδηλώνοντας αγγειακές προσαρμογές κατά την πάροδο

της κύησης.

Η μαθηματική μοντελοποίηση βασίζεται στις εξισώσεις Navier-Stokes, εμπλουτισμένες με τις μη-Νευτώνειες ιδιότητες του αίματος, ώστε να απειχονιστεί με αχρίβεια η δυναμική της παλμικής ροής και οι κατανομές της διατμητικής τάσης. Κύριοι αιμοδυναμικοί δείκτες, όπως η μέση διατμητική τάση τοιχώματος (TAWSS), ο δείκτης ταλαντούμενης διάτμισης (OSI), ο δείκτης σχετικού χρόνου παραμονής (RRT), καθώς και οι αριθμοί Reynolds (Re) και Dean (De), ποσοτικοποιούνται για την εκτίμηση της σταθερότητας της στρωτής ροής στη μήτρα και των μοτίβων δευτερογενούς ροής στην ομφαλική αρτηρία. Η ανίχνευση μοτίβων δευτερογενούς ροής στην ομφαλική αρτηρία αποκαλύπτει τη σύνθετη αλληλεπίδραση μεταξύ πρωτογενών και δευτερευόντων ροών, κάτι που δεν είναι εύκολα αντιληπτό μόνο από υπερηχογραφικές μετρήσεις. Οι αρτηρίες της μήτρας και του ομφάλιου λώρου προσεγγίζονται με απλοποιημένες γεωμετρίες, όπως ευθείς και ελικοειδείς κυλινδρικές αρτηρίες, επιτρέποντας την πραγματοποίηση λεπτομερών αριθμητικών προσομοιώσεων με προηγμένο λογισμικό CFD. Τα αποτελέσματα επικυρώνονται μέσω σύγχρισης με μαθηματικά και θεωρητικά μοντέλα, παρέχοντας αξιόπιστες αιμοδυναμικές τιμές αναφοράς για τον Ελληνικό πληθυσμό.

Οι προσομοιώσεις επιβεβαίωσαν ότι η ροή στην μητριαία αρτηρία παραμένει στρωτή, με σχετικά σταθερές PSV και EDV κατά τη διάρκεια των τριμήνων, ενώ η ομφαλική αρτηρία παρουσιάζει μοτίβα δευτερογενούς ροής λόγω της ελικοειδούς της δομής. Η παρατηρούμενη αύξηση των τιμών PSV και EDV στην ομφαλική αρτηρία μεταξύ δεύτερου και τρίτου τριμήνου αντανακλά το αυξημένο εμβρυϊκό μεταβολική φόρτο και τη μείωση της αγγειακής αντίστασης του πλακούντα. Η αύξηση του TAWSS στην ομφαλική αρτηρία υποδηλώνει αγγειακή προσαρμογή σε υψηλότερες απαιτήσεις ροής αίματος, ενώ οι μέτριες τιμές του ΟSΙ επιβεβαιώνουν την αναμενόμενη ταλαντούμενη συμπεριφορά που οφείλεται στην ελιχοειδή δομή του αγγείου. Επιπλέον, η ελαφρά αύξηση του RRT υποδηλώνει παρατεταμένο χρόνο παραμονής του αίματος, που δύναται να ενισχύει την ανταλλαγή θρεπτιχών ουσιών αλλά επίσης να υποδειχνύει πιθανό θρομβωτιχό χίνδυνο σε ορισμένες περιπτώσεις. Σημαντικό είναι ότι όλες οι προσομοιώσεις λάμβαναν υπόψη τη μη-Νευτώνεια συμπεριφορά του αίματος, υπόθεση που ενισχύει τη φυσιολογική συνάφεια των αποτελεσμάτων CFD και υποστηρίζει πιο ακριβείς αιμοδυναμικές αξιολογήσεις.

Παρόλο που η μελέτη παρέχει πολύτιμες γνώσεις μέσω της ενσωμάτωσης CFD και υπερηχογράφησης Doppler, πρέπει να αναγνωριστούν ορισμένοι περιορισμοί. Η μοντελοποίηση βασίστηκε σε ιδεατές γεωμετρίες αρτηριών και όχι σε πλήρως εξατομικευμένες ανακατασκευές αγγείων, γεγονός που ενδέχεται να περιορίζει τη γενικευσιμότητα των προτύπων ροής. Επιπλέον, οι υποθέσεις που ενσωματώνονται στα μη-Νευτώνεια ρεολογικά μοντέλα ενδεχομένως επηρεάζουν την ακρίβεια των προσομοιώσεων. Τεχνικοί παράγοντες, όπως η ανάλυση του πλέγματος (mesh independency) και τα κριτήρια σύγκλισης παρακολουθήθηκαν προσεκτικά.

Δεν υπήρχαν διαθέσιμα πειραματικά δεδομένα για άμεση επικύρωση των αποτελεσμάτων της μελέτης. Επομένως, για την επαλήθευση της ακρίβειας της υπολογιστικής προσέγγισης, πραγματοποιήθηκαν πρότυπες προσομοιώσεις πλήρως ανεπτυγμένων στρωτών ροών στις γεωμετρίες των αγγείων. Συγκεκριμένα, τα προφίλ ταχύτητας και οι πτώσεις πίεσης που προέκυψαν από τις προσομοιώσεις

συγκρίθηκαν με καθιερωμένες θεωρητικές λύσεις των εξισώσεων Navier–Stokes, όπως η ροή Hagen–Poiseuille για τη σταθερή πίεση σε ευθείς κυκλικούς σωλήνες, η ροή Womersley που περιγράφει τα προφίλ παλλόμενης ταχύτητας σε παλμικές αρτηριακές ροές, και η ροή Dean που χαρακτηρίζει δευτερογενείς ροές σε καμπυλωμένους σωλήνες. Αυτές οι κλασικές λύσεις ροής παρέχουν σημαντικές αναφορές για την επικύρωση των CFD μοντέλων στις φυσιολογικές προσομοιώσεις ροής.

Επιπλέον, αν και παράμετροι όπως οι TAWSS, OSI και RRT παρουσιάζουν προοπτικές ως δείκτες αγγειακής προσαρμογής και δυσλειτουργίας, δεν υπάρχουν επί του παρόντος καθιερωμένα κλινικά όρια για αυτούς τους δείκτες στην αιμοδυναμική του μητριαίου-πλακουντιακού συστήματος. Ο καθορισμός τέτοιων διαγνωστικών ορίων απαιτεί διευρυμένες και μακροχρόνιες κλινικές μελέτες.

Τα ευρήματα υπογραμμίζουν τη σημασία της παρακολούθησης της αιμοδυναμικής του μητριαίου-πλακουντιακού συστήματος για την έγκαιρη ανίχνευση πιθανών επιπλοκών. Μια μη φυσιολογική μείωση του TAWSS ή παθολογική αύξηση του OSI και RRT θα μπορούσαν να λειτουργήσουν ως πρώιμοι δείκτες αγγειακής δυσλειτουργίας, απαιτώντας πιο στενή κλινική παρακολούθηση. Παρόλο που η CFD δεν αποτελεί ακόμη κλινικό πρότυπο, η ικανότητά της να αποκαλύπτει πρότυπα ροής πέρα από αυτά που εντοπίζει ο υπέρηχος υπογραμμίζει το δυναμικό της ως συμπληρωματικό διαγνωστικό εργαλείο.

Συνολικά, η διατριβή συμβάλλει σημαντικά στην κατανόηση της αιματικής ροής μεταξύ μητέρας και εμβρύου, με εφαρμογές κλινικού ενδιαφέροντος για την παρακολούθηση και αξιολόγηση της εξέλιξης της κύησης. Τα ευρήματα της μελέτης προωθούν τη γνώση στον τομέα της μητροεμβρυϊκής ιατρικής και της βιοϊατρικής ρευστομηχανικής, υποστηρίζοντας την έγκαιρη διάγνωση και βελτιωμένη διαχείριση επιπλοκών που σχετίζονται με την κύηση.

Βασιζόμενοι στα ευρήματα αυτής της μελέτης, προτείνονται αρχετοί σημαντιχοί άξονες για μελλοντιχή έρευνα. Μία βασιχή χατεύθυνση αφορά τη μελέτη της ροής αίματος υπό την επίδραση των ραβδώσεων στα τοιχώματα των αρτηριών, η οποία μπορεί να προσφέρει βαθύτερες γνώσεις σχετιχά με τη ρευστοδυναμιχή συμπεριφορά χαι τη μηχανιχή των αγγείων που εξετάζονται. Ένα αχόμη χρίσιμο βήμα είναι η ενσωμάτωση της αλληλεπίδρασης ρευστού-δομής (FSI) στα μελλοντιχά μοντέλα, προχειμένου να ληφθεί υπόψη η δυναμιχή χίνηση των αρτηριαχών τοιχωμάτων χατά τη διάρχεια του χαρδιαχού χύχλου, επιτυγχάνοντας έτσι πιο φυσιολογιχά αχριβείς ροϊχές δυναμιχές χαι χατανομές του TAWSS. Επιπλέον, η διερεύνηση προηγμένων αιμοδυναμιχών βιοδειχτών, όπως, μεταξύ άλλων, η ελιχότητα (helicity) χαι η στροβιλότητα (vorticity), θα μπορούσε να ενισχύσει την χατανόηση των σύνθετων χαραχτηριστιχών της ροής που σχετίζονται με τη λειτουργία χαι την παθολογία των αγγείων.

Επιπρόσθετα, απαιτούνται δημογραφικές μελέτες που θα περιλαμβάνουν κλινικά δεδομένα από διαφορετικές γεωγραφικές ή πληθυσμιακές ομάδες, ώστε να εντοπιστούν πιθανές διαφορές στην αιμοδυναμική του μητριαίου-πλακουντιακού συστήματος - τέτοιες διαφορές θα μπορούσαν να συμβάλουν στην ανάπτυξη διαγνωστικών προτύπων και θεραπευτικών στρατηγικών προσαρμοσμένων σε κάθε πληθυσμό. Ακόμη, η διερεύνηση της επίδρασης του εμβρυϊκού βάρους στη διαμόρφωση των προφίλ ταχύτητας στις υπό μελέτη αρτηρίες ενδέχεται να βελτιώσει την ακρίβεια των προσομοιώσεων, αντανακλώντας τις φυσιολογικές αλλαγές που συνδέονται με

την ανάπτυξη του εμβρύου.

Ενδιαφέρον παρουσιάζει η ενσωμάτωση εξατομικευμένων γεωμετριών, ειδικών για κάθε ασθενή, ανακατασκευασμένων από υπερηχογραφικές απεικονίσεις, η οποία δύναται να επεκτείνει τις εφαρμογές υπολογιστικής ρευστοδυναμικής (CFD) σε πραγματικό χρόνο και σε παθολογικές καταστάσεις. Η εφαρμογή αλγορίθμων μηχανικής μάθησης εκπαιδευμένων με δεδομένα από υπερήχους παρουσιάζει προστικές για την βελτίωση των διαγνωστικών δυνατοτήτων, επιτρέποντας τη χρήση προγνωστικών μοντέλων για επιπλοκές της κύησης. Η συνεχής ενσωμάτωση των προσομοιώσεων CFD στην κλινική αξιολόγηση αναμένεται να διευκολύνει την πιο έγκαιρη διάγνωση και την αποδοτικότερη διαχείριση των κυήσεων, βελτιώνοντας τελικά την υγεία μητέρας και εμβρύου.

Η έρευνα πραγματοποιήθηκε εν μέρει στο πλαίσιο της δράσης «Διατομεακές δράσεις σε διεπιστημονικούς τομείς με ιδιαίτερη έμφαση στον παραγωγικό ιστό», η οποία υλοποιείται μέσω του Εθνικού Σχεδίου Ανάκαμψης και Ανθεκτικότητας Ελλάδα 2.0, χρηματοδοτούμενου από την Ευρωπαϊκή Ένωση - NextGenerationEU (Αριθμός έργου: TAEDR-0535983).

Κρίνω επίσης σημαντικό να αναφερθεί ότι, κατά τη διάρκεια εκπόνησης της Δι-δακτορικής διατριβής, χρηματοδοτήθηκα μέσω του προγράμματος «ΔΙΩΝΗ: ΥΠ-ΟΛΟΓΙΣΤΙΚΗ ΥΠΟΔΟΜΗ ΕΠΕΞΕΡΓΑΣΙΑΣ ΚΑΙ ΑΝΑΛΥΣΗΣ ΜΕΓΑΛΟΥ ΌΓΚΟΥ ΔΕΔΟΜΕΝΩΝ - ΥΠΟΕΡΓΟ 1: ΕΡΕΥΝΗΤΙΚΗ ΔΡΑΣΤΗΡΙΟΤΗΤΑ ΚΑΙ ΥΠΗΡΕΣΙΕΣ ΝΕΦΟΥΣ» Κωδικό 82870 και Επιστημονικά Υπεύθυνο τον κ. Σταύρο Νικολόπουλο, του Επιχειρησιακού Προγράμματος Ε.Σ.Π.Α. 2014-2020, Τομεακά ΕΠ, ΕΠ «Ανταγωνιστικότητα, Επιχειρηματικότητα και Καινοτομία» (ΕΠΑνΕΚ), Πρόσκληση 111. Υποστήριξη της Περιφερειακής Αριστείας. Ανάπτυξη, διαχείριση και συντήρηση του λογισμικού των επιστημονικών υπολογισμών που αφορούν την επιστημονική περιοχή των Βιοϊατρικών Εφαρμογών στα πλάισια του Πακέτου Εργασίας Π1.1 του έργου «ΔΙΩΝΗ».

Λήφθηκε ενημερωμένη συγκατάθεση όλων των ατόμων που συμμετείχαν στη μελέτη. Η μελέτη εγκρίθηκε επίσης από την Επιτροπή Επιστημονικής Έρευνας του Πανεπιστημίου Ιωαννίνων και το Διοικητικό Συμβούλιο του Πανεπιστημιακού Νοσοκομείου Ιωαννίνων (αριθμός έγκρισης: 4558/24-2-25) Σχετικό PDF. Τα υπερηχογραφικά δεδομένα της έρευνας δεν διατίθενται για λόγους προστασίας της ιδιωτικότητας και εμπιστευτικότητας των ευαίσθητων προσωπικών δεδομένων των συμμετεχόντων.

Chapter 4

Notable Work

The current chapter provides information on the distribution of the research carried out during the course of this doctoral study. The following sections outline the most important publications, the works in progress that are meant to be submitted, the presentations made at conferences linked to this thesis, as well as the peer-review activities undertaken for relevant papers. These results and contributions constitute important milestones in the dissemination of the findings of this research to the wider scientific community, as well as in the promotion of discussion in the areas of Computational Fluid Dynamics, Biofluid Mechanics, and Maternal Fetal Medicine.

The publications listed consist of validated and peer-reviewed journal articles, as well as contributions to refereed collective volumes, that substantiate and build on the theoretical and computational models presented in this thesis. They also serve as the basis for further discussion of the clinical aspects of the findings. In the same spirit, the conferences where these presentations were made provided the opportunity to present preliminary results, receive comments, and establish contacts with specialists from adjacent fields. Additionally, the involvement in peer reviewing relevant manuscripts has allowed for critical engagement with ongoing research and contributed to maintaining high scientific standards in the field.

This chapter is organized as follows.

- Published work: Peer-reviewed articles have been published in scientific journals, as well as contributions to refereed collective volumes.
- Work in progress: Research that is currently being reviewed or planned for submission.
- Conference activity: Presentations and posters delivered at scientific meetings.
- Peer reviewing: Activities related to the critical evaluation of manuscripts submitted to scientific journals in relevant fields.

All of these accomplishments highlight the relevance of this study towards improving the knowledge of the uterine and umbilical blood flows, while concentrating on new avenues to pursue and the possibility for use in practice.

4.1 Published work

• Felias A, Skentou C, Paschopoulos M, Tzimas P, Vatopoulou A, Gkrozou F, Xenos M. Mathematical Study of Pulsatile Blood Flow in the Uterine and Umbilical Arteries During Pregnancy. Fluids. 2025 Aug;10(8):203.

Parts of the study were presented at the 3rd Panhellenic Conference of "Upcoming Researchers in the Disciplines of Mathematical Science", Ioannina, 24-25 May, 2024 and at the 13th Panhellenic Conference on Biomaterials, Ioannina, 28-29 March, 2025. As the presenter, I was awarded commendation certificates recognizing new researchers for this presentation.

Abstract

This study applies Computational Fluid Dynamics (CFD) and mathematical modeling to examine uterine and umbilical arterial blood flow during pregnancy, providing a more detailed understanding of hemodynamic changes across gestation. Statistical analysis of Doppler ultrasound data from a large cohort of more than 200 pregnant women (in the second and third trimesters) reveals significant increases in the umbilical arterial peak systolic velocity (PSV) between the 22nd and 30th weeks, while uterine artery velocities remain relatively stable, suggesting adaptations in vascular resistance during pregnancy. By combining the Navier-Stokes equations with Doppler ultrasound-derived inlet velocity profiles, we quantify several key fluid dynamics parameters, including time-averaged wall shear stress (TAWSS), oscillatory shear index (OSI), relative residence time (RRT), Reynolds number (Re), and Dean number (De), evaluating laminar flow stability in the uterine artery and secondary flow patterns in the umbilical artery. Since blood exhibits shear-dependent viscosity and complex rheological behavior, modeling it as a non-Newtonian fluid is essential to accurately capture pulsatile flow dynamics and wall shear stresses in these vessels. Unlike conventional imaging techniques, CFD offers enhanced visualization of blood flow characteristics such as streamlines, velocity distributions, and instantaneous particle motion, providing insights that are not easily captured by Doppler ultrasound alone. Specifically, CFD reveals secondary flow patterns in the umbilical artery, which interact with the primary flow, a phenomenon that is challenging to observe with ultrasound. These findings refine existing hemodynamic models, provide population-specific reference values for clinical assessments, and improve our understanding of the relationship between umbilical arterial flow dynamics and fetal growth restriction, with important implications for maternal and fetal health monitoring.

Link: MDPI website

 Felias AC, Rassias MT, Xenos MA, Paschopoulos ME. Mathematical Models and Advancements in Cardiac Hemodynamics. InMathematical Analysis, Optimization, Approximation and Applications 2025 (pp. 263-283).

Abstract

The emergence of advanced biomedical technologies has contributed to the development of biofluid dynamics. A major achievement of the latter is the prediction of hemodynamics, ie, the flow patterns and wall stresses of the cardiovascular system in the human body. Notable exact results on hemodynamics are obtained by means of the Hagen–Poiseuille, Womersley, and Korteweg–de Vries–Burgers (KdV–B) mathematical models. The semi-exact homotopy analysis method is discussed and a numerical Fluid Structure Interaction (FSI) approach is followed. The semiexact and numerical results are compared with the exact ones. As of current analysis, the KdV–B mathematical model seems to be quite reliable as a cardiac hemodynamics model. It also compares very well with other advanced multi-dimensional numerical methods, such as the presented FSI numerical method.

Link: World Scientific website

 Felias AC, Kyriakoudi KC, Mpiraki KN, Xenos MA. Analytic and numerical solutions to nonlinear partial differential equations in biomechanics. Analysis, Geometry, Nonlinear Optimization and Applications. 2023:331-403.

Abstract

The study of exact solutions to nonlinear equations is an active field of both, pure and applied mathematics. Plenty of the most interesting features of physical systems are hidden in their nonlinear behavior and can only be studied with appropriate methods designed to tackle nonlinearity. Therefore, seeking for suitable solving methods, exact, semi-exact or numerical, is an active task in branches of applied and computational mathematics. Complex phenomena in notable scientific fields, especially in physics, such as fluid and plasma dynamics, optical fibers, solid state physics, as well as in cardiac hemodynamics, can be efficiently mathematically modeled in terms of the Korteweg-de Vries (KdV), modified KdV (mKdV), Burgers and Korteweg-de Vries-Burgers (KdV-B) equations. In this review chapter, analytical solutions are sought for each of the aforementioned equations, by means of traveling wave and similarity transforms. Especially, for the KdV equation, one- and two-soliton solutions are derived. The Lax pairs are introduced and the Inverse Scattering Transform (IST) is discussed for the KdV equation. The Miura Transform is presented, connecting the KdV and mKdV equations. The Cole-Hopf Transform is described, converting the viscous Burgers equation to the linear Heat transport equation. Weak solution formulation is presented for the inviscid Burgers

equation. Additionally, the Rankine-Hugoniot condition is discussed in the implementation of the method of characteristics. Semi-exact solutions are obtained through the Homotopy Analysis Method. Numerical solutions are derived by means of spectral Fourier analysis and are evolved in time, using the fourth-order explicit Runge-Kutta method. Qualitative analysis is performed for the inviscid Burgers equation, and conservation laws in general, and phase plane trajectories are obtained for the KdV-B equation.

<u>Link</u>: World Scientific website

 Xenos MA, Felias AC. Nonlinear dynamics of the KdV-B equation and its biomedical applications. InNonlinear Analysis, Differential Equations, and Applications 2021 Mar 15 (pp. 765-793). Cham: Springer International Publishing.

Abstract

In recent years there is an incremental degree of bridging open questions in biomechanics with the help of applied mathematics and nonlinear analysis. Recent advancements concerning the cardiac dynamics pose important questions about the cardiac waveform. A governing equation, namely the KdV-B equation (Korteweg-de Vries-Burgers),

$$\frac{\partial u}{\partial t} + \gamma u \frac{\partial u}{\partial x} - \alpha \frac{\partial^2 u}{\partial x^2} + \beta \frac{\partial^3 u}{\partial x^3} = 0, \quad u = u(t,x), \quad \alpha,\beta,\gamma \in \mathbb{R}$$

is a partial differential equation utilized to answer several of those questions. The cardiac dynamics mathematical model features both solitary and shock wave characteristics due to the dispersion and dissipation terms, as occurring in the arterial tree. In this chapter a focus is given on describing cardiac dynamics. It is customarily difficult to solve nonlinear problems, especially by analytical techniques. Therefore, seeking suitable solving methods, exact, approximate or numerical, is an active task in branches of applied mathematics. The phase plane of the KdV-B equation is analyzed and its qualitative behavior is derived. An asymptotic expansion is presented and traveling wave solutions under both shock and solitary profiles are sought. Numerical solutions are obtained for the equation, by means of the Spectral Fourier analysis and are evolved in time by the Runge-Kutta method. This whole analysis provides vital information about the KdV-B equation and its connection to cardiac hemodynamics. The applications of KdV-B, presented in this chapter, highlight its essence to human hemodynamics.

Link: Springer's website

 Biraki KN, Kyriakoudi KC, Felias AC, Xenos MA. The Finite Element Method with Applications to Fluid Mechanics. Mathematical Analysis, Differential Equations and Applications. 2024:139-74.

Abstract

The finite element method (FEM) is a well-established approach for the

numerical solution of ordinary differential equations (ODEs) and partial differential equations (PDEs). This method is a powerful tool in the study of various problems and has many applications, such as structural and fluid mechanics. In this review chapter, we mainly focus on applying the method to fluid mechanics problems. Initially, we present the FEM along with the basic theorems and examples. We analyze the error estimates for linear problems and the base functions that help distinguish the problem under consideration. We present the numerical solution of the Duffing equation, using the Galerkin FEM.

Additionally, we concentrate on the two-dimensional Stokes problem. We further introduce novel methods, such as the Discontinuous Galerkin (DG) FEM. The notion of adaptive mesh is also discussed. Lastly, we study the two-dimensional Navier–Stokes equations using the Galerkin FEM. These advanced methods provide reliable numerical results in all studied cases. This is achieved with the application of FEM to "test problems", such as the backward-facing step. We obtain all the numerical results utilizing the software programs MATLAB and FEniCS.

<u>Link</u>: World Scientific website

• "Problem 265", Solved and Unsolved Problems Column, EMS Magazine (Anastasios Felias AC, Xenos MA).

Statement

"For a Newtonian incompressible fluid, the Navier–Stokes momentum equation, in vector form, reads ${\bf Q}$

$$\rho\left(\frac{\partial u}{\partial t} + u \cdot \nabla u\right) = -\nabla p + \mu \nabla^2 u + F,$$

$$u(x,t), \quad u \colon \mathbb{R}^n \times (0,\infty) \to \mathbb{R}^n \quad (1)$$

Here, ρ is the fluid density, u is the velocity vector field, p is the pressure, μ is the viscosity, and F is an external force field.

(i) Assuming that both the pressure drop ∇p and the external field F are negligible, it is easy to show that equation (1) reduces to

$$\frac{\partial u}{\partial t} + u \cdot \nabla u = \nu \nabla^2 u,$$

and finally to equation (2), where $\nu = \frac{\mu}{\rho}$ is the so-called kinematic viscosity 32.

(ii) Regarding the one-dimensional viscous Burgers equation

$$\frac{\partial u}{\partial t} + u \frac{\partial u}{\partial x} = \nu \frac{\partial^2 u}{\partial x^2}, \quad u = u(x, t), \quad (2)$$

prove that an analytical solution can be obtained by means of the Tanh Method [32, 45, 46] as

$$u(x,t) = \lambda \left[1 - \tanh\left(\frac{\lambda}{2\nu}(x - \lambda t)\right) \right], \quad \lambda > 0.$$
"

Link: EMS Magazine

 I have also contributed to the development of the work titled: "Ράπτης Α, Ξένος Μ. Εισαγωγή στην Υπολογιστική Ρευστοδυναμική μέσω της γλώσσας προγραμματισμού Python."

Abstract

Τα προβλήματα της Ρευστομηχανικής περιγράφονται από μη γραμμικά, συζευγμένα συστήματα μερικών διαφορικών εξισώσεων (Μ.Δ.Ε.), γεγονός που καθιστά την αναλυτική τους επίλυση εξαιρετικά δύσκολη. Για αυτόν τον λόγο, απαιτούνται αριθμητικές μέθοδοι. Σε αυτό το βιβλίο, παρουσιάζονται οι αριθμητικές μέθοδοι που εφαρμόζονται σε προβλήματα της Ρευστομηγανικής και μπορούν να προσφέρουν ακριβείς αριθμητικές λύσεις. Αρχικά γίνεται αναφορά στη γλώσσα προγραμματισμού Python, η οποία χρησιμοποιείται για την αριθμητική επίλυση συστημάτων Μ.Δ.Ε. Έπειτα παρουσιάζεται η μέθοδος ταξινόμησης συστήματος Μ.Δ.Ε. μέσω των χαρακτηριστικών και της ορίζουσας των συντελεστών των αγνώστων. Εισάγεται η έννοια του καλώς τοποθετημένου προβλήματος και περιγράφονται οι αργικές και συνοριαχές συνθήχες που απαιτούνται για την επίλυση προβλημάτων που περιγράφονται από Μ.Δ.Ε. Οι πιο βασικές αριθμητικές μέθοδοι που χρησιμοποιούνται στη Ρευστομηχανική είναι η μέθοδος των πεπερασμένων διαφορών, η μέθοδος των πεπερασμένων όγκων και η φασματική μέθοδος. Η εφαρμογή των αριθμητικών μεθόδων ξεκινά με την επίλυση της εξίσωσης διάχυσης και στη συνέχεια με τις εξισώσεις Laplace και Poisson. Ακολουθεί η επίλυση της εξίσωσης μεταφοράς, καθώς και προβλημάτων μόνιμης μεταφοράς και διάχυσης. Οι εξισώσεις του Burger και των Korteweg-de Vries επιλύονται αριθμητικά με τη χρήση κατάλληλων μεθόδων. Τέλος παρουσιάζεται η αριθμητική επίλυση των κύριων εξισώσεων ροής των Navier-Stokes. Το βιβλίο κλείνει με βασικές εφαρμογές όπως είναι η ροή σε ορθογώνια κοιλότητα, η ροή σε κανάλι κ.ά. Κάθε κεφάλαιο συνοδεύεται από λυμένες ασκήσεις για την καλύτερη κατανόηση της θεωρίας και της υλοποίησης υπολογιστιχού χώδιχα για την επίλυση προβλημάτων Ρευστομηχανιχής. Επιπλέον, παρέχονται άλυτες ασκήσεις για περαιτέρω εξάσκηση.

Link: Kallipos

4.2 Work in progress

• "Fluid-Structure Interaction (FSI) Methods for the Navier-Stokes Equations." In: Trends in Applied Mathematical Analysis (Felias AC, Kyriakoudi KC, Rassias TM and Xenos MA).

Abstract

Advanced fluid–structure interaction (FSI) simulations, exploiting the dynamic interaction between the vessel hemodynamics and wall deformation, is conducted to simulate the biomechanical behavior of arterial vessels. Initially, in this chapter a brief description of the basic fluid equations is introduced. Additionally, analytical solutions of basic fluid mechanics problems are discussed. Main focus is set on applying two–dimensional FSI methods on the Navier–Stokes equations, mathematically modeling blood flow in arteries. The cardiovascular data obtained are compared with numerical results, derived from numerical methods. In the FSI approach, the initial two–dimensional fluid equations are expanded to a mixed Euler-Lagrange formulation to study blood flow during the entire cardiac cycle. Transport equations are transformed into a moving body–fitted reference frame using generalized curvilinear coordinates. Furthermore, a generalization to a three–dimensional FSI approach is introduced and discussed.

<u>Link</u>: Fluid-Structure Interaction (FSI) Methods for the Navier-Stokes Equations.

• "Investigation of the forced Burgers' equation." Submitted for publication in: International Journal of Modelling and Simulation (Efstathiou AG, Felias AC, Petropoulou EN, Xenos MA).

Abstract

The forced Burgers' equation is investigated via the Homotopy Analysis Method. Various types of forcing terms and initial conditions are considered which give rise to several type of solutions such as wavefronts and shock waves. The obtained analytical solutions are compared with corresponding numerical ones indicating an excellent agreement between them. The results imply that there is a significant influence of the forcing term, as expected.

Link: Investigation of the forced Burgers' equation.

• "Fluid-Structure Interaction in Arterial Hemodynamics: A Mathematical Approach." (Kyriakoudi KC, Chrimatopoulos GT, Felias AC, Linardopoulos PD, Tzirtzilakis EE, Xenos MA)

Abstract

This review focuses on a variety of pathological vessels that are of interest in hemodynamics. In fluid mechanics, Partial Differential Equations are essential for describing physical phenomena, while Navier–Stokes equations are employed to describe the dynamics of fluid flow, providing a deeper comprehension of hemodynamics. Also, the two-dimensional and three-dimensional formulations of the Navier–Stokes equations are introduced both aiming to simulate blood flow in such arteries. The numerical solution of the yielding systems acquires the use of generalized curvilinear

coordinates and the finite volume method. Finally, a comparative analysis is provided by the presentation of blood flow's hydrodynamic cases through stenoses and aneurysms.

<u>Link</u>: Fluid-Structure Interaction in Arterial Hemodynamics: A Mathematical Approach.

• "Εφαρμοσμένα Μαθηματικά στις Βιοεπιστήμες." (Felias AC, Xenos MA)

<u>Link</u>: Εφαρμοσμένα Μαθηματικά στις Βιοεπιστήμες.

4.3 Conference activity

• "Mathematical Study of Blood Flow in Major Arteries of the Uterus and Umbilical Cord During Pregnancy." Presented at the 3rd Panhellenic Conference of "Upcoming Researchers in the Disciplines of Mathematical Science", Ioannina, 24-25 May, 2024 (Felias A, Skentou C, Paschopoulos M, Tzimas P, Xenos M.).

Περίληψη

Η Υπολογιστική Ρευστοδυναμική (CFD) και η μαθηματική μοντελοποίηση θα μπορούσαν να παράσχουν σημαντικές πληροφορίες για τη δυναμική των αρτηριαχών ροών της μήτρας και του ομφάλιου λώρου κατά τη διάρκεια της εγχυμοσύνης. Οι θεμελιώδεις εξισώσεις για την περιγραφή αυτών των ροών είναι οι εξισώσεις Navier-Stokes για ασυμπίεστα ρευστά. Η στατιστική ανάλυση δεδομένων υπερήχων Doppler που ελήφθησαν από έγχυες γυναίχες σε διάφορα στάδια κύησης παρέχει πληροφορίες σχετικά με τα εξελισσόμενα χαραχτηριστικά της αρτηριαχής ροής. Οι αρτηρίες της μήτρας και του ομφάλιου λώρου μοντελοποιούνται ως απλές γεωμετρίες, όπως για παράδειγμα ευθύγραμμοι και ελικοειδείς κυλινδρικοί σωλήνες. Αριθμητικές τρισδιάστατες προσομοιώσεις που διεξάγονται με τη χρήση προηγμένου λογισμικού CFD εξετάζουν σενάρια ροής στις μητριαίες και ομφαλικές αρτηρίες. Τα προφίλ ταχύτητας εισόδου που προέρχονται από δεδομένα υπερήχων Doppler καθοδηγούν αυτές τις προσομοιώσεις, ενώ τα αποτελέσματα συγκρίνονται με θεωρητικά και αριθμητικά προηγμένα μαθηματικά μοντέλα. Τα αποτελέσματα που προέχυψαν συμβάλλουν στη βαθύτερη χατανόηση των ροών των αρτηριών της μήτρας και του ομφάλιου λώρου κατά τη διάρκεια της εγκυμοσύνης, συμβάλλοντας στην αξιολόγηση της υγείας της μητέρας και του εμβρύου στην κλινική πράξη.

Link: Conference abstracts

• "Mathematical Study of Blood Flow in Major Arteries of the Uterus and Umbilical Cord During Pregnancy." Presented at the 13th Panhellenic Conference on Biomaterials, Ioannina, 28-29 March, 2025 (Felias A, Paschopoulos M, Tzimas P, Skentou C, Xenos M.).

As the presenter, I was awarded a commendation certificate for new researchers.



ΒΕΒΑΙΩΣΗ ΠΑΡΑΚΟΛΟΥΘΗΣΗΣ & ΕΠΑΙΝΟΣ ΝΕΟΥ ΕΡΕΥΝΗΤΗ

Ο κ. Αναστάσιος Φελιάς παρακολούθησε τις εργασίες του 13^{ου} Πανελληνίου Συνεδρίου Βιοϋλικών, που έγινε στους χώρους του Πανεπιστημίου Ιωαννίνων, στις 28 και 29 Μαρτίου 2025, και παρουσίασε, ως νέος ερευνητής, την εργασία με τίτλο «Μαθηματική μελέτη της αιματικής ροής σε βασικές αρτηρίες της μήτρας και του ομφάλιου λώρου κατά τη διάρκεια της εγκυμοσύνης» και συγγραφείς τους Αναστάσιο Φελιά, Μηνά Πασχόπουλο, Πέτρο Τζίμα, Χαρίκλεια Σκέντου και Μιχαήλ Ξένο.

Ο Πρόεδρος του Συνεδρίου

Καθηγητής Συμεών Αγαθόπουλος



Περίληψη

Η Υπολογιστική Ρευστοδυναμική (CFD) και η μαθηματική μοντελοποίηση θα μπορούσαν να παράσχουν σημαντικές πληροφορίες για τη δυναμική των αρτηριαχών ροών της μήτρας και του ομφάλιου λώρου κατά τη διάρκεια της εγχυμοσύνης. Οι θεμελιώδεις εξισώσεις για την περιγραφή αυτών των ροών είναι οι εξισώσεις Navier-Stokes για ασυμπίεστα ρευστά. Η στατιστιχή ανάλυση δεδομένων υπερήχων Doppler που ελήφθησαν από έγχυες γυναίχες σε διάφορα στάδια χύησης παρέχει πληροφορίες σχετιχά με τα εξελισσόμενα χαρακτηριστικά της αρτηριακής ροής. Οι αρτηρίες της μήτρας και του ομφάλιου λώρου μοντελοποιούνται ως απλές γεωμετρίες. Αριθμητικές τρισδιάστατες προσομοιώσεις που διεξάγονται με τη χρήση προηγμένου λογισμικού CFD εξετάζουν σενάρια ροής στις μητριαίες και ομφαλικές αρτηρίες. Τα προφίλ ταχύτητας εισόδου που προέρχονται από δεδομένα υπερήχων καθοδηγούν αυτές τις προσομοιώσεις, ενώ τα αποτελέσματα συγκρίνονται με θεωρητικά και αριθμητικά προηγμένα μαθηματικά μοντέλα. Τα αποτελέσματα που προέχυψαν συμβάλλουν στη βαθύτερη κατανόηση των ροών των αρτηριών της μήτρας και του ομφάλιου λώρου κατά τη διάρκεια της εγκυμοσύνης, συμβάλλοντας στην αξιολόγηση της υγείας της μητέρας και του εμβρύου στην κλινική πράξη.

<u>Link</u>: Conference page

• "Analytical and Numerical Study of the Forced Burgers Equation." Presented at the 11th International Conference from Scientific Computing to Computational Engineering (11th IC-SCCE), Loutraki, 3-6 July, 2024 (Efstathiou AG, Felias AC, Petropoulou EN, Xenos MA).

Abstract

The forced Burgers' equation is investigated via the Homotopy Analysis Method. Various types of forcing terms and initial conditions are considered which give rise to several type of solutions such as wavefronts and shock waves. The obtained analytical solutions are compared with corresponding numerical ones indicating an excellent agreement between them. The results imply that there is a significant influence of the forcing term, as expected.

Link: Conference page

"Mathemagics: The Doppler Effect." Presented at the Mathematics Club
 "Μεθόδιος Ανθραχίτης", Department of Mathematics, University of Ioannina, 9 November, 2023 (Felias AC).

Link: Presentation

"From equations to human health: Applications of Mathematics in Medicine"
 Presented at the Mathematics Club "Μεθόδιος Ανθρακίτης", Department of Mathematics, University of Ioannina, 17 October, 2024 (Felias AC).

Link: Presentation

• Attended the 16th Panhellenic Conference of Obstetrics & Gynecology, Ioannina, 13-16 June, 2024.

<u>Link</u>: Conference page

4.4 Peer reviewing

I have participated in the peer review of the following manuscripts:

 Subhan F, Nisar KS, Raja MA, Uddin I, Shoaib M, Ullah K, Islam S, Munjam SR. Novel quartic spline method for boundary layer fluid flow problem of Falkner-Skan model with wall stretching and transfer of mass effects. Case Studies in Thermal Engineering. 2024 Jan 1;53:103887.

Abstract

The non-linear ordinary differential equations (NODEs) in this article are estimated and analyzed numerically using the capability of the Quartic Splines Method (QSM) for mathematical modeling of the Falkner-Skan fluidic system and its optimization through global search Genetic Algorithms (GAs) and local search Active-Set (AS) techniques. The concept of hybridization is used to optimize the obtained results and provide a boost to

the suggested method, QSM, which allows for rapid iteration. Falkner-Skan fluid model (FSFM) is solved by the proposed technique QSM-GAs-AS. The FSFM is solved for three, seven, and twelve splines successfully. The problem is analyzed for three scenarios, in which each scenario is based on the variation of a parameter out of the three involved parameters, namely the wall mass transfer parameter (γ), the wall movement parameter (λ), and the stream-wise pressure gradient parameter (β), appearing in FSFM. The QSM-GAs-AS produces an interpolated function that is continuous up to its fourth derivative. The solution outcomes of FSFM, treated by the designed scheme QSM-GAs-AS, are presented graphically. The evaluation of the planned solution is done with a deterministic numerical solver, the Homotopy Analysis Method (HAM). Statistical analysis for multiple runs is used to examine the proposed scheme's convergence, exactness, and accuracy.

<u>Link</u>: ScienceDirect

• "Impact of Thermal Radiation on Heat and Mass Transfer in MHD Mixed Convection Nanofluid Flow over Stretching Sheet" by Mazhar Hussain, M Mansoor, Iqra Amer, Muhammad Hanif, Mubashir Qayyum, and Gilbert Chambashi for AIP Advances.

Abstract

This research work investigates the dynamics of mixed convective nanofluid flow across a stretched sheet, taking into account the effects of suction and magnetic fields. The important microscopic behavior of nanoparticles is emphasized, particularly how Brownian motion and thermophoresis influence macroscopic heat and mass transport processes. The problem is first formulated/modeled as partial differential equations then translated into ordinary differential equations using suitable transformations and the Runge Kutta method in MATLAB's byp4c package is utilized to obtain the numerical solution. The novelty includes an assessment of several dimensionless characteristics, such as the impact of rising magnetic fields, mixed convection, radiation, Eckert number, thermal slip, and Lewis number on velocity, temperature and concentration profiles. Important findings shows that magnetic fields reduce velocity but increase temperature and concentration. Enhanced mixed convection speeds up the fluid while cooling and diluting it, while radiation and higher Eckert numbers increase temperature. Thermal and velocity slip, Brownian motion, higher Lewis numbers, and suction significantly impact fluid behavior. The conclusions demonstrate complex connections between various factors, providing information for enhancing cooling and heating systems in industrial applications.

Link: Review invitation

Bibliography

- [1] Gallo DM, Poon LC, Akolekar R, Syngelaki A, Nicolaides KH. Prediction of preeclampsia by uterine artery Doppler at 20-24 weeks' gestation. Fetal diagnosis and therapy. 2013;34(4):241-7.
- [2] Clark AR, James JL, Stevenson GN, Collins SL. Understanding abnormal uterine artery Doppler waveforms: a novel computational model to explore potential causes within the utero-placental vasculature. Placenta. 2018;66:74-81.
- [3] Mandala M, Osol G. Physiological remodelling of the maternal uterine circulation during pregnancy. Basic & clinical pharmacology & toxicology. 2012;110(1):12-8.
- [4] Kasiteropoulou D, Topalidou A, Downe S. A computational fluid dynamics modelling of maternal-fetal heat exchange and blood flow in the umbilical cord. PLoS One. 2020;15(7):e0231997.
- [5] Ferguson VL, Dodson RB. Bioengineering aspects of the umbilical cord. European Journal of Obstetrics & Gynecology and Reproductive Biology. 2009;144:S108-13.
- [6] Spurway J, Logan P, Pak S. The development, structure and blood flow within the umbilical cord with particular reference to the venous system. Australasian journal of ultrasound in medicine. 2012;15(3):97-102.
- [7] Hu X, Zhang L. Uteroplacental circulation in normal pregnancy and preeclampsia: functional adaptation and maladaptation. International journal of molecular sciences. 2021;22(16):8622.
- [8] De Onis M, Blössner M, Villar J. Levels and patterns of intrauterine growth retardation in developing countries. European journal of clinical nutrition. 1998;52:S5-15.
- [9] Xenos M. An Euler-Lagrange approach for studying blood flow in an aneurysmal geometry. Proceedings of the Royal Society A: Mathematical, Physical and Engineering Sciences. 2017;473(2199):20160774.

- [10] Serrano A, Cunha V, Teixeira JP, Pires MB, O'Neill JG, Vassilenko V. Hemodynamics in human uterine arteries: modeling and computational fluid dynamics calculations. In: 2019 IEEE 6th Portuguese Meeting on Bioengineering (ENBENG). IEEE; 2019. p. 1-4.
- [11] Shah RG, Girardi T, Merz G, Necaise P, Salafia CM. Hemodynamic analysis of blood flow in umbilical artery using computational modeling. Placenta. 2017;57:9-12.
- [12] Ferdows M, Hoque K, Bangalee M, Xenos M. Wall shear stress indicators influence the regular hemodynamic conditions in coronary main arterial diseases: cardiovascular abnormalities. Computer Methods in Biomechanics and Biomedical Engineering. 2023;26(2):235-48.
- [13] Tasso P, Raptis A, Matsagkas M, Rizzini ML, Gallo D, Xenos M, et al. Abdominal aortic aneurysm endovascular repair: profiling postimplantation morphometry and hemodynamics with image-based computational fluid dynamics. Journal of biomechanical engineering. 2018;140(11):111003.
- [14] De Nisco G, Kok AM, Chiastra C, Gallo D, Hoogendoorn A, Migliavacca F, et al. The atheroprotective nature of helical flow in coronary arteries. Annals of biomedical engineering. 2019;47:425-38.
- [15] Malatos S, Fazzini L, Raptis A, Nana P, Kouvelos G, Tasso P, et al. Evaluation of Hemodynamic Properties After Chimney and Fenestrated Endovascular Aneurysm Repair. Annals of Vascular Surgery. 2024;104:237-47.
- [16] Pennati G, Socci L, Rigano S, Boito S, Ferrazzi E. Computational patient-specific models based on 3-D ultrasound data to quantify uterine arterial flow during pregnancy. IEEE transactions on medical imaging. 2008;27(12):1715-22.
- [17] Batchelor CK, Batchelor GK. An introduction to fluid dynamics. Cambridge university press; 1967.
- [18] Falkovich G. Fluid mechanics: A short course for physicists. Cambridge University Press; 2011.
- [19] Granger RA. Fluid mechanics. Courier Corporation; 1995.
- [20] Fletcher CA. Computational techniques for fluid dynamics. Volume 1-Fundamental and general techniques. Volume 2-Specific techniques for different flow categories. Berlin and New York. 1988;1.
- [21] Ferziger JH, Perić M, Street RL. Computational methods for fluid dynamics. springer; 2019.
- [22] Tzirtzilakis1 E, Sakalis V, Kafoussias N, Hatzikonstantinou P. Biomagnetic fluid flow in a 3D rectangular duct. International Journal for Numerical Methods in Fluids. 2004;44(12):1279-98.

- [23] Tzirtzilakis E. A simple numerical methodology for BFD problems using stream function vorticity formulation. Communications in Numerical Methods in Engineering. 2008;24(8):683-700.
- [24] Sharma A. Introduction to computational fluid dynamics: development, application and analysis. Springer Nature; 2021.
- [25] Patankar S. Numerical heat transfer and fluid flow. Taylor & Francis; 2018.
- [26] Kyriakoudi KC, Xenos MA. Magnetohydrodynamic effects on a pathological vessel: An Euler–Lagrange approach. Physics of Fluids. 2023;35(12).
- [27] Chrimatopoulos G, Tzirtzilakis EE, Xenos MA. Magnetohydrodynamic and Ferrohydrodynamic Fluid Flow Using the Finite Volume Method. Fluids. 2023;9(1):5.
- [28] Nichols WW, O'Rourke M, Edelman ER, Vlachopoulos C. McDonald's blood flow in arteries: theoretical, experimental and clinical principles. CRC press; 2022.
- [29] Gersten K. Hermann schlichting and the boundary-layer theory. In: Hermann Schlichting—100 Years. Springer; 2009. p. 3-17.
- [30] Nield D, Kuznetsov A. Forced convection with laminar pulsating flow in a channel or tube. International Journal of Thermal Sciences. 2007;46(6):551-60.
- [31] Abramowitz M, Stegun IA. Handbook of mathematical functions with formulas, graphs, and mathematical tables. vol. 55. US Government printing office; 1964.
- [32] Xenos MA, Felias AC. Nonlinear Dynamics of the KdV-B Equation and Its Biomedical Applications. In: Nonlinear Analysis, Differential Equations, and Applications. Springer; 2021. p. 765-93.
- [33] Demiray H. Wave propagation through a viscous fluid contained in a prestressed thin elastic tube. International journal of engineering science. 1992;30(11):1607-20.
- [34] Erbay H, Erbay S, Dost S. Wave propagation in fluid filled nonlinear viscoelastic tubes. Acta mechanica. 1992;95:87-102.
- [35] Felias AC, Kyriakoudi KC, Mpiraki KN, Xenos MA. Analytic and Numerical Solutions to Nonlinear Partial Differential Equations in Biomechanics. Analysis, Geometry, Nonlinear Optimization and Applications. 2023:331-403.
- [36] Felias AC, Rassias MT, Xenos MA, Paschopoulos ME. Mathematical Models and Advancements in Cardiac Hemodynamics. In: Mathematical Analysis, Optimization, Approximation and Applications. World Scientific; 2025. p. 263-83.

- [37] Saffar Y, Kashanj S, Nobes DS, Sabbagh R. The physics and manipulation of Dean vortices in single-and two-phase flow in curved microchannels: A review. Micromachines. 2023;14(12):2202.
- [38] Mestel J. Flow in curved pipes: The Dean equations. Lecture Handout for Course M4A33, Imperial College. 2024.
- [39] Dennis S, NG M. Dual solutions for steady laminar flow through a curved tube. The Quarterly Journal of Mechanics and Applied Mathematics. 1982;35(3):305-24.
- [40] Akbar NS, Nadeem S. Carreau fluid model for blood flow through a tapered artery with a stenosis. Ain Shams Engineering Journal. 2014;5(4):1307-16.
- [41] Tabakova S, Nikolova E, Radev S. Carreau model for oscillatory blood flow in a tube. In: AIP conference proceedings. vol. 1629. American Institute of Physics; 2014. p. 336-43.
- [42] Shyy W, Udaykumar H, Rao MM, Smith RW. Computational fluid dynamics with moving boundaries. Courier Corporation; 2012.
- [43] Kaplan AD, Jaffa AJ, Timor IE, Elad D. Hemodynamic analysis of arterial blood flow in the coiled umbilical cord. Reproductive Sciences. 2010;17(3):258-68.
- [44] Mimouni Z. The rheological behavior of human blood—comparison of two models. Open Journal of Biophysics. 2016;6(2):29-33.
- [45] Malfliet W, Hereman W. The tanh method: I. Exact solutions of nonlinear evolution and wave equations. Physica Scripta. 1996;54(6):563.
- [46] Wazwaz AM. The tanh method for traveling wave solutions of nonlinear equations. Applied Mathematics and Computation. 2004;154(3):713-23.